

E. van der Lingen

Dielectric spectroscopy for hydration monitoring, from application to portable sensor



Dielectric spectroscopy for hydration monitoring, from application to portable sensor

By

E. van der Lingen

in partial fulfilment of the requirements for the degree of

Master of Science
in Electrical Engineering

at the Delft University of Technology,
to be defended publicly on Friday July 10, 2020 at 10:00 AM.

Supervisor:	Dr. M. Spirito
Thesis committee:	Dr. M. Spirito
	Dr. M. Mastrangeli
	Prof. Dr. Ir. WA Serdijn

An electronic version of this thesis is available at <http://repository.tudelft.nl/>.



Preface

This thesis is part of the Master Graduation Project for the Master Electrical Engineering at the Technical University of Delft. The curriculum of this two-year program encompasses a 120 ECTS of which one year, i.e. 67 ECTS, of course work and a second year in which I choose to perform an extra project which contributed 15 ECTS and finally the thesis project which resulted in this thesis that accounts for the final 45 ECTS. All parts have to be successfully finished before one can finish the master program.

The origin of this thesis project comes from a project in which over a four-year course both a CMOS integrated permittivity sensing array with accompanying algorithms and software needed for accurate measurements were developed. This sensor, after calibration, detects the permittivity of a medium that is in near proximity of its sensing patches in milliseconds. In a laboratory setting this sensor shows great promise, because of this it was postulated that it could be used to detect the hydration level of a human body. Being, that a high permittivity correlates well with the presence of water. If this correlation can be satisfied, the sensor could provide benefits to the healthcare where a significant interest in monitoring the hydration levels of elderly and people with health problems is, as myriad of medical related problems which can be prevented of proper hydration levels. However, need to help migrate the sensor from the safe and controlled laboratory environment to the, in comparison much more hostile environment of today's society, is required.

A research proposal, to implement the last step as mentioned above, is defined by Dr. M. Spirito from the Electronics Research Laboratory at the TU Delft. The project consists of performing validation measurements, designing and manufacturing, in the Else Kooi Laboratory; packaging solution to encapsulate the chip and PCB design to enable a portable sensor technique. This thesis mainly focuses on three major challenges;

Develop and fabricate a packaging scheme that would provide encapsulation of the chip to allow use outside the controlled laboratory environment.

Investigate the hypothesis that a permittivity sensor can be used. If so, to what level to monitor the hydration level of a person.

Investigate which commercially of the shelf components are required around the permittivity sensor in order to allow the functionality without bulky laboratory instruments in a stand-alone printed circuit board prototype that can be used as a demonstrator of the sensing array.

The result from the first major challenge shows a promising relation between the hydration level on skin measurements. The packaging and fabrication show that many challenges needs to be faced during process. However, after accomplishment of these challenges a packaging solution could be defined to encapsulate the sensor. Regarding the design of PCB, creation of the input signals for the sensor on a PCB level shows promising developments.

*E. van der Lingen
Delft, July 2020*

Acknowledgement

My whole adventure started in Dr. M. Spirito office, where the concept of this thesis was described. The relation between the medical applicability and the technical aspects grabbed my attention immediately. Therefore, I would like to express my gratitude to Dr. M. Spirito for giving me the possibility to perform my master thesis in the ELCA group, while providing me with guidance, feedback and help throughout the progress of this project.

First a hardware implementation of the chip was described, but soon the packaging got included to the project. Since, the ELCA group 'always' leave the packaging solutions to the ECTM group, I got into contact with Henk van Zeijl. However, to enable packaging, work in the clean room is required. If you want to work in the clean room first you need to successfully fulfil the clean room training, PIT training and/or module training. However, this training did not explain how to work with SU8 and since everybody was telling me GOOD LUCK, when I told them that I will be using SU8. They scared me a lot. There I went starting with coating SU8 on a wafer and there I fell. Instead of a uniform spread of the SU8, I just got a stripe on the wafer. Luckily, there was Henk, helping me a lot during the whole process and providing me with the chips attached on the wafer. Therefore, a special thanks for Henk van Zeijl who helped and guided me a lot during the packaging procedures carried out in the clean room.

Besides the struggling with SU8 (which I overcame) there was still the struggling of the disappeared SU8 structures after aluminium deposition. The first thing I thought, is that everybody said to me that it is impossible to remove SU8 after development. However, I accomplished to do this. This somehow made me happy, that I discovered a way to remove SU8, but still I did not want this to happen. Luckily there was Johannes van Wingerden, to help me discover how this could happen and when it happens. He also described my loosening of SU8 structures as a caterpillar who removed my SU8 structures. This affect was really visible since my whole processing box is full with SU8 structures fallen from my wafers. Therefore, thank you Johannes van Wingerden for helping me with the discovery of the removed SU8 structures.

During the wild adventures in the clean room, I was also performing the validation measurements. Here I discovered the many influences on the validation measurements. Nevertheless, I was not the only one struggling to achieve consistent measurements. The problems I encountered, also encountered the owners of Vertigo, where I did a two-year internship, Luca Galatro and Raffaele Romano. They solved these problems taking assumptions and providing me insight into the system. Therefore, I would like to express my appreciation towards the owners of Vertigo; Luca Galatro and Raffaele Romano, who gave me the opportunity for a two-month internship during my graduation project and thereby gave me a lot of helpful feedback and discussions.

In the first measurements carried out with the old liquids a fast conclusion was made that the liquids were impure, meaning that new liquids had to be ordered. This was really a big 'journey', since I and Satoshi Malatoux were not allowed to buy them. We were not considered to be allowed to work with chemicals, since we do not have chemical background knowledge. Luckily, there was Robert Verhoeven. Robert is a chemical expert in the clean room and is therefore allowed to buy the liquids. We decided to order the chemical from Hinmeijer Chemie. After successfully placing the order, the delivery was planned to be in three weeks. After three weeks still no liquids and an email appeared from the company saying: we are not allowed to ship the liquids because somebody needs to sign for the approval of the order at Hinmeijer. We waited for three weeks, but still no liquids... Contacting the company again, they responded with: the delivery is on its way. Three days later still no liquids Contacting the company again and they responded; our apologies, the order is shipped to a different address and we lost your order, can you please place an order again. Still no liquids..... Finally after three weeks, we got the delivery (which was still not the entire delivery). Therefore, thank you Robert Verhoeven for having the patience to contact Hinmeijer every time and help us with getting the chemicals.

Last but certainly not least, I would like to specially thank Satoshi Malatoux for the guidance and feedback during the entire thesis. I gave him a lot of jobs and questions which were pretty annoying jobs and he still managed to accomplish them. Also, thank you for making the dumplings during the Chinese new year and for the patience while working with me and with Hinmeijer. Also, thank you for your guidance, even while you were working.

The coronavirus also played a major role during my thesis. Due to all the guidelines regarding the coronavirus, working in the cleanroom from 7:00 till 22:00 was not possible anymore, which gave the restrictions to work less hours, as the same also holds for the opening hours of the University. Besides the restrictions on the opening hours, there were still the skin measurements which I had to perform on individuals. Due to the 1.5 meter distance restriction, carrying out these measurements became a challenge which I gladly was able to tackle.

Finally, I want to thank the EKL staff for giving me the trainings on the equipment in the cleanroom. Thank you to all the other colleagues, friends and staff that gave insight and motivation to me to successfully finish this one-year project. I almost forget my family, who encouraged me to follow my ambitions in life.

*E. van der Lingen
Delft, July 2020*

Content

Abstract	11
1. Introduction.....	12
1.1 Hydration and human physiology	13
1.2 Essence	16
1.4 Main research question	16
1.5 Outline.....	16
2. Dielectric measurements for medical application	18
2.1 Sensing techniques.....	18
2.2 Medical diagnostics	22
3. Packaging of the CMOS permittivity sensor.....	25
3.1 CMOS permittivity sensor	25
3.2 Packaging solutions of the CMOS permittivity sensor	30
3.3 Processing steps	32
3.4 Custom developed packaging flowchart.....	33
3.5 Mask design.....	34
3.6 Results	38
3.7 Conclusion	48
4. First level validation dielectric spectroscopy for hydration monitoring.....	49
4.1 System overview	49
4.2 Matlab code to enable GUI interface measurements.....	50
4.3 Calibration procedure	52
4.4 Measurement setup.....	54
4.5 Measurement result.....	57
4.6 Measurements results new liquids	57
4.7 Conclusion	68
5. Proposed system	69
5.1 System block diagram	69
6. Prototype design	71
6.1 PCB board design.....	71
6.2 Signal generation.....	73
6.3 PLL design	74
6.4 RF line generation	75
6.5 CMOS sensing array	76
7. Conclusion	78
8. Discussion	79
Bibliography.....	80
Appendix A	85
Appendix B	87
Appendix B.1 Visual representation of processing step for SU8 metalized pillars.....	87
Appendix B.2 Visual representation for creation SU8 cavities	90
Appendix B.3 Flowchart	91
Appendix B.4 Process with spin coating SU8 at 1300 rpm and 800 rpm.....	99
Appendix C	106
Appendix C.1 Creation of calibration liquids.....	106
Appendix C.2 Creation of the Look Up Table	110
Appendix C.3 Building blocks influences.....	113

Table of figures

Figure 1: Hydraulic pressure which triggers fluid movement between plasma and interstitial fluid [6].	13
Figure 2: Cross-Section of skin and panniculus [8].	14
Figure 3: Layers of the epidermis [9].	14
Figure 4: Layer thickness of the epidermis and dermis for various regions of the body [17].	15
Figure 5: a) Electrical modeling of cancer cells [32] b) Measured S21 magnitudes of different cells [32].	18
Figure 6: Schematic overview of the interdigitated electrodes based capacitive sensing method [33].	19
Figure 7: a) Antibodies are binding to the target b) Silver enhancement process is achieved [33].	19
Figure 8: Diagram of skin integration and measurement principle [37].	20
Figure 9: Measured resonant frequency versus quality factor for air and different liquid samples [43].	20
Figure 13: Approximated water concentration profile in the skin [48].	21
Figure 10: Dielectric permittivity from three representative tumour tissues, with the locus of the data from dog skeletal muscle shown for comparison [50].	22
Figure 11: The measured dielectric constant from 500 MHz to 20 GHz for various glucose levels [53].	23
Figure 12: Conceptual framework for physiological processes leading to pressure ulcer development [56].	24
Figure 14: Sensor matrix readout architecture [65].	25
Figure 15: Schematic of the implemented fully differential double balanced bridge [64].	26
Figure 16: Current-mode down conversion mixer schematic [64].	26
Figure 17: Ethanol permittivity measurement versus frequency [64].	27
Figure 18: 5x5 permittivity sensing array [69].	27
Figure 19: a) Wafer with available chips b) The dimensions of the chip and array.	28
Figure 20: Thickness of die of other participant measured using caliper.	28
Figure 21: Top view and side view of the patches in the 5x5 array CMOS permittivity sensor.	29
Figure 22: Cross section image of SU8 metalized pillars.	30
Figure 23: Cross section image of metalized silicon pyramids.	30
Figure 24: Cross section image of cavities filled with aluminium	31
Figure 25: Overview of the mask design for creating SU8 pillars.	34
Figure 26: Mask design for single chip to create SU8 pillars.	35
Figure 27: Mask design for single chip to create metallized pillars.	36
Figure 28: Mask designs for single chip to create metallized SU8 metalized pillars.	36
Figure 29: Overview of mask for creation cavities in a SU8 layer.	37
Figure 30: Single chip mask to create cavities in SU8.	38
Figure 31: Vertical height measurements of spin coating SU8 with 1100 rpm.	39
Figure 32: Horizontal height measurements of spin coating SU8 with 1100 rpm.	40
Figure 33: Tilt images from SU8 metalized pillars: a) Total overview of a single chip SU8 metallization, b) SU8 pillar metallization for single pillar with dimensions, c) High resolution metallization on top view of SU8, d) Top view two chip SU8 structures.	41
Figure 34: AZ9260 photoresist coverage of SU8 metallized pillars: a) Coating on the 5x5 pillar array, b) Coating on a single pillar.	42
Figure 35: Tilt images from SU8 metalized pillars after AZ9260 development: a) Total overview of a single chip, b) For single pillar with dimensions, c) Single pillar view, d) High resolution development on pillar side.	43
Figure 36: Tilt images from SU8 metalized pillars after wet etching aluminium; a) Total overview of a single chip, b) Height measurement of etched aluminium, c) Etching behavior on single pillar, d) High resolution of the aluminium on the bottom of the SU8 metalized pillar.	44
Figure 37: Tilt images for cavities in SU8: a) Total overview of a single chip, b) Corner image, c) Cavity in SU8, d) Cavity in SU8 depth measurement.	45
Figure 38: Chip overview of attachment to the carrier wafer: a) Top view, b) Side view.	46
Figure 39: Tilt images from SU8 metalized pillars on the CMOS permittivity chip: a) Total overview of a single chip, b) Dimensions of the applied SU8 layer, c) Alignment on the left side of the wafer, d) Alignment on the right side of the wafer.	47
Figure 40: System overview with connections, settings and interfaces.	49

Figure 41: Creation of the real Admittance, from the real permittivity, for the calibration liquid methanol.	50
Figure 42: Creation of real Admittances, for a given real permittivity, for the LUT.	51
Figure 43: Measurement setup with pin and patch configuration.	52
Figure 44: Calibration setup overview.	53
Figure 45: Top view for different geometry of the pin and patches.	53
Figure 46: Side view for different geometry of the pin and patches.	54
Figure 47: Calibration measurements.	54
Figure 48: Measurement overview.	55
Figure 49: GUI interface for validation measurements.	56
Figure 50: S11-parameter for calibration measurements a) overview b) zoom version	58
Figure 51: Permittivity measurements for calibration check.	58
Figure 52: Zoom version of S11-parameter measurements for the independent liquids and air.	59
Figure 53: Permittivity measurements for the independent liquids and air.	59
Figure 54: a) Zero-state measurement b) Putting the hand in water for 10 minutes c) Resulting hand hydration after 10 minutes of water.	60
Figure 55: Real permittivity zero state skin measurements: a) test person 1 b) test person 2 c) test person 3 d) average of each test person compared to each other.	61
Figure 56: Imaginary permittivity zero-state skin measurements; a) test person 1 b) test person 2 c) test person 3 d) average of each test person compared to each other.	62
Figure 57: Real permittivity hydrated-state skin measurements; a) test person 1 b) test person 2 c) test person 3 d) average of each test person compared to each other.	63
Figure 58: Imaginary permittivity hydrated-state skin measurements; a) test person 1 b) test person 2 c) test person 3 d) average of each test person compared to each other.	64
Figure 59: Real permittivity zero-state versus hydrated-state measurements; a) test person 1 b) test person 2 c) test person 3 d) test person comparison.	65
Figure 60: Imaginary permittivity zero state vs hydrated state measurements a) test person 1 b) test person 2 c) test person 3 d) test person comparison.	66
Figure 61: Absolute difference plotted for a) real permittivity b) imaginary permittivity.	67
Figure 62: System overview of the sensor with input and readout circuit.	69
Figure 63: Schematic of input board for CMOS sensing array.	71
Figure 64: PCB board design for the CMOS sensing array.	72
Figure 65: 3D view of the designed PCB layout.	73
Figure 66: Schematic design for the crystal oscillator CWX813.	74
Figure 67: a) Layout of the crystal oscillator b) 3D view of the crystal oscillator.	74
Figure 68: Schematic design for the PLL LMX2581.	75
Figure 69: a) Layout of one PLL LMX2581 b) 3D view of the PLL LMX2581.	75
Figure 70: Calculation of RF line using ADS.	76
Figure 71: Schematic of the CMOS sensing array.	77
Figure 72: a) Layout of the CMOS permittivity sensor b) 3D view of CMOS permittivity sensor.	77
Figure 73: Complex permittivity of the palm measured in vivo [47].	85
Figure 74: Complex permittivity of the temple measured in vivo [54].	85
Figure 75: Complex permittivity of the neck measured in vivo [54].	86
Figure 76: Complex permittivity of the abdomen measured in vivo [54].	86
Figure 77: Tilt images from SU8 metalized pillars: a) Total overview of a single chip SU8 metallization, b) SU8 pillar metallization for the 5x5 array, c) Two dike images of two chips SU8 metallization, d) High resolution metallization on top view of SU8 pillar.	100
Figure 78: Vertical height measurements of spin coating SU8 with 800 rpm.	101
Figure 79: Horizontal height measurements of spin coating SU8 with 800 rpm.	102
Figure 80: Tilt images from SU8 metalized pillars: a) Overall overview of a single chip SU8 metallization, b) SU8 pillar metallization for single pillar with dimensions, c) High resolution metallization on top view of SU8, d) Single pillar image.	103
Figure 81: Tilt images from SU8 metalized pillars after AZ9260 development: a) Total overview of a single chip, b) Second chip total overview, c) Third chip total overview, d) High resolution development on pillar side.	104

Figure 82: Tilt images for cavities in SU8 a) Overview of single chip b) Cavity dimensions.	105
Figure 83: a) S11-parameter of the cable influence measurements b) Zoom version of the S11-parameter	113
Figure 84: a) Real epsilon measurement of the cable distortion b) Imaginary epsilon for cable distortion measurement.	114
Figure 85: Water depth measurements; a) Deep inside the water b) Above the water surface creating a bubble c) Gold measurement, where the water is just touching the pin and patch.	115
Figure 86: S11-parameter measurement with different liquid depths.	116
Figure 87: Permittivity measurements with real and imaginary epsilon for water depth measurements.....	116
Figure 88: S11-parameter measurements for calibration configuration 1; a) general overview b) zoom version.	117
Figure 89: a) Real permittivity b) imaginary permittivity for calibration 1 configuration.	118
Figure 90: S11-parameter measurements for calibration configuration 2 a) general overview b) zoom version.	118
Figure 91: a) Real permittivity b) imaginary permittivity for calibration 2 configuration.	119
Figure 92: S11-parameter zero-state skin measurements: a) test person 1, b) test person 2, c) test person 3, d) average of each test person compared to each other.	120
Figure 93: S11-parameter hydrated-state skin measurements; a) test person 1 b) test person 2 c) test person 3 d) average of each test person compared to each other.	121
Figure 94: S11-parameter zero-state versus hydrated-state measurements; a) test person 1 b) test person 2 c) test person 3.....	122

Abstract

Due to the earth's population growth and the increased living age of a person, more and more people could deal with medical problems. Early detection of health related problems in both healthy and people with medical problems, will catch problems early and prevent the need for more costly procedures. One of these medical problems is concerning the hydration level. Dehydration most often occurs for elderly people. To prevent sickness and even death, monitoring of the hydration can play a key factor in prevention.

Hydration monitoring can be established by using a designed CMOS permittivity sensor. However, to design a commonly used hydration monitoring device, this CMOS permittivity sensor needs to be designed in such a way that portable sensing could be enabled.

To design such a portable hydration sensor from an application sensor, different steps are required. To bring previously developed sensor to enable hydration monitoring, it need to be packaged in such a way that it can sense the medium of interest and be connected to the outside world while sufficiently protected, so that it will not damage during use. Different packaging procedures could be distinguished to accomplish this. The first packaging procedure is regarding the creation of SU8 metallized pillars. The second packaging procedure is for creation of cavities in SU8 and fill these cavities with aluminium particles.

Besides the packaging of the sensor chip, validation measurements are required to ensure that a relationship could be detected with the permittivity sensor between the hydration level of the human skin.

To enable measurements of the skin permittivity without bulky systems, a PCB layout should be designed.

1. Introduction

In 2011 the world counted 7.0 billion people. The expected world population in 2050 will be grown up to 9.3 billion people and in the year 2100 even till 10.1 billion. Besides the population growth, the life expectancy will also increase from 69 years to 81 years in the year 2100. Moreover will the percentage of people aged over 60 years grow from 11 to 28 percent [1].

This increase in the world population and the relative increase in population age is expected to strongly impact the healthcare costs. These healthcare costs include monitoring, medicine intake and caring of people. For all the above reasons, current trend in medicine are to increase the level of non-invasive monitoring and thus reduce the testing time, patient discomfort and eventually the requirement of expensive direct nurse monitoring.

Currently there is a myriad of equipment to measure temperature, heart rate, oxygen levels, etc. However, for hydration levels this is not the case. This, for all but the most critical cases, is still done by accounting for fluid intake and bathroom visits or pinching a person skin to see its elasticity (turgor test). Despite the fact that most of the experts in the medical community will tell you that having a proper hydration level is essential for preventing medical complications. Commonly, dehydration is known as one of the causes of health complications and diseases for elderlies, athletes and children. Dehydration can lead to kidney failure, low blood pressure, seizure and even death [2]. The hydration level plays a more important role in the elderly people. Elderlies mostly lose their sensation for thirst and therefore become dehydrated more often[3].

According to US statics is the cost for treatment of dehydration among elderly patients 1.36 billion dollars in the year 1996 [4]. Because of the increase in elderly people each year, the need in hydration monitoring, to reduce cost and societal strain is needed.

Hydration can be connected to other parameters. For instance, the hydration level has a linkage between the permittivity and nutrients concentration. This permittivity can be referred to as complex permittivity. The permittivity of water can be found as the interaction between EM radiation and water molecules varies across the frequency spectrum (i.e., dielectric fingerprint of a material). This frequency dependence of the permittivity and un-ionized water is given by the Cole-Cole model.

However, the permittivity is not the same for water. For instance water in different soils have different permittivities [5]. This is mainly due to the fact that this water contains different nutrients and/or different amounts meaning that the hydration level of each person can differ per person and body part.

To conclude, insight into an individual also gives insight into the well-being of a person. However, to get a better feeling of the hydration mechanism in the human, background knowledge is required. Therefore, the human physiology regarding the hydration will be discussed.

1.1 Hydration and human physiology

The body water is divided into fluid compartments. These compartments consist of the intracellular fluid (ICF) and counts for the water into the cells. The other compartment is the extracellular fluid compartment (ECF) and can be subdivided into the plasma and interstitial fluid parts, which are the fluid compartments in the blood plasma and the fluid outside of the cells. Along these compartments fluid movement is possible and can occur based on osmotic and hydrostatic pressure. The hydraulic pressure raises fluid movement between the plasma and the interstitial fluid. The mechanism of this principle can be seen in Figure 1. Movement of water from the interstitial to the intracellular compartment will occur in a two-way osmotic manner through the plasma membrane. With this fluid flow through the body, water can be transported to different areas.

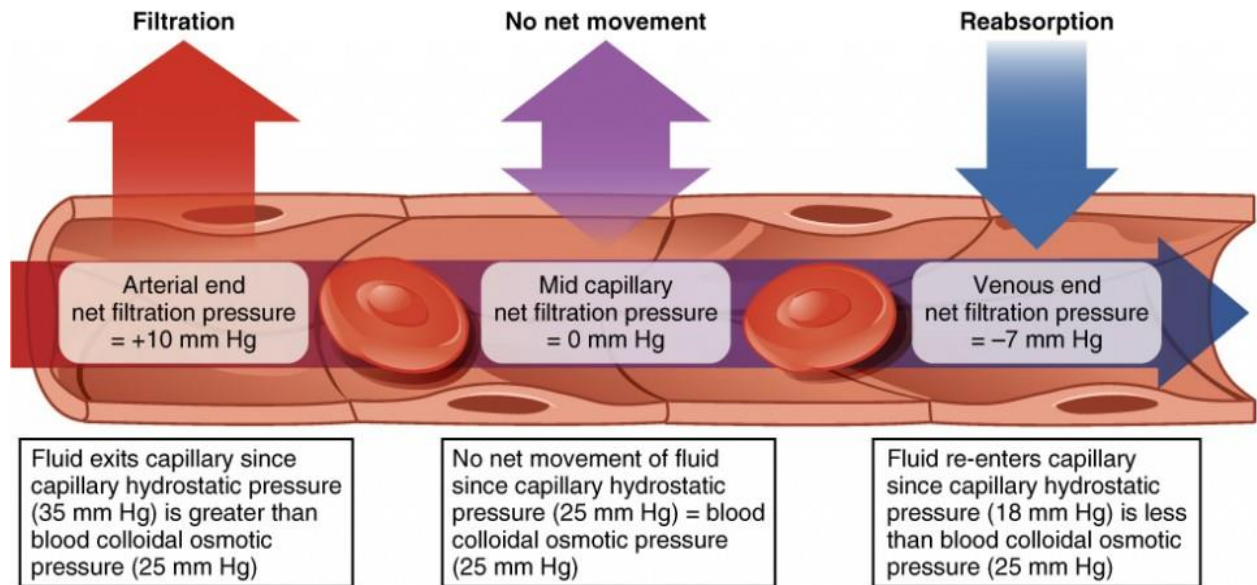


Figure 1: Hydraulic pressure which triggers fluid movement between plasma and interstitial fluid [6].

The skin is the largest organ of the body and is account to be 15% of the body weight. The skin is responsible for different functions in the body, it protects the inner organs from the external physical environment, chemical exposure and biologic assailants. The vital function which is the most interesting for the hydration is the prevention of excess water loss and the role in the thermoregulation (sweating) [7].

With this in mind, one can observe that a large amount of fluid is stored in the skin. To examine the fluid balance, an observation of the skin topology is necessary. A cross-section of the skin can be seen in Figure 2. The skin consists of three layers; the upper layer epidermis, the dermis and the subcutaneous tissue. The epidermis thickness is an average of 0.1 mm, which is roughly the thickness of a sheet of paper and the dermis layer has an average thickness of 2 mm.

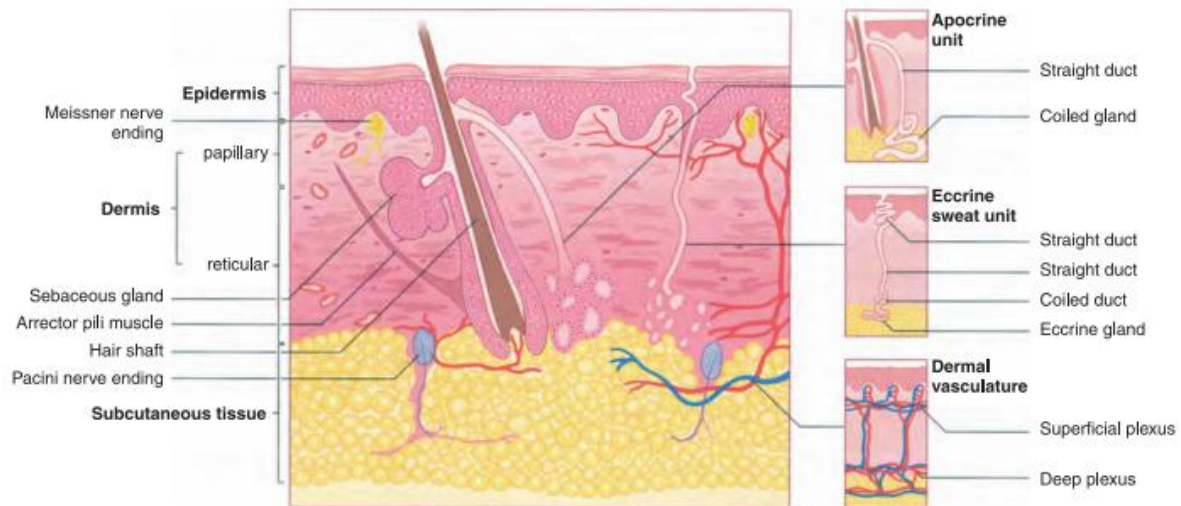


Figure 2: Cross-Section of skin and panniculus [8].

The epidermis consists of different layers, which can be seen in Figure 3. The upper layer is the stratum corneum and consist of a layer of dead cells. The basal cells of the stratum lucidum undergo cycles which provide renewal of the outer layer of the epidermis. These cycles undergo in an unsynchronized motion, which differs from other cells [8]. The stratum basale is connected to the dermis layer and contains mostly the same content as the dermis layer.

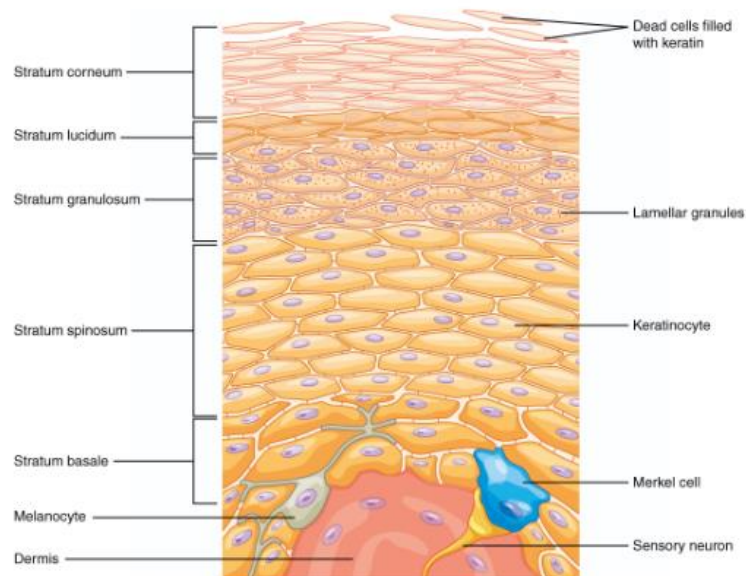


Figure 3: Layers of the epidermis [9].

In the dermis layer are the hair follicles, sweat glands, nerves and other structures. The dermis layer mostly consists of the proteins collagen and elastin, blood and lymph vessels and specialized cells called mast cells, fibroblast and fat cells (lipocytes) [10]. These structures will work together in a mesh-like network and are surrounded by a gel-based substance. This gel-based substance plays a critical role in the hydration and moisture levels of the skin [11]. Collagen is the most important component of the skin that contributes to the hydration level. The molecule structure of collagen shows that hydrogen bonds are present. Furthermore, collagen is able to perform hydrolysis, which is an important factor for the hydration level in the skin [12].

The subcutaneous tissue is the lowest layer of the skin and contains fibroblasts, adipose cells and macrophages [13]. This tissue contains mostly fat cells, which do not contribute to the hydration level.

Due to the rise of the sweat gland function from the epidermis layer, the eccrine sweat unit should be highlighted into more detail. The eccrine sweat glands are involved in the thermoregulation of the human body. The sweat glands are made of a band of epithelial cells which are growing downwards from the epidermis layer [14]. The structure of the sweat gland function can be distinguished in the following parts; intraepidermal spiral duct, the straight duct, the straight dermal portion and the coiled secretor duct [10].

The intraepidermal duct is open at the skin surface and consists of dermal duct cells which are migrated upwards. Cells in the duct undergo cornification, which will produce the corneocytes cells and these cells are becoming part of the cornified layer. The straight duct connects the intraepidermal duct to the inner layered coiled secretor duct. The secretor duct of the eccrine unit lies deep into the dermis layer and is composed of glycogen-rich clear secretory cells, dark mucoidal cells, and myoepithelial cells specialized in contractile properties [10, 14].

According to *Kolarsick et al*, clear cells rest either on the membrane or on the myoepithelial cells and create the intercellular canaliculi where two clear cells join. The canaliculi open directly into the lumen of the gland large, glycogen-rich inner epithelial cells start the formation of sweat in response to a thermal stimulus. Initially an isotonic solution located in the darker mucoidal cells in the secretor duct and in the dermal duct, actively reabsorb the sodium from the sweat in the duct, resulting in the extremely hypotonic solution that is emitted on the skin surface through the intraepidermal duct. This response promotes cooling while keeping the sodium level stable in the skin [15].

The eccrine sweat gland contributes to the thermal regulation. However, the apocrine sweat glands are involved into the scent release [16]. I will not discuss this apocrine unit furthermore, due to the non-influence of the apocrine sweat glands to the thermal regulation and thus the hydration level.

The three most important layers for the hydration application are the stratum corneum, epidermis and dermis. However, these three layers do not have the same thickness. The thickness of each layer is dependent on the location. In Figure 4 the different layer thickness for various regions of the body can be seen. In this figure, it can clearly be seen that the epidermis is approximately lower in thickness than the dermis [17].

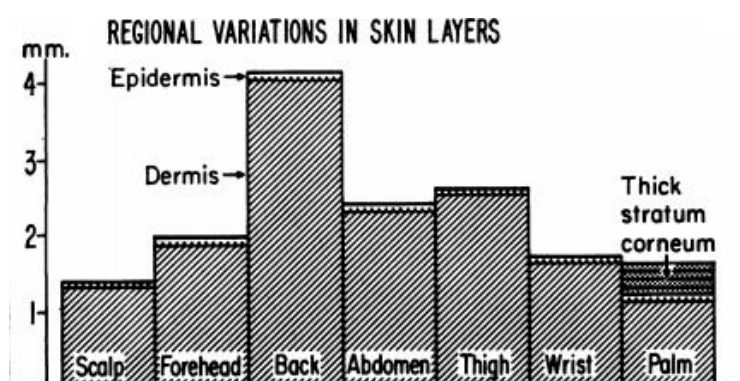


Figure 4: Layer thickness of the epidermis and dermis for various regions of the body [17].

To conclude, the most hydrated part of the skin is the dermis, this is mostly due the many blood vessels and the collagen. Blood vessels make it possible to transport water in an efficient and fast way resulting in a faster hydration transaction between skin and blood. Furthermore, collagen is the most important protein for the elasticity and fluid level in the dermis layer [18]. Therefore, the dermis is the most useful layer to examine in the hydration field.

Currently, there are different approaches to detect the hydration level in a patient. One of these approaches is testing based on the laboratory equipment. The techniques, which can be used here, are the isotope dilution [19], neutron activation analysis [20], bioelectrical impedance spectroscopy [21],

plasma osmolality [22], urine specific gravity, conductivity and osmolality [23]. However, these techniques are costly and time-consuming. Because of this they are not widely applied or easily accessible for most people.

Another approach is related to the visual inspection of the urine colour [24] or the skin turgor [25]. The benefit of this approach is that no special equipment is required, which is less labour intensive. However, this approach is hard to practice by non-experts. Also, visual inspection of the skin turgor in the elderly is not convenient due to the lack of elasticity of the skin. The skin of elderlies is less flexible and will therefore not quickly return to its normal state. Because of this, indication of hydration with this approach is not that reliable for elderlies [26].

1.2 Essence

As mentioned above, is the current detection of dehydration far from ideal. Using this approach requires costly laboratory work and continues monitoring is not applicable. To enable a continuous monitoring of the person's hydration at low power (i.e., wearable) sensor that could capture a measured directly related to the water concentration in a given layer is desirable. A CMOS based sensor to measure in close proximity the complex permittivity of a layer was recently developed at the ELCA group at the Delft University of Technology from the STW Informer project, this sensor which is described in more details in Section 3.1, and will provide the sensing hardware for the work carried out in this thesis is name Essence.

1.3 Main research question

As mentioned in the previous section a permittivity sensor is implemented to determine the permittivity with a penetration depth of two mm. However, this permittivity sensing chip relies on signal generators, readout system and other machines. These generators are big machines and therefore, far from ideal to measure the skin permittivity. The work carried out in this thesis spun out from the following research question:

What is the packaging technique and reacquired PCB level hardware to enable the usage of near field CMOS sensor to provide hydration level readouts?

1.4 Outline

This thesis is divided into different sections. At first, current medically applied permittivity sensing technique will be discussed. Secondly, the CMOS permittivity chip sensor to enable permittivity measurement is discussed, regarding the architecture, circuit analysis, measurement performance and packaging.

The main research question can be divided into smaller sub questions. Different subtasks could be distinguished while designing a portable sensor on the existing CMOS permittivity sensor. One task is regarding the packaging of the chip to ensure that the chip is able to perform measurements while being protected from harmful inputs. With this in mind the following sub questions can be defined regarding the packaging of the chip:

Chapter 3 deals with the packaging techniques for near field sensor and addresses the following sub questions:

- Which packaging solutions are able to protect the chip?
- Which steps are required to result in the given packaging solutions?
- Where can these packaging steps be performed?
- Which parameters influences the performance of these packaging steps?

After the packaging of the chip, validation measurements should be performed to ensure that the hydration level of the human skin can be monitored. Regarding the validation measurements, the following sub questions could be distinguished.

Chapter 4 deals with the validation measurements using a pin and patch configuration and addresses the following sub questions:

- Which aspects should be measured (noise, power, etc)?
- How are the results compared to the expectations?
- What are the most important aspects?
- What do the results tell us in its performance?
- How far can we relate these validation measurements to the permittivity sensor?

As mentioned before, it is convenient to remove the bulkiness of the machines to enable a portable readout system. To achieve this, a printed circuit board (PCB) can be designed in which the bulky machines are replaced by smaller components. While designing this PCB, the following sub questions can be distinguished:

Chapter 6 deals with the PCB design for the CMOS permittivity sensor and addresses the following sub questions:

- Which components are needed for the generation of the input signals for the sensor?
- Which components are needed for readout of the output signals of the sensor?
- How do these components contribute to the performance of the system?
- How should the PCB be designed, with the attached components?

After completion of each subsection, an overall sub question can be defined for all of the subsection and is given as follows: How to optimize the system?

This will lead to a conclusion on the performance of the sensor and a discussion where further recommendations are given.

2. Dielectric measurements for medical application

Permittivity is a materials ability to store an electric field in the polarization of the medium and is denoted by ϵ (epsilon) [27]. Epsilon is a complex number which varies with frequency, and its real part is associated with the polarization of the molecules constituting the medium while the imaginary part is associated with the loss mechanism that these molecules generate when excited by an alternating field. Often the permittivity is modeled with a reactive (capacitance) as element. This permittivity can be measured by using different sensing techniques. Several of these sensing techniques will be examined regarding their behaviour, in the coming section.

2.1 Sensing techniques

Electromagnetic waves can be used for creating diagnosis images. This principle is introduced in a Magnetic Resonance Imaging (MRI) device. To obtain such images in the sagittal, transverse and coronal plane of the human body, excitation of the electromagnetic waves is desired. The images from the MRI, can be used to obtain 3D images.

These images are obtained by the weighting dissipation time of the hydrogen longitudinal relaxation time and thereby looks at the amount of hydrogen in the body. The electromagnetic fields in the 3D plane are calculated as follows [28]:

$$M_z = M_0(1 - e^{-k_1 t}) \quad (1.1)$$

$$M_{x,y} = M_0 e^{-k_2 t} \quad (1.2)$$

Here the z-plane is given in the length of the human body and the xy-plane is given in the transverse plane of the human. Using this principle allows us to detect the fluid amount in the human body.

Another sensing technique which can be used for detecting permittivity is the capacitive sensor. A capacitive sensor can be used to detect and measure force, humidity and fluid level. This makes it possible to detect the fluid level in a specie. By changing the capacitance of the sensor, the frequency of the sensor can change but the amplitude of the AC signal can also change, which makes it possible to use two different types of readout system [29] [30]. For instance, using a fingerprint makes it possible to change the capacitance of the system and depending on the molecules in that fingerprint, the capacitance can differ. With this in mind, different substances consisting in the fingertip can be detected [31].

Such a capacitive sensor can be made by using a coplanar waveguide (CPW) transmission line. Both the CPW transmission line and cancer cells were modelled using RLCG circuit elements, see Figure 5a [32]. The resistance and capacitance of the different cancer cells can be sensed by observing the reflection coefficient over 40 GHz bandwidth [33]. By using the coplanar waveguide transmission line with a microfluidic channel placed on top, an innovative high-frequency based biosensor can be achieved [34].

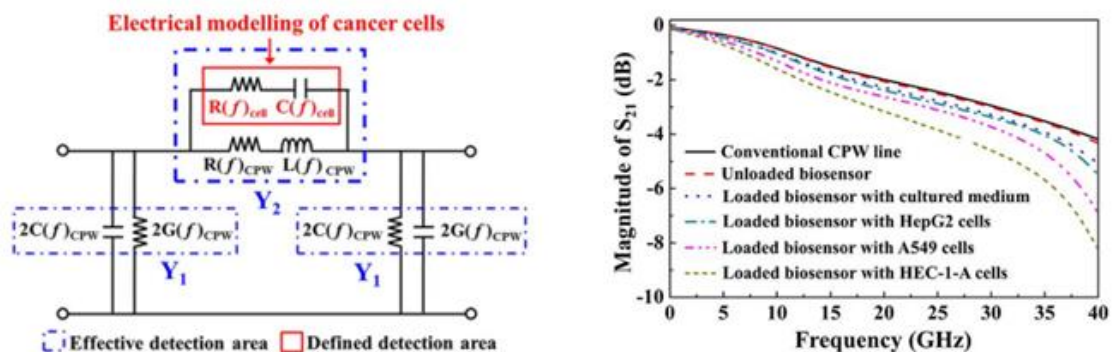


Figure 5: a) Electrical modeling of cancer cells [32] b) Measured S_{21} magnitudes of different cells [32].

The observed results can be seen in Figure 5b. In these results one can see that the different cancer cells are frequency dependent and results in different reflection coefficients.

A different type of capacitive sensing is based on the interdigitated Electrodes manner. Here an interdigitated capacitor is embedded in a LC tank of a voltage-controlled oscillator (VCO), see Figure 6. This VCO will be placed in a phase-locked loop (PLL) configuration. By applying a medium on the interdigitated capacitor, the permittivity of the capacitor changes and this results in a change in the frequency, which can be detected [30, 35].

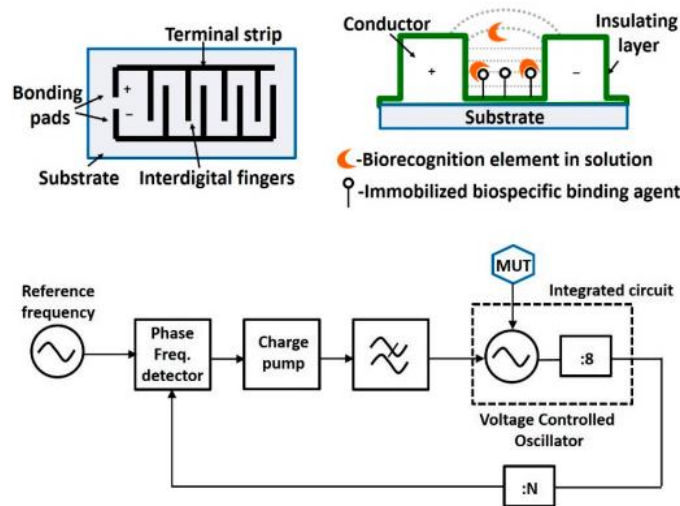


Figure 6: Schematic overview of the interdigitated electrodes based capacitive sensing method [33].

Besides the capacitive sensing techniques, there is also a radio-frequency identification (RFID)-based biosensor. This sensor uses the fact that the reflected RF signal strength varies with the change in concentration of an analyte. To do this, a dipole antenna is split and covers a nitrocellulose (NC) membrane. Then specific antibodies are placed on the surface of the NC membrane. The analyte will conjugate with antibodies to form a sandwich structure. Because of this, a silver enhancement process will take place, resulting in grow of the size of the silver particles. The growing particles will fall into the gap and form a complete dipole structure. Depending on the targets concentration, the growth strength of the RF wave will vary and therefore give an indication of the concentration [33, 36]. Figure 7 shows this process in a schematic way.

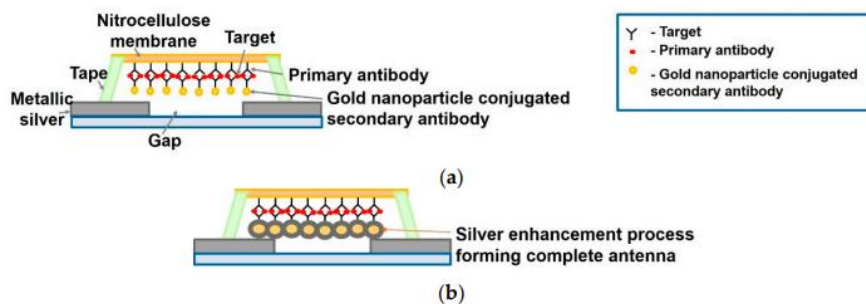


Figure 7: a) Antibodies are binding to the target b) Silver enhancement process is achieved [33].

Another sensing technique is possible to perform epidermal impedance sensors for spatial hydration mapping. Figure 8 represents the cross-sectional implementation of two electrodes contacting the skin. By using different geometries and or frequencies it is possible to obtain the hydration level over large areas with uniform or different skin depths. With this the capacitance of the electrodes changes, which results in a measurement of different hydration levels [37].

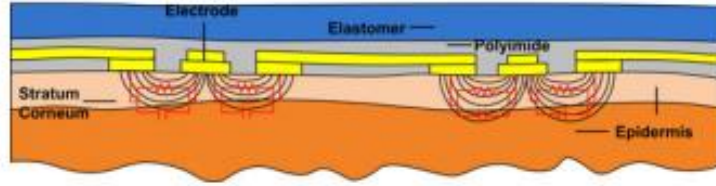


Figure 8: Diagram of skin integration and measurement principle [37].

With the use of finite difference time domain (FDTD) technologies and double Debye theory it is achieved to model the THz electromagnetic properties of the skin [38, 39]. Over the frequency band of interest is found that the water dielectric constants were 6.6 and 4.1 respectively and for the skin the values were found to be 3.6 and 3.0 respectively. From these results can be concluded that the skin can be modelled as a semi homogenous medium with a dielectric constant that is similar to liquid water. Also, the contrast in tissue imaging is primarily due to water concentration gradients. However, working in a higher frequency also gives a larger attenuation constant in the signal [40]. Hydration mapping of skin samples from chicken and porcine provide evidence that liquid water is a dominant contrast mechanism of the skin [41, 42].

Using a resonant microwave near-field sensing sensor enables a highly localized electric field. This can be achieved by introducing two resonators with different resonant frequencies, a sensing tip and a microfluidic channel [43]. This sensor makes it possible to detect a single-cell in the human body, the change in quality factor of the circuit and the frequency represents different liquid examples. This can be seen in Figure 9.

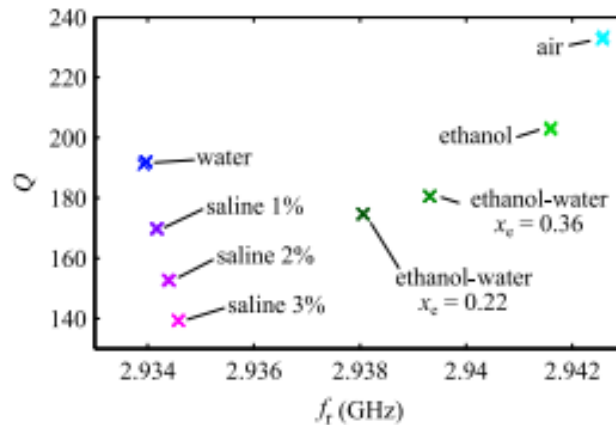


Figure 9: Measured resonant frequency versus quality factor for air and different liquid samples [43].

Different types of resonators exist. One of those resonators is the split ring oscillator for sensing a biomolecule through affinity binding on its surface. This type of resonator is a, so-called, affinity binding sensing system and works as follows; before the affinity binding of a molecule, the resonator will work at a specific frequency. When the affinity binding takes place (analyte binds on the sensors surface), the permittivity and/or permeability of the sensors surface changes resulting in the change of capacitance and/or inductance and thereby the resonance frequency. The frequency will change in the following way [44]:

$$f_{res} = \frac{1}{2\pi\sqrt{C_{eff}L_{eff}}} \quad (1.3)$$

In here, the effective inductance and capacitance of the resonator are geometry dependent on the split ring. Finally, Magnetic Induction Tomography (MIT) can be used for medical imaging applications. According to *Griffiths et al*, MIT applies a magnetic field from an excitation coil to induce eddy currents in the to be studied material and then the magnetic field from this is detected by sensing coils. MIT is able to detect the conductivity, permittivity and permeability of the material under interest (MUT). Besides the Magnetic Induction Tomography various techniques from the basic of MIT exists, which are called Mutual Inductance Tomography and Electromagnetic Tomography [45, 46].

With the open ended coaxial cable, it is possible to measure the reflection coefficient and relate this to the complex permittivity of the sample by using a suitable analysis ($\epsilon^* = \epsilon' - j\epsilon''$). The radius of the open ended coaxial cable is related to the penetration depth of the sensor (i.e. $\approx 7\text{mm}$) [47]. The sensor is placed on four different places in a male individual. The results of the permittivity can be seen in Table 1.

Table 1: Complex permittivity of the human skin measured in vivo [47].

$f(\text{MHz})$	Palm (thumb base)				Temple (forehead)				Neck (thyroid)				Abdomen (liver)			
	ϵ'	$\Delta\epsilon'$	ϵ''	$\Delta\epsilon''$	ϵ'	$\Delta\epsilon'$	ϵ''	$\Delta\epsilon''$	ϵ'	$\Delta\epsilon'$	ϵ''	$\Delta\epsilon''$	ϵ'	$\Delta\epsilon'$	ϵ''	$\Delta\epsilon''$
50	85.1	2.1	171.0	1.4	63.8	2.1	151.4	1.4	80.3	2.2	99.3	1.1	71.5	2.2	106.3	1.1
100	65.7	1.1	96.0	0.7	48.8	1.0	81.7	0.7	50.9	1.2	59.1	0.7	48.6	1.0	60.9	0.6
200	54.9	0.6	53.8	0.4	41.6	0.6	44.1	0.5	38.6	0.6	33.3	0.5	39.2	0.6	33.9	0.3
300	50.9	0.6	38.8	0.3	39.1	0.5	30.8	0.4	35.1	0.5	23.7	0.4	36.2	0.5	24.1	0.3
400	48.6	0.5	30.9	0.3	37.8	0.4	23.9	0.3	33.6	0.4	18.5	0.3	34.8	0.4	18.9	0.2
500	47.1	0.5	26.1	0.3	37.0	0.4	19.7	0.3	32.7	0.4	15.3	0.3	33.9	0.4	15.7	0.2
600	46.2	0.5	23.1	0.3	36.4	0.4	16.9	0.3	32.2	0.4	13.3	0.2	33.3	0.4	13.5	0.2
700	45.7	0.5	21.0	0.3	36.0	0.4	14.8	0.3	31.7	0.4	11.6	0.2	32.9	0.4	11.9	0.2
800	45.2	0.5	19.7	0.3	35.6	0.4	13.2	0.2	31.3	0.4	10.4	0.2	32.5	0.4	10.7	0.2
900	44.5	0.6	18.8	0.3	35.2	0.4	11.9	0.2	31.1	0.4	9.5	0.2	32.2	0.4	9.7	0.2
1000	43.5	0.6	18.0	0.3	34.7	0.4	10.9	0.2	30.2	0.4	8.6	0.2	31.7	0.4	8.9	0.2
1100	43.2	0.6	17.2	0.2	34.6	0.4	9.9	0.2	30.2	0.4	7.8	0.2	31.6	0.4	8.2	0.2
1200	42.7	0.6	16.5	0.2	33.9	0.4	9.1	0.2	30.0	0.4	7.2	0.2	31.3	0.4	7.6	0.2
1300	42.2	0.6	15.9	0.2	33.7	0.4	8.4	0.1	29.8	0.4	6.7	0.1	31.1	0.4	7.1	0.1
1400	41.6	0.6	15.1	0.2	33.4	0.4	7.7	0.1	29.7	0.4	6.3	0.1	31.0	0.4	6.5	0.1
1500	41.5	0.6	14.5	0.2	33.2	0.4	7.1	0.1	29.5	0.4	5.8	0.1	30.8	0.4	6.0	0.1
1600	41.4	0.6	14.3	0.2	33.0	0.4	6.6	0.1	29.3	0.4	5.5	0.1	30.5	0.4	5.6	0.1
1700	41.3	0.6	14.2	0.2	32.7	0.4	6.1	0.1	29.1	0.4	5.1	0.1	30.4	0.4	5.2	0.1
1800	40.9	0.6	14.3	0.2	32.6	0.4	5.7	0.1	29.0	0.4	4.8	0.1	30.2	0.4	4.8	0.1
1900	40.3	0.6	14.0	0.2	32.3	0.5	5.2	0.1	28.8	0.5	4.4	0.1	29.9	0.5	4.3	0.1
2000	39.8	0.6	13.6	0.2	32.0	0.5	4.7	0.1	28.7	0.5	4.0	0.1	29.8	0.5	3.9	0.1

Transferring the table into figures results to the figures given in Appendix A

Using confocal Raman spectroscopy makes it possible to measure *in vivo* the hydration gradients for the different layer of the skins. Figure 10 represents the approximated result of the confocal Raman spectroscopy [48]. In this figure can be seen that the hydration level increases with skin depth. Therefore, can be concluded that looking at the hydration level in the lower part of the epidermis layer or the dermis layer is more convenient for measuring the hydration level differences.

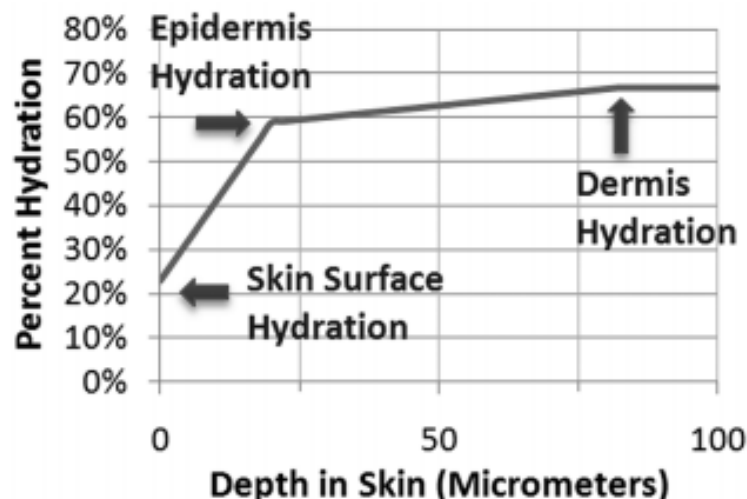


Figure 10: Approximated water concentration profile in the skin [48].

2.2 Medical diagnostics

The above-mentioned sensing techniques can lead to medical diagnoses. For instance, the MRI makes it possible to detect different materials in the human body (cancer, healthy tissue etc). Depending on the coefficients (k_1 , k_2) and the scan time of the MRI different weighted images can be obtained (T_1 , T_2 and PD) [49].

Measuring the dielectric permittivity of tumour cells (cancer) and normal tissue in a frequency range of 0-17 GHz makes it possible to distinguish these two types of tissue [50]. Figure 11 represents the results of the dielectric permittivity for the frequency range of 0-17 GHz for three different types of tumour cells with as reference the skeletal muscle (normal tissue).

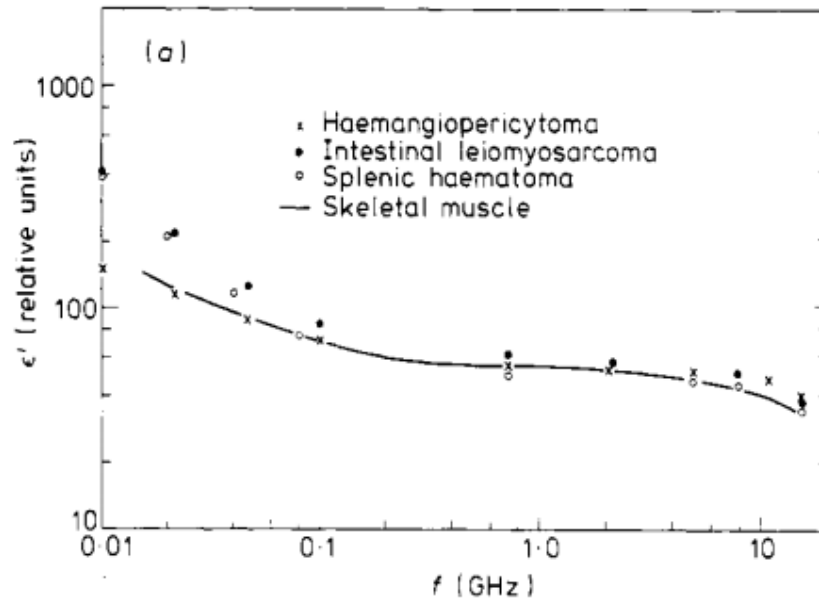


Figure 11: Dielectric permittivity from three representative tumour tissues, with the locus of the data from dog skeletal muscle shown for comparison [50].

Ex vivo theoretical analysis together with simulations describes the radiation of a source located close to the artificial dielectric layers. This provides evidence for distinguishing the different dielectric layers [51]. *In vivo* measurements using multifrequency impedance spectra for electrical bio-impedance enables to distinguish skin cancer from normal tissue. The resulting accuracy allows to distinguish malignant melanoma from benign nevi tissue and is found to be 75% for a sensitivity of 100% and between nonmelanoma skin cancer and benign nevi is 87% at a sensitivity of 100%. With these results, the cancer skin detection is as good or even better than the conventional screening (screening by visual interpretation) [52]. The single-cell detection in the above-mentioned section also detects cancer cells, depending on the resonant frequency and quality factor of the system [43].

Besides detecting cancer cells, permittivity detection can be used for monitoring the blood glucose concentration. Different glucose concentrations are measured over the frequency range of 500 MHz till 20 GHz. From Figure 12 the dependence of the glucose concentration on the frequency can be seen. This can distinguish different glucose concentrations at the same frequency and even a relation between the frequency and the glucose concentration in the blood [53].

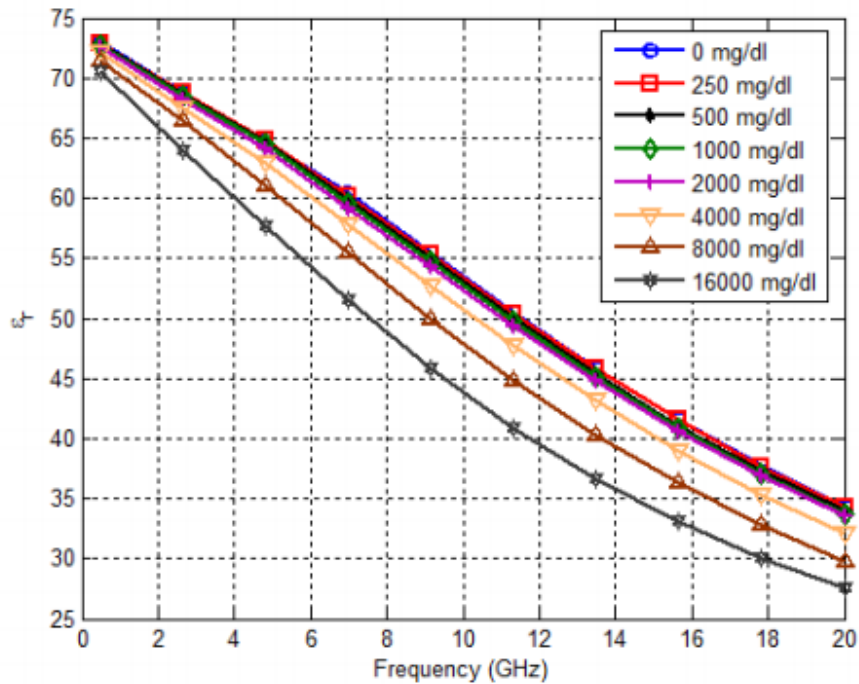


Figure 12: The measured dielectric constant from 500 MHz to 20 GHz for various glucose levels [53].

Furthermore, it is found that THz imaging signals are useful in the skin burn process of animal tissue. In these studies, it is found that the reflection of the THz waves is correlated with the burn degree of the skin. The burned part of the skin contains less water and is therefore less reflective [54].

Another application of the THz imaging can be used for the cornea hydration level. Hydration loss in the cornea can lead to deforming of the cornea from its spherical shape and eventually to loss of sight [40]. From recently published data, it can be observed that THz imaging applied to the cornea while considering water to be the dominant contrast mechanism may provide that the hydration sensitivity is superior to other known diagnostic systems [55].

Currently, pressure ulcers will be detected by visual aspects and tactile changes on the skin. However, below the skin. Pressure ulcers can be detected more rapidly than outside changes. By detecting these changes faster it is possible to treat the patient quicker and prevent significant costs [56].

Figure 13 presents a diagram for the physiological events that occur in pressure ulcers [56]. By using a permittivity sensor, it is possible to detect the pressure ulcers below the skin surface. Leading to a reduced procedure plan for the patient. Moreover prevention of pressure ulcers provides cost savings compared to treatment [57, 58]. Prevention is estimated to cost 2.65 up to 87.57 euro per patient per day, but treatment can cost 1.71 up to 470.49 euro per patient per day [58].

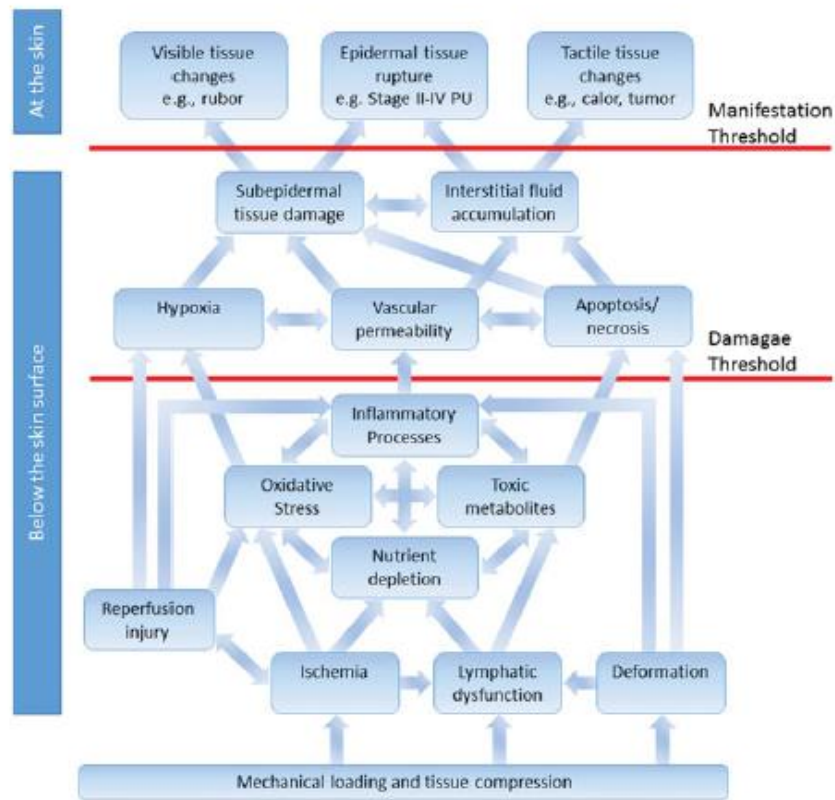


Figure 13: Conceptual framework for physiological processes leading to pressure ulcer development [56].

As mentioned in the skin physiology section, sweat is greatly related to the hydration level of the skin due to its thermal regulation. This makes it possible to connect sweat with disorders, which can eventually be connected to the hydration level of the skin. Impaired neurogenic sweating can be the earliest signs of various autonomic neuropathies as well as neurodegenerative disorders which can significantly reduce the quality of life [59]. Sweating is also an indication for the disease called cystic fibrosis. Defective sweating is an inseparable component of the constellation of symptoms for diagnosing cystic fibrosis [60]. Moreover, does hyperhidrosis affect the palms and soles with excessive sweat dissipation and can be associated with previous spinal cord injuries, peripheral neuropathies, brain lesions, intrathoracic neoplasm, systemic illness and gustatory sweating. On the other hand, hypohidrotic disorders include anhidrotic ectodermal dysplasia, hereditary sensory neuropathy, Holmes-Adie syndrome and generalized anhidrosis [61].

Besides detecting diseases, the hydration level detection is also useful in the athletic world. Athletes may not consume enough fluid and supplements, during training and competition, which can lead to decrease in their competition performance [62]. To detect the insufficient amount of fluid, the microfluidics in the athletes sweat are measured. Some of these important microfluidics are: ethanol, sodium, chloride, ammonia and urea [63]. Measuring the sweat rate and the microfluidics can give a correlation between the dehydration rate and sweat and/or microfluidics rate.

3. Encapsulation technique for the CMOS permittivity sensor

When considering contacting sensor an encapsulation technique should be devised in order to protect all the functional part of such sensors, i.e., bondwire, and other sensitive components. In this chapter we will first discuss the CMOS sensor used in this work (the Essense sensor) and the packaging flow that was developed at the Else Kooi Laboratory to allow a proper encapsulation of the sensor and allow direct contact testing.

3.1 CMOS permittivity sensor

The implementation of the permittivity sensor uses a double balanced Wheatstone bridge (see Figure 15.) with multi-harmonic down-conversion scheme (see Figure 16). This permittivity sensor makes it possible to obtain a high-resolution permittivity readout across a frequency range of 0.1-10 GHz [64]. The sensor architecture consists of a near-field, single-ended patch sensor, a RF-driven impedance bridge in a double-balanced configuration and a multi-harmonic IF down-conversion scheme. The sensor is able to measure in the fundamental frequency of 0.1 to 5 GHz and also the third and fifth harmonic components, which are located in the range of 0.1-10 GHz. The power consumption from a 1.1 Volt supply is 1.2 mW for 0.1GHz and 24 mW for 5 GHz [27, 64, 65]

3.1.1 Architecture of the permittivity sensor

The CMOS permittivity sensor represents a 25 pixel with 5x5 microwave permittivity sensor matrix [65]. The sensor matrix readout can be seen in Figure 14. In this 5x5 microwave permittivity sensor matrix, each sensor is connected to a double-balanced Wheatstone bridge by using a clipping RF buffer. This provides fundamental and harmonic output voltage, depending on the load of the patch. A dummy bridge is introduced to perform differential readout, which cancels the common-mode signal. The Y_B 4-bit binary capacitors are introduced to allow dynamic tuning ($Y_B = Y_L$), from Figure 15. The g_m stages provide voltage to current conversion. The RF switch selects the polarity of the selecting pixel and mixes the signal into an IF frequency. The TransImpedance Amplifier (TIA) converts the IF current to a voltage output. A Serial Peripheral Interface (SPI) is used to communicate with the chip.

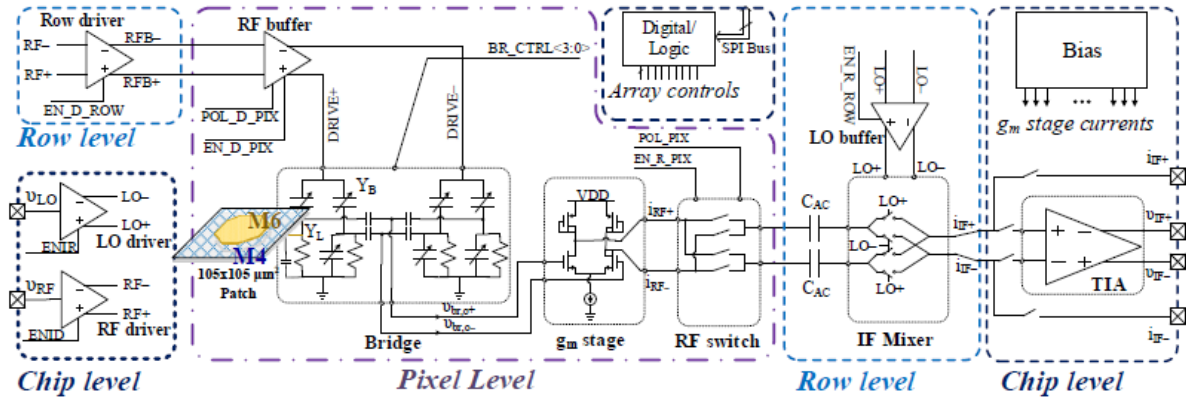


Figure 14: Sensor matrix readout architecture [65].

3.1.2 Circuit analysis of the differential double balanced bridge

The differential Wheatstone bridge will be discussed in this section. Figure 15 shows the final full differential bridge with attached patch. The output of the bridge can be defined as:

$$\Delta v_{b,o} = v_{b,o+} - v_{b,o-} = v_{in} \frac{Y_L}{4Y_o + 2Y_L} \quad (1.4)$$

Here, Y_L is the load admittance occurring due to the patch connection. Y_o are the admittances of the balanced Wheatstone bridge, which are defined as follows. $Y_L = G_L + jB_L$ and $Y_o = G_o + jB_o$, where B_o and B_L are ωC_o and ωC_L respectively.

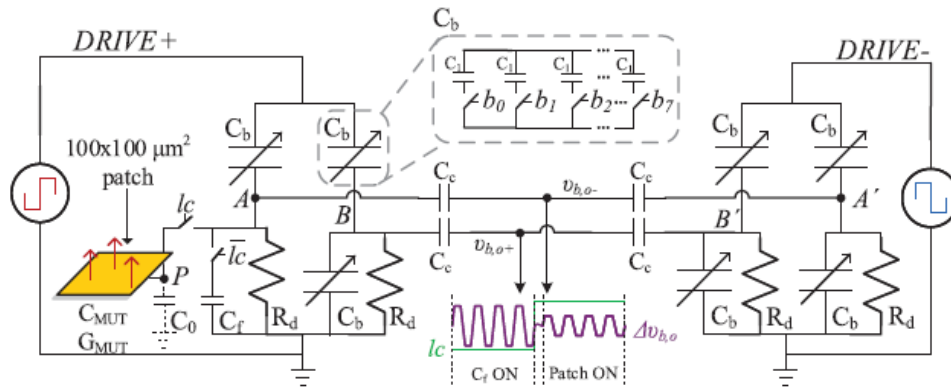


Figure 15: Schematic of the implemented fully differential double balanced bridge [64].

The use of a double-balanced RF bridge is chosen to improve the linearity and results in giving a differential output for the following stages [27]. Furthermore, it was chosen to make each capacitor of the differential double-balanced tuneable for better matching which results in greater sensitivity.

3.1.3 Circuit analysis of the down-conversion mixer

The output of the differential bridge is in the RF range and needs to be down-converted in order to digitize and to perform further analysis. This down-conversion mixer can be seen in Figure 16. In this figure, the LO signal is generated as a square wave, which results in a greater conversion efficiency [66, 67]. With the use of the Q1 and Q2 transistor the voltage from the differential bridge will be converted to current. The transistor Qs is used for biasing. The output current i_{RF+} and i_{RF-} are fed to the switching quads which perform the mixing operation. Capacitive coupling between this action is used to prevent DC current flow to the quads (which creates flicker noise) [68]. The resulting current can later be converted to voltage or can be read out as current [64].

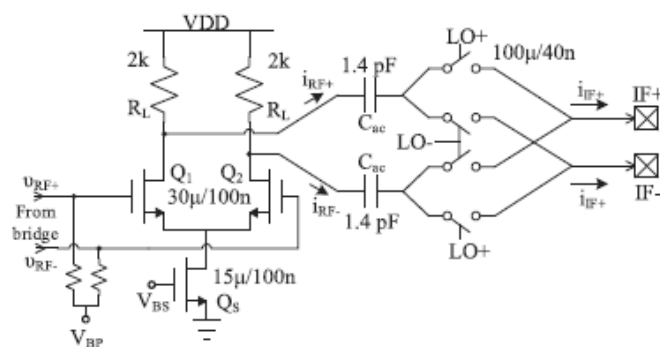


Figure 16: Current-mode down conversion mixer schematic [64].

3.1.4 Calibration procedure

The real and imaginary outputs of the differential bridge are linear combinations of the load conductance and susceptance. These outputs make it possible to perform a linear fitting procedure by the use of a linear fitting algorithm. In this way, calibration can be used for the system. To find the optimum calibration values, a calibration procedure can be defined as follows:

1. Apply a set of known load values $Y_{L,cal}$ and measure the sensor output.
2. Search for the combinations of the coefficients for the linear calibration curve by using the adjusted R2 as a fit merit figure.
3. Store these coefficients as the calibration values of the chip.

These coefficients are specific for each certain frequency. The Y_{off} represents the amount of load that should be added at the patch mode [64].

3.1.5 Experimental results

Figure 17 represents the results of the measured permittivity of ethanol versus the frequency. This graph shows the fundamental excitation from 0.1 to 5 GHz, while the third and fifth harmonic are expanding over the full range of 0.1 to 10 GHz. In this figure can be seen that the reference value lies within the measured values for the real permittivity. However, the imaginary part of the permittivity shows a little deviation which is tolerable [27].

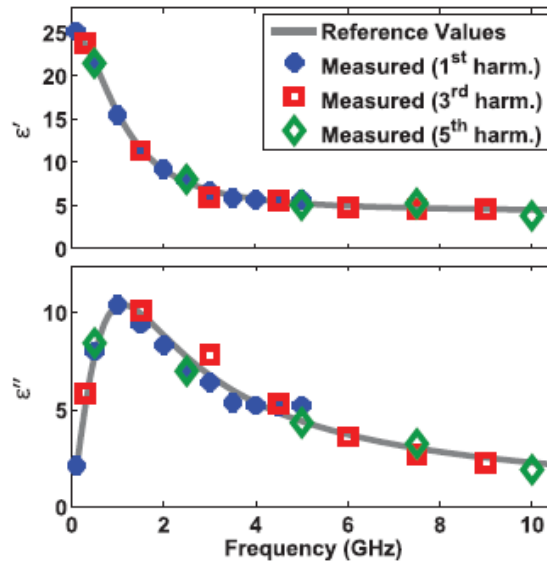


Figure 17: Ethanol permittivity measurement versus frequency [64].

The integrated microwave permittivity sensor implementation can be seen in Figure 18.

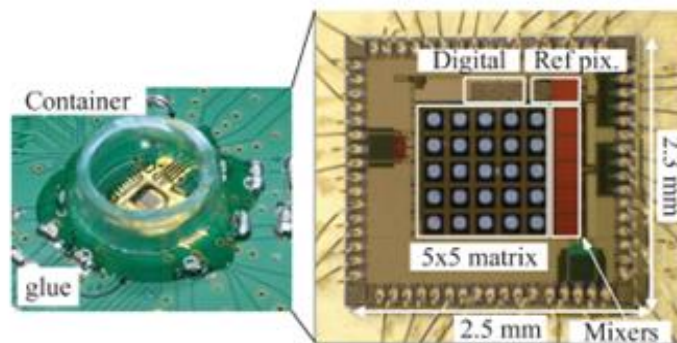


Figure 18: 5x5 permittivity sensing array [65].

3.1.6 Packaging of the CMOS permittivity Sensor

The wafer with the available prototype dies is given in Figure 19. Although this is not a complete count. There are more than $21 \times 15 = 315$ dies of the sensor chip on the wafer. As can be seen in Figure 19a, the wafer is taped to a plastic holder.

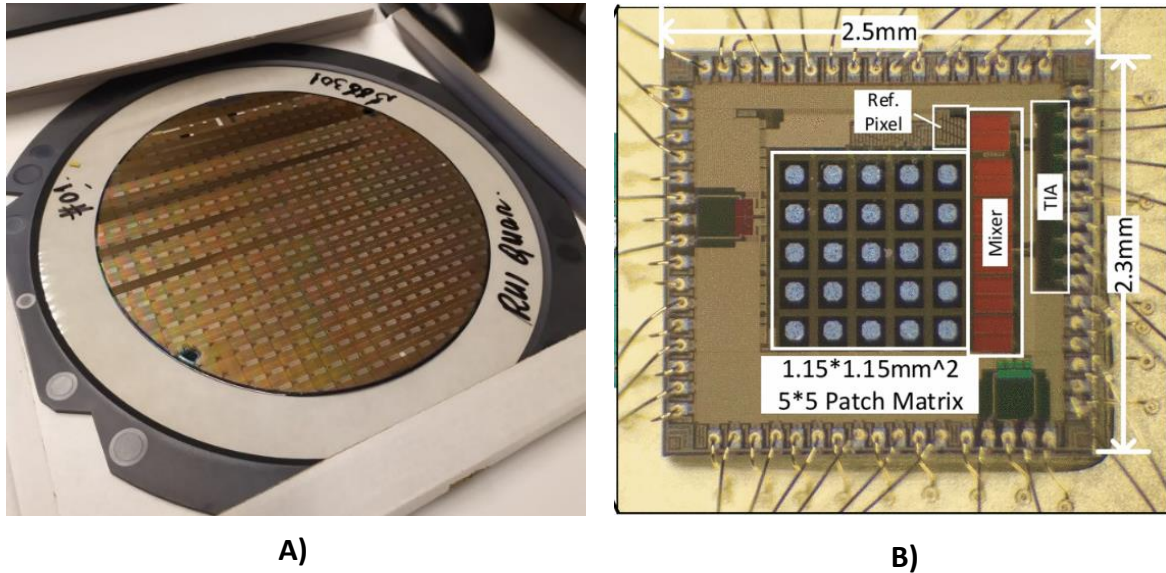


Figure 19: a) Wafer with available chips b) The dimensions of the chip and array [65].

The thickness of the wafer and thus of the prototype integrated circuit is measured by inserting a die containing a circuit of a different participant in a caliper as shown in Figure 20. The measured thickness of the prototype dies that will be used in the intended packaging, is approximately $\pm 400 \mu\text{m}$.



Figure 20: Thickness of die of other participant measured using caliper.

A graphical representation of a 2x2 array of the 5x5 array sensing patches of the CMOS permittivity sensor can be seen in Figure 21.

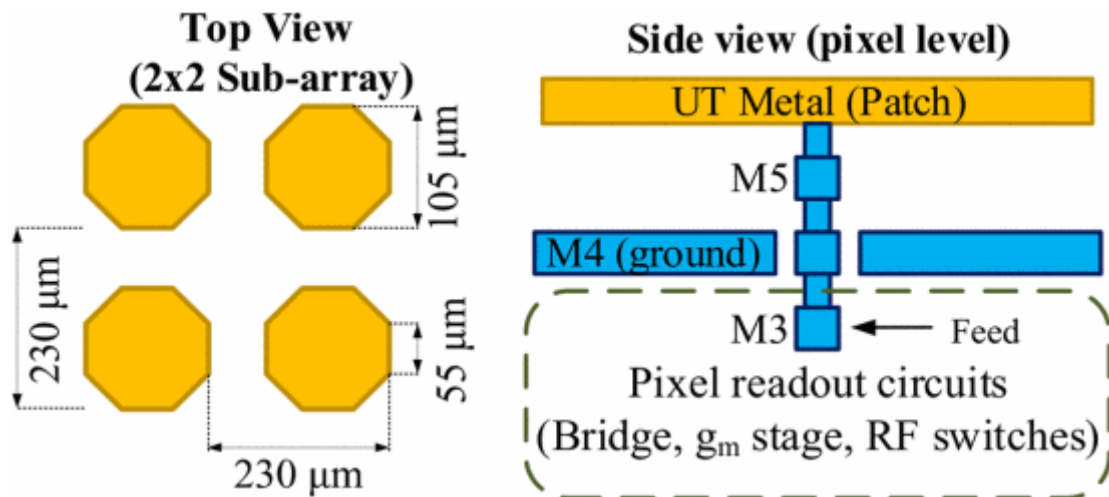


Figure 21: Top view and side view of the patches in the 5x5 array CMOS permittivity sensor [65].

These dimensions are crucial for the packaging procedure of the chip. Besides the provided dimensions of the CMOS permittivity, it is also given that the patches contain an aluminium alloy, namely aluminium with 0.5% copper. Furthermore, the 5x5 patch array is not located in the middle of the CMOS permittivity chip.

3.2 Packaging solutions of the CMOS permittivity sensor

Protecting the bondwires of the CMOS permittivity sensor (see Figure 18), which are at least 200 μm high, by creating a height difference between the chip surface and measurement surface can be achieved using different packaging solutions. Three of these possible solutions will be examined in the following sections. The first solution is the creation of SU8 metalized pillars. The second solution consists of silicon pyramids with an aluminium layer. The final solution is a creation of cavities which can be filled with aluminium.

3.2.1 SU8 metalized pillars

To establish the height of the bondwires, a polymer called SU8 can be used. SU8 is mostly used to establish big structures with a large height/width ratio. An aluminium layer is required to create a contact between the underlying patch and the top of the SU8 pillars. A cross section image of this solution is shown in Figure 22.

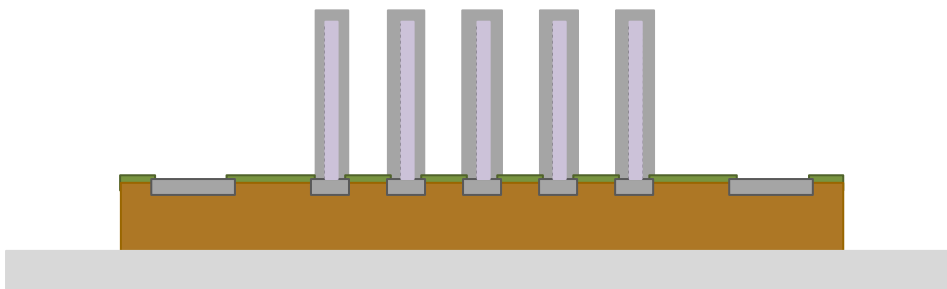


Figure 22: Cross section image of SU8 metalized pillars.

The positive aspect of this solution is that SU8 is beneficial for the structures with a height/width ratio of 200/80. Another positive aspect is that SU8 is considered to be a polymer which has a high cure and attach rate to another substrate and finally after curing removal of SU8 can be considered as difficult. The disadvantage of this solution is that a uniformity of aluminium should be established around the SU8 pillars on the patch. Also is there a chance that the SU8 pillars can collapse when pressure is applied on the pillars. Therefore, a filling is required between the patches to encapsulate the pillars.

3.2.2 Metalized silicon pyramids

The height of the bondwires can also be achieved by creating silicon pyramids. First a layer of silicon is deployed on the chip. Etching this silicon layer in a tetramethylammonium hydroxide (TMAH) or potassium hydroxide (KOH) solution occur in creation of pyramids. After the creation a metallization layer should be deployed on the pyramids to enable contact between the pyramid and the patch. This solution can be seen in Figure 23.

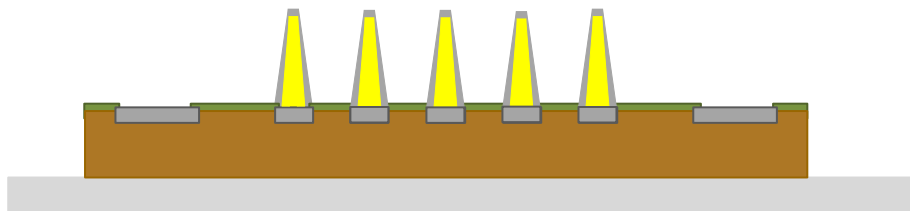


Figure 23: Cross section image of metalized silicon pyramids.

The advantage of this approach is that the pyramids are more robust, resulting in no necessary need of pyramid encapsulation. The third advantage is that the coverage of aluminium on the pyramids is more equal than the coverage is for SU8 pillars. The disadvantage is that using KOH for etching silicon will also etch the aluminium [69], thereby removes the aluminium for the bondwire connections and at the patch sides next to the pyramids. Because of this effect, the packaging solution of metalized silicon pyramids is not further considered.

3.2.3 Filled aluminium cavities

The third solution is to create cavities in SU8 on the underlying patches for the bondwire connections. These cavities can be filled with aluminium to create a connection between the underlying patch and the created aluminium pillar. This packaging can be established by applying a SU8 layer on the chip to create cavities. This packaging solution can be seen in Figure 24.

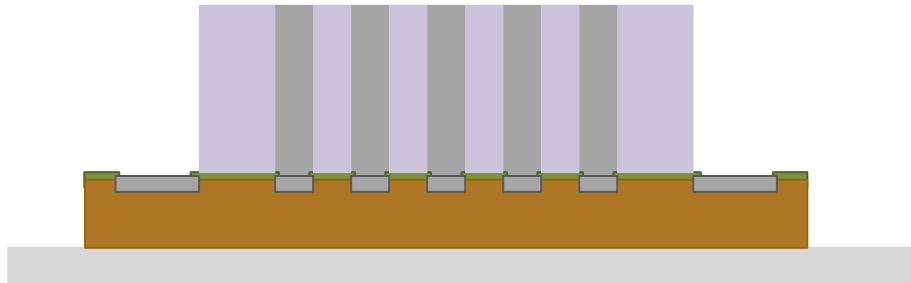


Figure 24: Cross section image of cavities filled with aluminium

This procedure has the same advantages for SU8 as the first procedure. Another advantage is that the connection between the patch and the top, where the measurement will occur, is certainly there. The disadvantage of this procedure is that there must be a process that is able to fill these cavities with aluminium particles.

3.3 Processing steps

In the previous section different packaging solutions are described with their advantages and disadvantages. Within this thesis work the first (Figure 22) and the last (Figure 24) packaging solution have been developed and the custom developed flowchart has experimentally been tested. The processing steps for these procedures will be discussed below.

3.3.1 Procedure steps for creating SU8 metalized pillars

First the processing steps of the packaging procedure should be defined. A visual representation of the packaging steps are given in Appendix B.1

The process of the chip will start by gluing the chip on the carrier wafer. If the chip is ready to use the bondwires will be attached to the chip this results in bondwire height of at least 150 μm . To be sure that the bondwires will also be encapsulated and that the patches are laying in a higher field than the bondwires, there is chosen to use a SU8 pillar height of 200 μm . SU8 will be coated by using the manual brewer spinner and by applying a droplet of SU8 in the middle of the wafer.

After the coating of SU8, alignment should take place to create the 200 μm SU8 pillars on the patches. These pillars should be created on the patches. However, they should not be as large as the patch radius, but a little bit smaller to ensure that there is enough space left for the metallization step. To perform this exposure of the alignment the EVG420 contact aligner will be used.

To make sure that the SU8 pillars will be staying on the patches and to remove the any remains of the SU8 at the other places, development should take place. Development of SU8 will occur when using propylene glycol methyl ether acetate (PGMEA) developer.

To assure the contact between the aluminium patches and the SU8 pillars, it is convenient to sputter aluminium on the SU8 pillars. This sputter will occur with an alloy of aluminium with 1% silicon. A metallization sputter thickness of 4 μm thickness is used.

However, after the sputtering of aluminium there is still some aluminium between the patches. This could create one large patch instead of the 25 separate patches. To prevent this, the aluminium should be removed between the patches and the outside of the patches area. To make this possible, a photoresist layer should be spray coated on the wafer. Here the AZ9260 positive photoresist will be used for defining the regions that should be etched away and which should stay.

With the applied positive photoresist, it is possible to define the regions that should be etched and the regions that should not be etched. This can be achieved by using a different mask than the previously used mask for SU8 and again use the EVG420 mask aligner. There should be photoresist left on the metalized SU8 pillars and the remaining of the aluminium should be removed.

Before removing the additional aluminium between and around the patches, the photoresist should be developed to distinguish between the areas where the aluminium should be etched away and the area where the metallization should be left. This accomplished by using the AZ Developer.

Now, etching the aluminium can occur. This will take place by performing wet aluminium etching. The final step in creating the SU8 metalized pillars, is the removal of positive photoresist remnants. This can be done by rinsing the wafer with the chip in a bath of acetone.

After finalizing the SU8 metalized pillars, it is possible to place the chip on the PCB board design. Before this can be done the SU8 metalized pillars should be encapsulated to ensure that the pillars will not collapse when exposed to stress at the surface of the metalized SU8 pillars. This can be accomplished by performing a capsule with a compound adhesive between the pillars.

The chip can now be cut from the carrier wafer. Now the chip can be placed on the PCB board design at the located place. Thereafter, the bondwires can be attached to the chip and the PCB. Finally the entire chip with the bondwires can be encapsulated with a compound glue. This can be done with the same glue as used to encapsulate the SU8 metalized pillars. However a different compound glue could also be used.

3.3.2 Procedure steps for creating cavities in SU8

The start of the cavity filling process with metal is according to the same procedure as creating the SU8 metalized pillars. First, the chips are glued onto the wafer. It should be noted that instead of the mask used to create the SU8 pillars, a different mask is required. A visual representation of the packaging steps are given in Appendix B.2.

The process of the chip will start by gluing the chip on the carrier wafer. If the chip is ready to use the bondwires will be attached to the chip this results in bondwire height of at least 150 μm . To be sure that the bondwires will also be encapsulated and that the patches are laying in a higher field than the bondwires, there is chosen to use a SU8 pillar height of 200 μm . SU8 will be coated by using the manual brewer spinner and by applying a droplet of SU8 in the middle of the wafer.

After the coating of the SU8, alignment should take place to create the 200 μm SU8 pillars on the patches. These cavities should be created on the patches. However, they should be larger or the same size as the patch radius. This to ensure that metallization is deposited on the entire patch size.

To remove the unexposed SU8, a development in PGMEA is required.

To finalize the process, the cavities should be filled with aluminium particles to generate a contact between the patch and the top part where measurements are performed. Resulting in the final cross section representation.

3.4 Custom developed packaging flowchart

To be able to process wafers in a clean environment, such as the cleanroom, a flowchart is required. This to ensure that no contamination or dangerous process will occur. This flowchart should be approved and followed while working in the cleanroom environment. The flowchart can be found in Appendix B.3

3.5 Mask design

Looking at the process steps for both generation of the SU8 metalized pillars and metal filled cavities results in the use of two masks for the SU8 metalized pillars and the use of one mask for the generation of the cavities. To fasten the process, it is chosen to design a 3x3 array with chips in such a way that more chips can be processed for the use of one wafer. Nevertheless, it is inconvenient to place the chips in a 3x3 array close to each other. This because the mask alignment machine uses two microscopes to be able to align with a more accurate field of view, which cannot overlap. Therefore a wider 3x3 array is created.

The Tresky T-6000-L [70] machine can be used to pick and place the chips in a given array to create a 2x3 chip array, instead of the designed 3x3 mask array. This due to the fact that the machine is not able to place chips next to each other.

3.5.1 Masks for SU8 metalized pillars

The first mask to create the SU8 pillars can be seen in Figure 25. There is chosen to have the standard alignment markers on both sides of the wafer. Besides the standard alignment markers, on both sides of the wafer, there are also alignment markers present on one of the patches for the most upper left and upper right chip. A more detailed mask design for the most upper left and upper right chips can be seen in Figure 26.

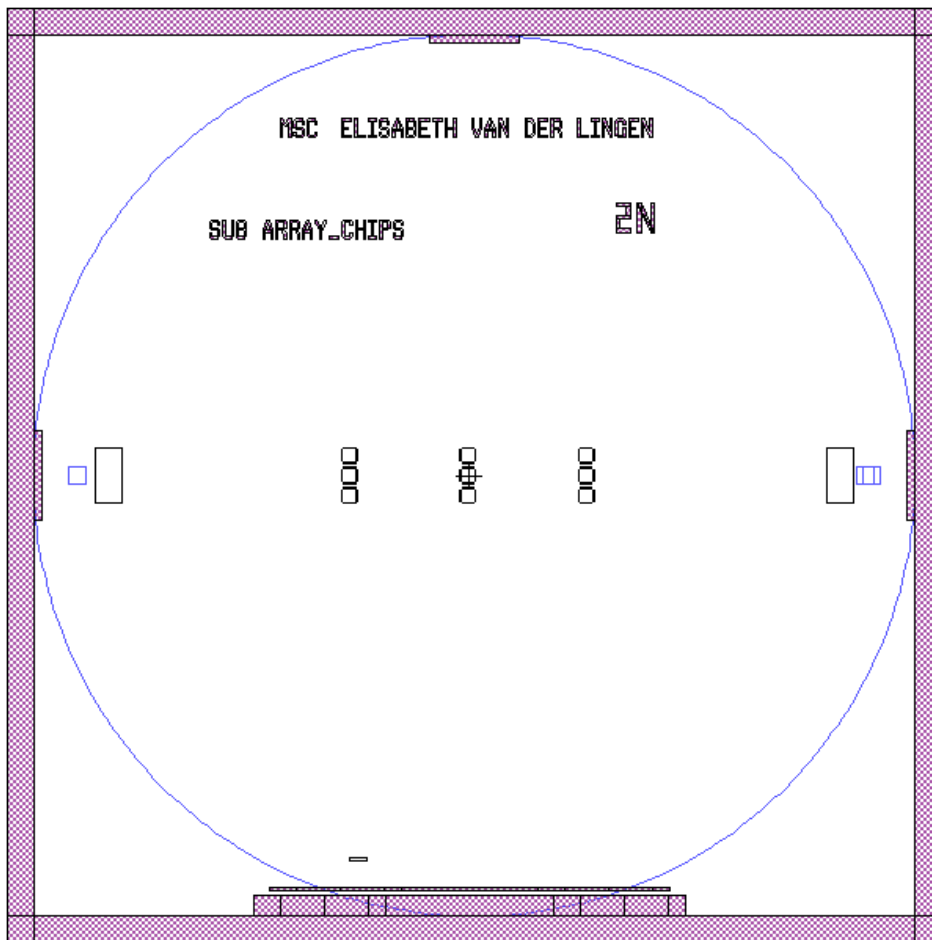


Figure 25: Overview of the mask design for creating SU8 pillars.

To properly align the chips, it is decided to sacrifice two patches in the most left upper chip and most right upper chip. Here can be seen that the upper left and upper right mask patches are designed in such a way that they are larger than the 105 μm wide patches of the chip.

This mask has a negative emulsion down polarity, meaning that the drawn figures will be see-through when exposing the mask to light. With this in mind, the patch of the chip (105 μm octagonal) can be seen through the 125 μm octagonal created for the mask, resulting in an alignment marker for all of the 2x3 designed chip array. Besides the alignment marker sizes there is also chosen to design the SU8 pillars with a diameter of 80 μm . This leaves space for the metallization step where a contact should be created between the patch surface and sputtered aluminium with 1% silicon.

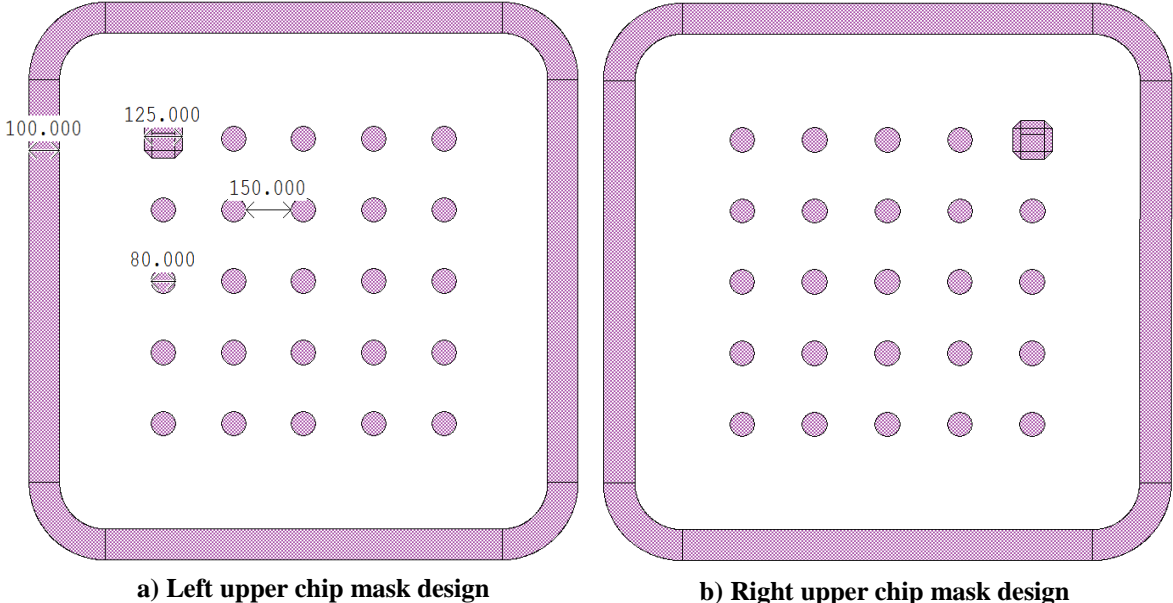


Figure 26: Mask design for single chip to create SU8 pillars.

The second mask is regarding the metallization step as explained in section 3.2.1. This mask has a positive emulsion down polarity. This results in a see-through field around the illustrated figures, which can be seen in Figure 27. The crosses are designed in a way to be able to recognize the SU8 octagon on the chip.

Also, it can be seen that the radius of all the circles is 125 μm , which are larger than the diameter of the patch on the chip (105 μm) and also bigger than the SU8 circle pillars diameter (80 μm). This to enable contact between the patch of the chip and the top of the SU8 pillar.

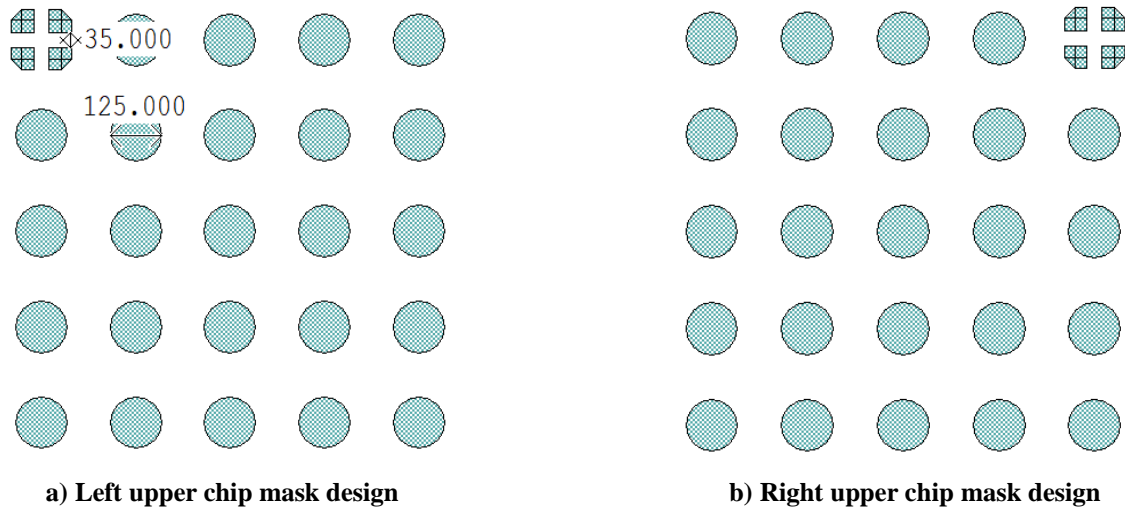


Figure 27: Mask design for single chip to create metallized pillars.

When overlapping the layers for the different sizes and alignment markers Figure 28 can be examined to give more insight.

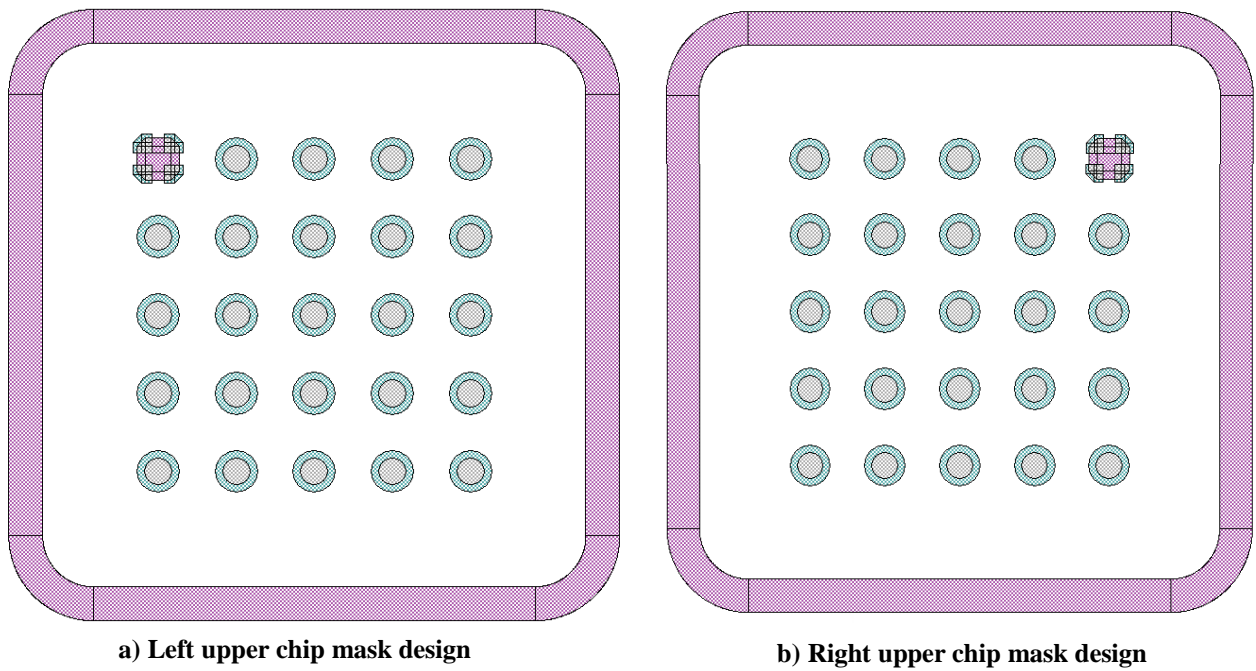


Figure 28: Mask designs for single chip to create metallized SU8 metalized pillars.

3.5.2 Mask for creation cavities in SU8

The third and final mask is regarding the creation of cavities in a SU8 layer. The overall view of this mask can be seen in Figure 29. In this mask, the same standard alignment markers on both sides of the wafer are used. However, in this mask two patches of the chips do not have to be sacrificed.

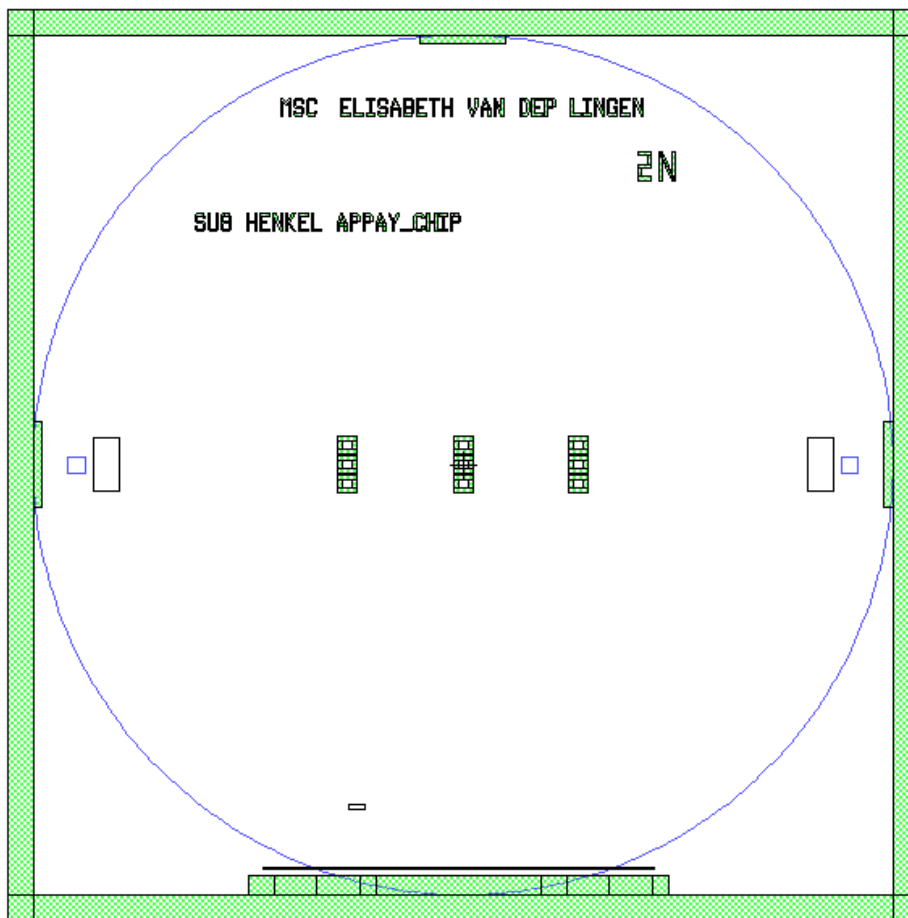


Figure 29: Overview of mask for creation cavities in a SU8 layer.

Figure 30 shows a more detailed mask design for one chip. Here is shown that no alignment markers in octagonal shape are present. This is due to the fact that this mask is created with a negative emulsion down polarity, resulting that the open circles will be a dark field of view. Furthermore are these diameter circles larger than the 105 μm octagonal patches on the chip. Resulting that when applying this mask it will not be able to see the patches around the 110 μm circles, which results in a good alignment.

An important note is that the SU8 should not be applied on the bondwire patches around the chip. This is achieved by creating the 685 μm horizontal distance on the right side and a 585 μm horizontal distance on the left side of the last circle. Also, the vertical distance is created to be 2100 μm , which leaves 100 μm on both sides for the bondwire patches.

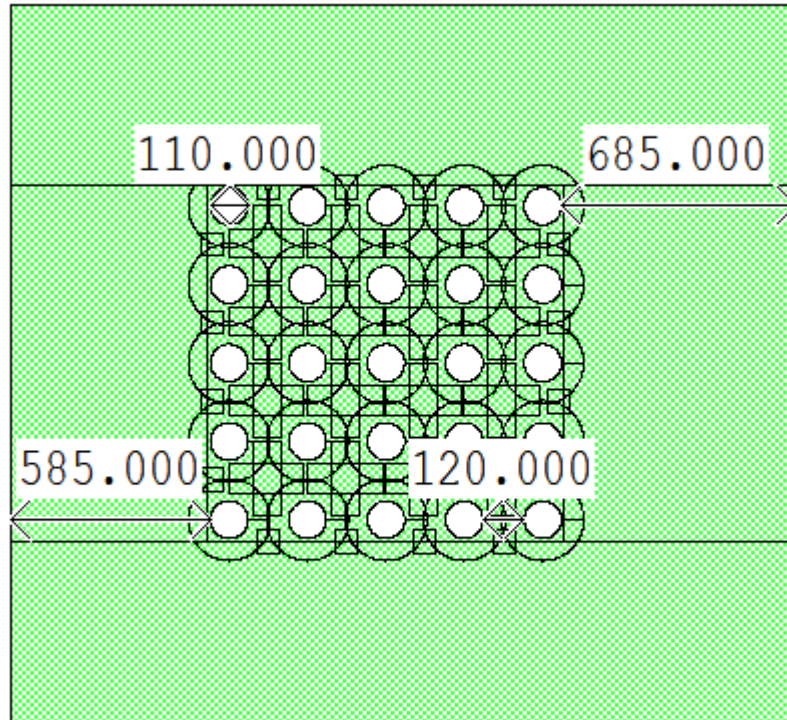


Figure 30: Single chip mask to create cavities in SU8.

3.6 Results

Before processing the wafers with the attached chips, several tests with dummy wafers, where no chips are introduced yet, are required. This to ensure the SU8 thickness and other parameters. First the results regarding these dummy wafers will be discussed and after this the results regarding the chips on the wafer are discussed.

3.6.1 Dummy wafer results

The process steps regarding the creation of the SU8 metalized pillars and the cavities in SU8 are examined.

3.6.1.1 Wafers with SU8 metalized pillars

The influence of different processing steps on the properties of the resulting structures are examined in this section. The first process that influences the structures of the SU8 pillars is the spinning and dispensing rate of the SU8 during the first coating step.

First the acceleration speed is examined regarding the height of the SU8 pillars. Following the processing guidelines according to MicroChem [71] a spin of 1300 rpm is desired to achieve a SU8 thickness of 200 μm .

The first trials with a spin speed of 1300 rpm show that a SU8 thickness of 127 μm is achieved. This shows that the chosen spin speed is too high. In the following iterations a spin speed of 1100 rpm and 800 rpm are investigated. The resulting SU8 height pillars for 1100 rpm in the vertical axis can be seen in Figure 31, which are measured using the Keyence VK-X250. The first vertical measurement is for the dike measurements which has a height annotated by [1] of 163 μm . The second vertical height measurement is of the fifth SU8 pillar, which is annotated by [3] with a height of 163 μm .

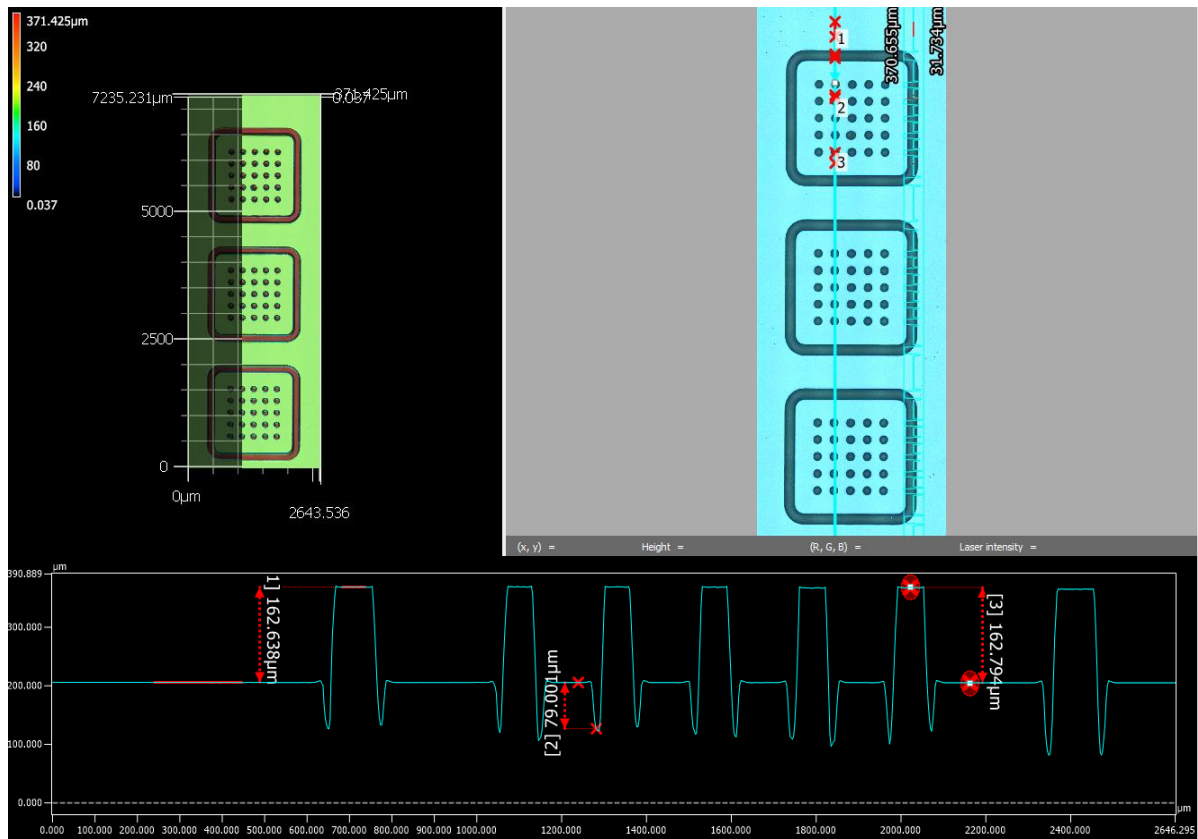


Figure 31: Vertical height measurements of spin coating SU8 with 1100 rpm.

Besides the vertical measurements of the spin coated SU8 at 1100 rpm, a horizontal measurement is performed. This vertical measurement can be shown in Figure 32. Here, also the first measurement is regarding the height of the dike, which is annotated by [1] and is given as 159 μm . The second measurement regarding the height of the SU8 pillars is annotated with [3] and given to be 158 μm .

To ensure that the optical and laser height measurements of the see through SU8 is performed in an accurate manner, a horizontal measurement is performed using the Dektak 8 profilometer. These measurements result in a dike height of 155 μm . Comparing these results with the height measurements of the Keyence VK-X250, results in an accurate height measurements for both the Keyence and the Dektak.

These results show that a spin speed of 1100 rpm is still too high to create a SU8 thickness of 200 μm . Another important note is that the height difference between the vertical measurements and horizontal measurements are not equal and have a deviation of approximately 3 μm , the same applies to the height of the dike and pillar. This is due to the fact that SU8 is a viscous liquid, which fluidity is tougher than honey. This fluidity results in a wavy behaviour of the SU8, resulting in a non-uniform more deviation height. Nevertheless, these differences are not considered to be harmful to the final packaging solution.

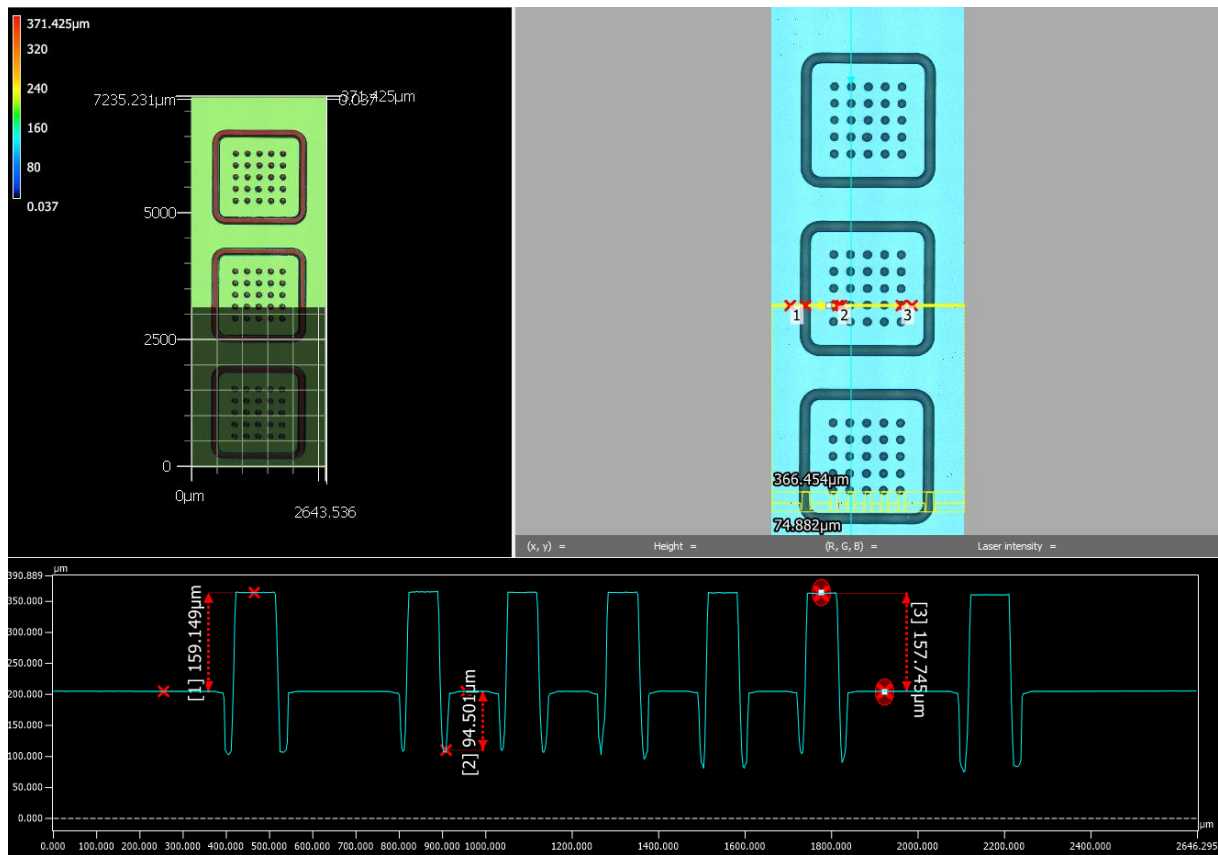


Figure 32: Horizontal height measurements of spin coating SU8 with 1100 rpm.

For the purpose of the processing steps there is chosen to show one full iteration. This iteration will be given with the 1100 rpm wafer. The other process for the 1300 rpm and 800 rpm can be seen in Appendix B.4.

SU8 metallization with 1100 rpm spin coating of SU8

In Figure 33a a total overview of a single SU8 chip coating with AL +1% Si is shown. Here the dike is still present due to the hard baking step that after development is extended with 20 minutes. Also, cooling steps are applied between the deposition steps. In Figure 33b, the dimension of a single pillar is given. This shows that the top diameter of the SU8 metalized pillar is 115 μm, while the bottom diameter is approximately 85 μm. This mushroom kind of shape is created by to the separation contact between the mask and wafer during exposure and/or too less development of the SU8. During exposure there is chosen to have a 30 μm separation between the mask and wafer. This separation is chosen, because if hard or soft contact is chosen the chance is that the SU8 will stick on the mask. Furthermore is the separation not chosen to be higher than 30 μm, because this can lead to even more mushroom kind of shapes with larger diameters. Figure 33c shows a higher magnification of the deposited metal layer. Finally, shows Figure 33d a top view of two chips SU8 structures with a metal layer. In this figure can be seen that during the deposition of the metal not only one dike was remained, but also for the other chip SU8 structures. Moreover, the width of the dike is measured to be 149 μm, which should be 108 μm. This larger width is again due to the fact that the distance between the mask and wafer during exposing was too high and/or development was too short.

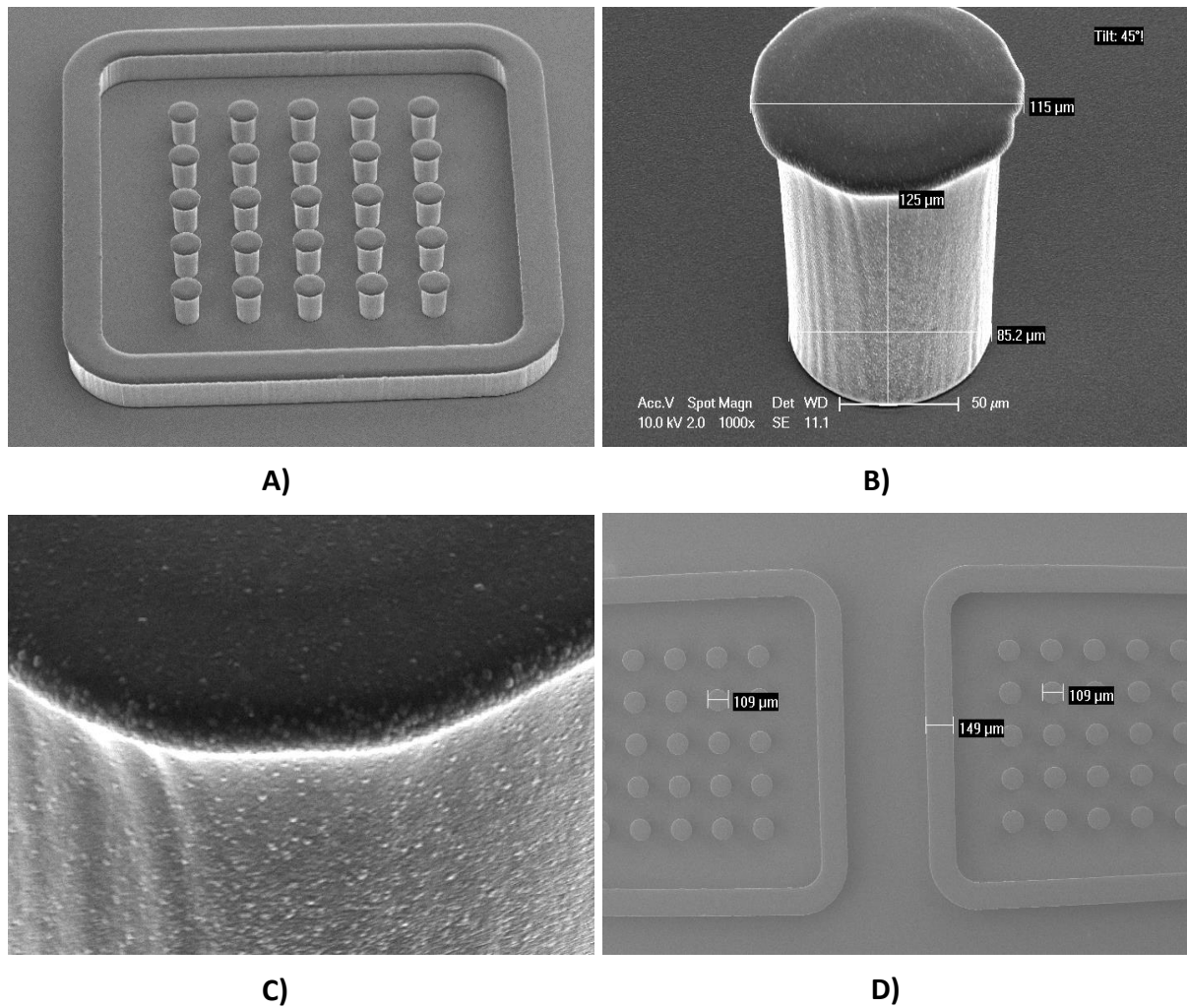


Figure 33: Tilt images from SU8 metallized pillars: a) Total overview of a single chip SU8 metallization, b) SU8 pillar metallization for single pillar with dimensions, c) High resolution metallization on top view of SU8, d) Top view two chip SU8 structures.

SU8 metallized pillars spray coating with AZ9260.

As earlier explained in the processing steps, is the following step to remove the metal between the pillars and the dike. To achieve this, a photoresist (AZ9260) layer is applied, exposed and developed. To inspect if the coating of the photoresist is applied homogenous, the coating step is imaged for the 1300 rpm spin coating of SU8, which is shown in Figure 34. Figure 34a shows the coating of the photoresist on the 5x5 pillar array. In this result is shown that the coating for the 5x5 array can be considered to be homogenous. No large accumulations can be seen on the top or bottom of the pillars, as would be expected. Looking to Figure 34b, a more precise representation of the coating for a single pillar can be seen. Here can be seen that the coating is less homogenous as expected in the 5x5 array image. For the single pillar, a wavier behaviour of the AZ9260 can be observed. A thicker layer of AZ9260 can be seen on the sides of the pillars and on the top. However, this is better than the expected homogenous distribution. A thicker layer of AZ9260 on the sides gives that a longer development and/or longer exposure is required to remove this. Nevertheless, removal of the AZ9260 on the pillars is undesirable. Therefore, using a short development will result in removal of the AZ9260 between the pillars, but not on the pillar sides.

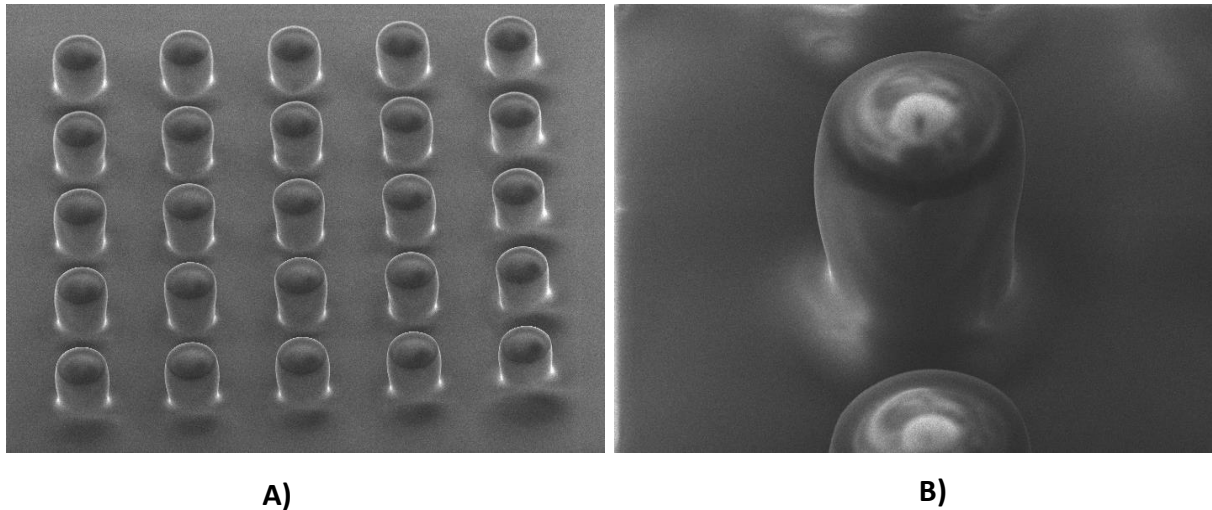


Figure 34: AZ9260 photoresist coverage of SU8 metallized pillars: a) Coating on the 5x5 pillar array, b) Coating on a single pillar.

Development of the AZ9260 on the 1100 rpm spin coated SU8.

An inspection is performed using the SEM_Philips_XL50, to ensure that the photoresist (AZ9260) is still present on the pillars after development. To ensure that less charging occurs, a lower electron acceleration voltage is used (approximately 1 kV). The resulting figures after the development can be seen in Figure 35. Figure 35a shows a single chip development. Here is shown that the AZ9260 is partly removed between the pillars. However, on the top right side is still some photoresist left, meaning that when etching the aluminium these top right patches will be connected to each other. When looking at a single pillar representation (Figure 35b) a more in-depth investigation can be found. To be expected is that the AZ9260 should still be around the SU8 metallized pillars, but this is not the case. Figure 35d shows a higher magnification SU8 pillar side. There could also be observed that besides the photoresist layer also the metal layer is visible. If wet etching is performed now, pin holes will occur in the SU8 metallized pillars which can degrade the performance of the patches.

A solution, to try covering up the SU8 metallized pillar with AZ9260, is to bake the developed wafer at a higher temperature than the curing temperature. When doing this, the AZ9260 applied layer is not dissolvable anymore in its development liquid.

So, by applying another AZ9260 layer on top of the old cured layer, which is not dissolvable anymore, another coating on the sides of the SU8 metallized pillars can be performed. Again, exposure and development can occur. This may result in a thicker layer of AZ9260 on the SU8 metallized pillars and therefore no pin holes will occur.

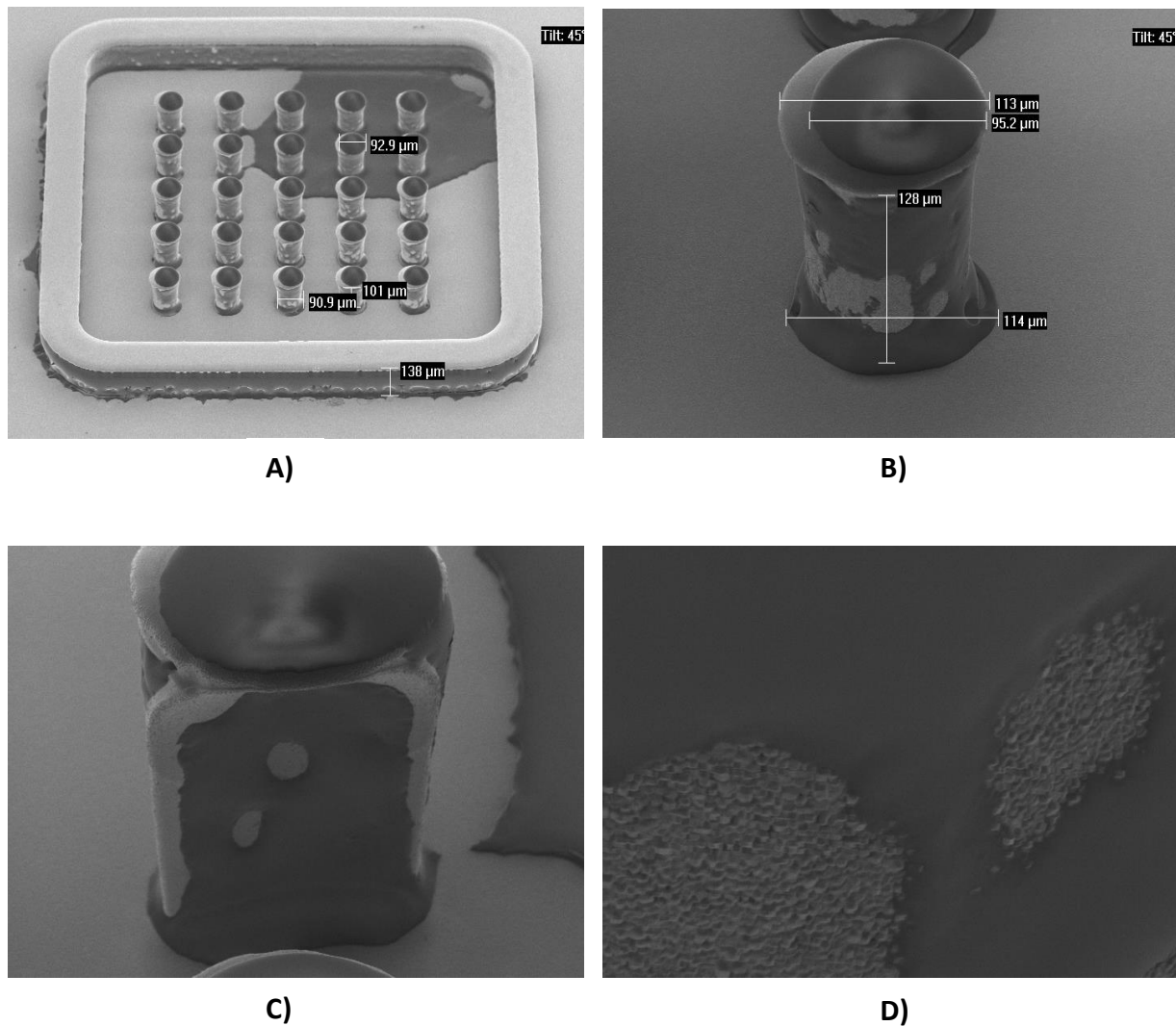
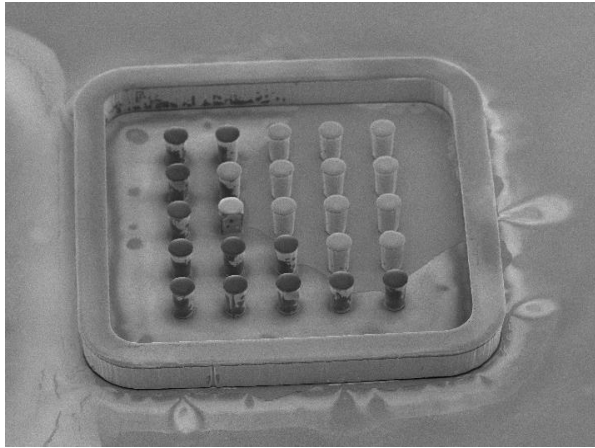


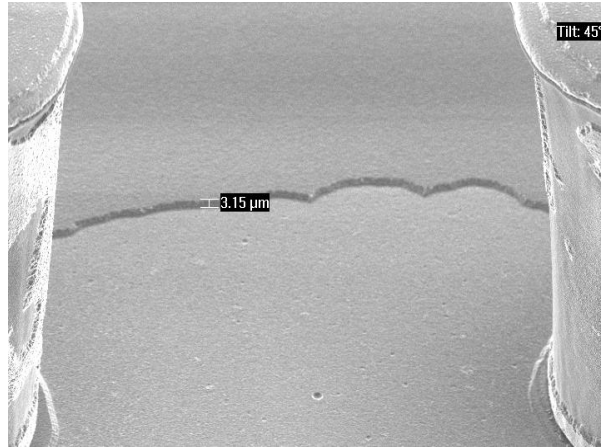
Figure 35: Tilt images from SU8 metalized pillars after AZ9260 development: a) Total overview of a single chip, b) For single pillar with dimensions, c) Single pillar view, d) High resolution development on pillar side.

Wet etching of Aluminium.

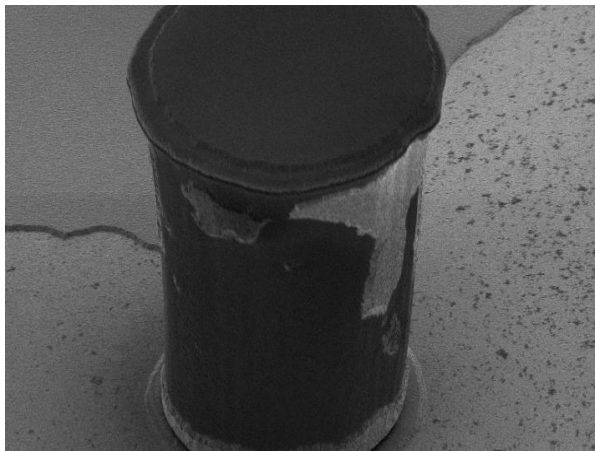
Wet etching of the 4 μm layer is performed on the wafer with SU8 pillars, which are created at a spin coating speed of 1100 rpm. As seen in Figure 35, pinholes can occur when performing wet etching. The number of pinholes and the wet etch time are investigated. The resulting SU8 metalized pillars after a wet etch time of 30 minutes (because 75 nm will be removed after 30 s) can be seen in Figure 36. Looking at Figure 36b shows that the wet etching, which is performed was too short. Only 3.15 μm is etched instead of the desired 4 μm . Therefore, the etching time should be increased for further processes. Figure 36c and d show a clear difference between etched aluminium and not etched on a single pillar. It can also be seen that when etching does occur for a removal of 4 μm , lots of aluminium will be lost on the pillar. This will result in degrading performance of the sensing pillars.



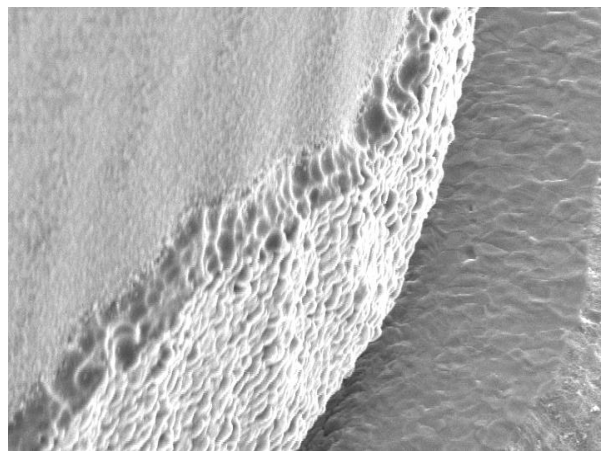
A)



B)



C)



D)

Figure 36: Tilt images from SU8 metalized pillars after wet etching aluminium; a) Total overview of a single chip, b) Height measurement of etched aluminium, c) Etching behavior on single pillar, d) High resolution of the aluminium on the bottom of the SU8 metalized pillar.

3.6.1.2 Wafers with cavities in SU8

The second process is for the creation of SU8 cavities. Here a flowchart process is followed by using a 1300 rpm SU8 spin coating and the second flowchart follows a 1000 rpm spin coating.

Creation of SU8 cavities for 1300 rpm spin coated SU8.

Figure 37a shows the created cavities in SU8. In this figure can be seen that the created diameter (which is from the mask design 110 μm) is not the same for each cavity. In Figure 37d is the cavity not the same height as should be annotated in Figure 37b. This is because of a longer exposure time and development is required. Enabling the development liquid to go into the cavities is more difficult than when creating pillars. Moreover, Figure 37b shows that no clear edge is obtained for the corner of the SU8 plateau. Longer development may solve this problem.

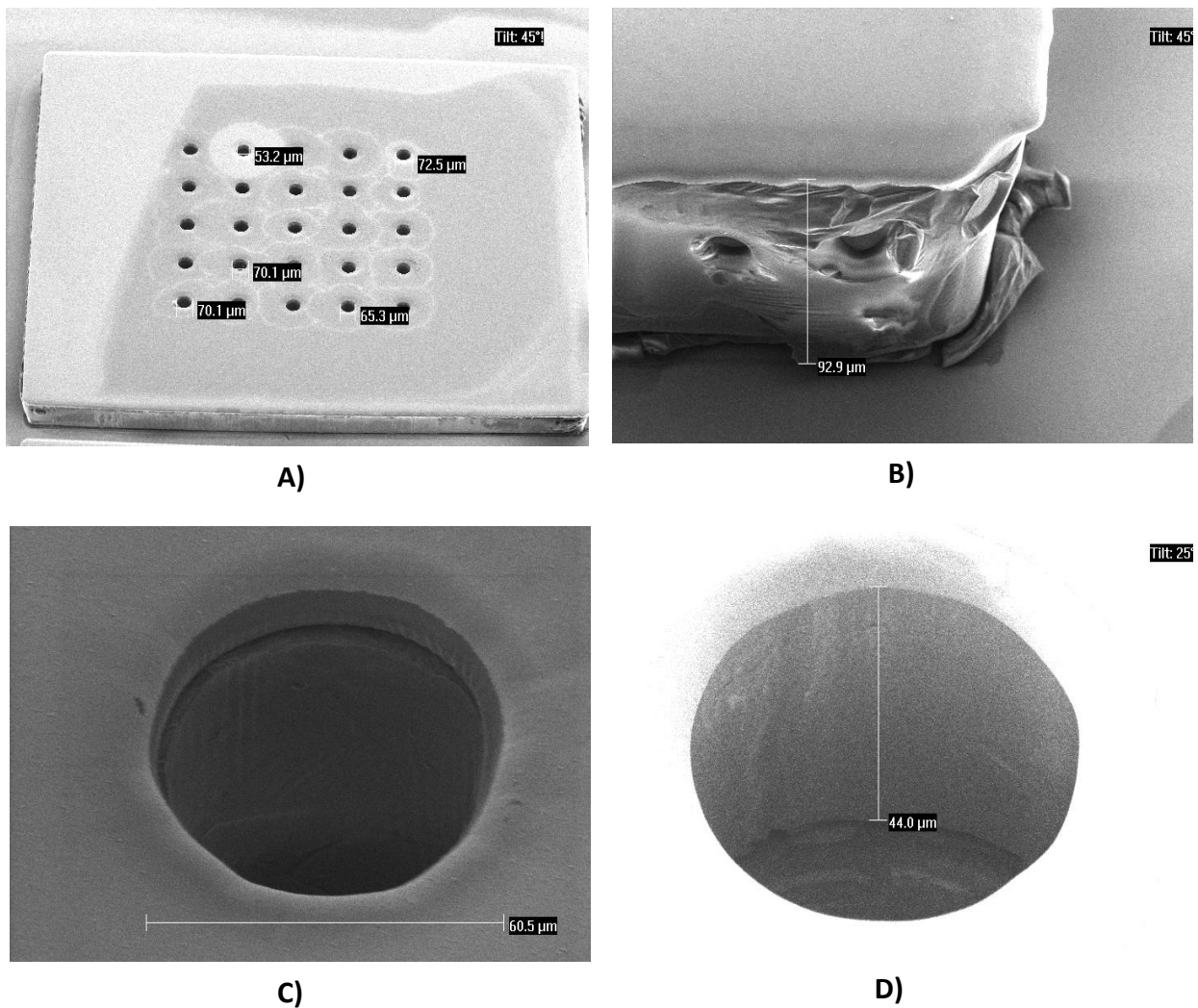


Figure 37: Tilt images for cavities in SU8: a) Total overview of a single chip, b) Corner image, c) Cavity in SU8, d) Cavity in SU8 depth measurement.

Appendix B.4.3 shows the creation of cavities in SU8 for a spin coating speed of 1000 rpm.

3.6.2 Final results with chip

After the dummy wafer processes a process can be started where the actual chip is attached on to the wafer. Hereby a 3x2 array is created on the carrier wafer. The wafers considered to be contaminated due to the Al + 0.5% CU in the metal of the patches. The attachment of the chip on the carrier wafer can be seen in Figure 38. This attachment ensures that during processes the chip cannot be detached from the wafer and that after fabrication the chip with the wafer has to be cut from the entire wafer.

The process steps regarding the creation of the SU8 layer is discussed. Since the old mask aligner (EVG420) is put out of order a training on the new contact aligner (SUSS). However, with this contact aligner it is not allowed to move each microscope individually. Therefore, I am bounded to the set distance given for the standard alignment markers on both sides of the wafer.

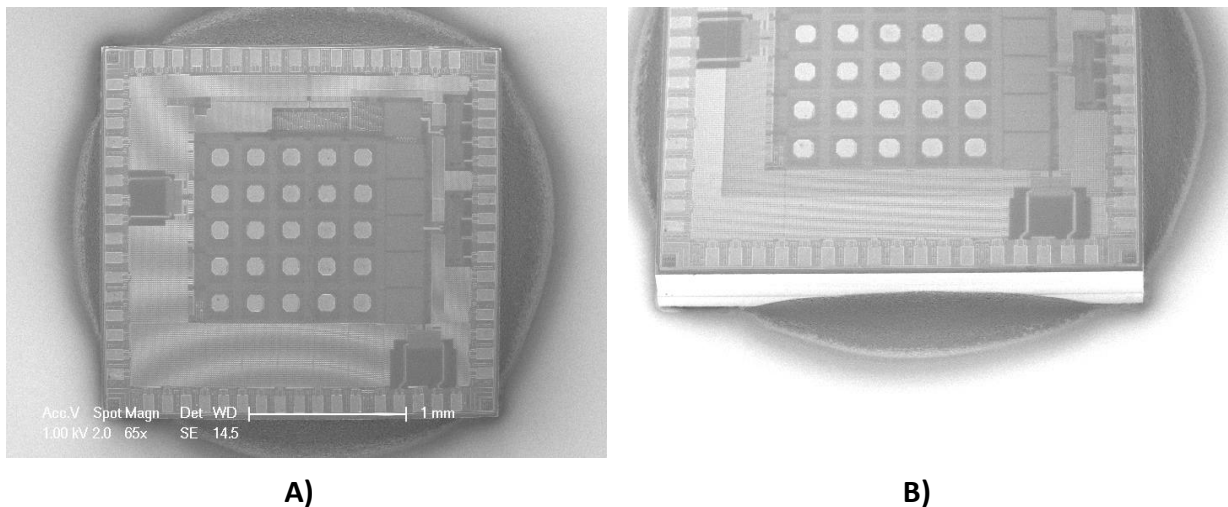


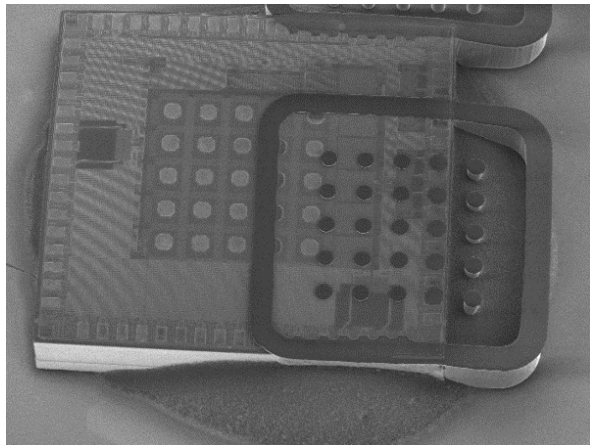
Figure 38: Chip overview of attachment to the carrier wafer: a) Top view, b) Side view.

3.6.2.1 SU8 pillars

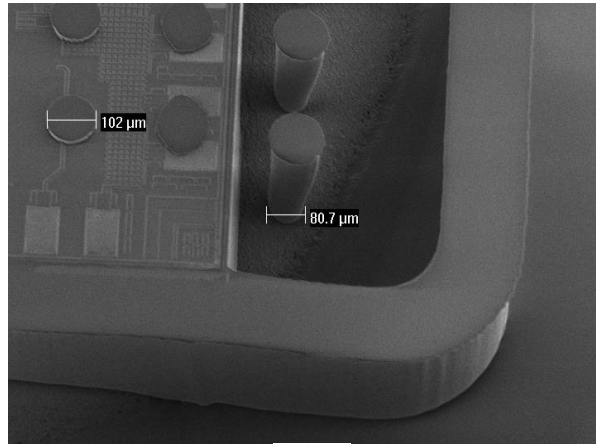
Figure 39 shows the created SU8 pillars on the CMOS permittivity chip. As described previously, a new machine is used to perform the alignment. This alignment for the left and right side of the wafer can be seen in Figure 39c and d. These show that the alignment is performed in the correct manner. However, the alignment of the pillars on the patches (see Figure 39a and b) is totally not accurate. Moreover, can be seen that the created height on the chip is not the 200 μm as should be expected for a spin coating speed of 800 rpm.

First, could the incorrect alignment of the patches and the pillars be caused by two main parameters. The first cause can be that the placement of the chip is not as expected for the created masks, or the mask design which is created, used the wrong assumption that were made during the design. However, as designed in the masks, there are two patches which will be sacrificed for the alignment. By moving the microscopes, alignment can be performed using the patches as alignment markers instead of the standard alignment markers given on the left and right side of the wafer. Nevertheless, as mentioned before is this not allowed in the new mask aligner and therefore the tool owner should be contacted to perform these alignments or a different machine should be used.

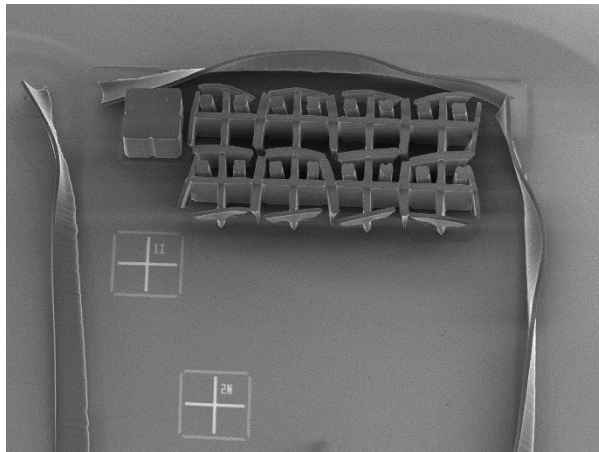
Secondly, could the flat creation of the SU8 pillars be a cause of the height difference on the wafer surface. However, this problem can be solved for further processes. To perform an equal SU8 layer to this chip, it is convenient to place structures around the chip that have the same height as the chip. This create a plateau and enables more accurate heights around the chips. Creation of this uniform plateau can be created by attachment of the residues that are located on the fabrication wafer of the chip.



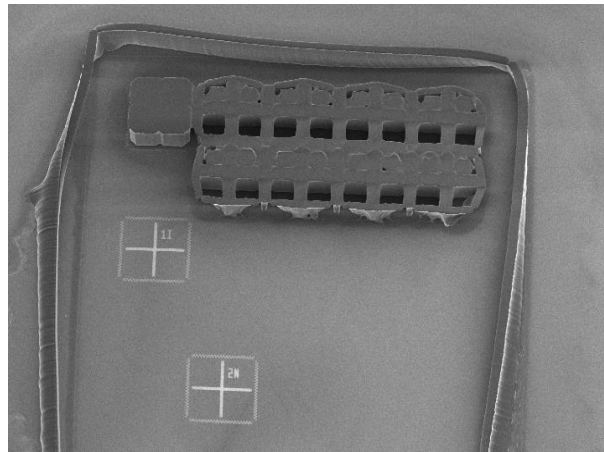
A)



B)



C)



D)

Figure 39: Tilt images from SU8 metalized pillars on the CMOS permittivity chip: a) Total overview of a single chip, b) Dimensions of the applied SU8 layer, c) Alignment on the left side of the wafer, d) Alignment on the right side of the wafer.

3.7 Conclusion

To conclude, different solutions should first be considered to create metalized pillars on the patches of the CMOS permittivity sensor. To enable the creation of the packaging solutions, the different steps are listed. With these processing steps a flowchart is designed and approved to allow processes in the cleanroom. However, to create these pillars and cavities different masks are designed and ordered as foil masks.

The first trials, which are done are from the dummy wafer results. From these results the following parameters are tested; the spin coating speed of SU8, exposure separation and dose, development time for both the SU8 and AZ9260 and the etch time for wet etching of aluminium. These results show that it is convenient to choose a spin coating speed of 800 rpm. For exposure of the wafer, three different contacts between the wafer and mask can be chosen. These are as follows; separation, soft contact or hard contact. During exposure a hard or soft contact resulting in fewer mushroom shapes for the SU8. Regarding the AZ9260 also here it is convenient to use soft or hard contact during exposure to create fewer mushroom shapes for the pillars. Moreover, when pinholes of AZ9260 are created on the pillars, during development, a second layer of AZ9260 can be applied.

Using the parameters, obtained from the dummy wafer processes it results in the creation of the SU8 pillars on the chip. However, the first iterations show that alignment is poorly using the new contact aligner machine and that creation of the SU8 height is not performed. To optimize further iterations a plateau should be created around the chip to enable better SU8 coating. Regarding the alignment moving the microscopes to be able to use the patch aligners is required. However, to accomplish this a different machine should be used or the tool owner needs to perform the alignment.

Furthermore, to prevent contamination of the tool, it is not allowed to perform an HSE step on the chip to remove the native oxide on the Al + 0.5% CU patches. This results in a bad or even no connection between the patches and the SU8 metalized pillars. To ensure this connection, a different approach should be performed, which should be examined in the following processes.

4. First level validation dielectric spectroscopy for hydration monitoring

To make sure that the Essence chip will also work with different skin permittivity a validation measurement is needed. Therefore, a system will be used, which acts in a similar method as the Essence chip. Here the use of a pin and patch method is used. The pin and patch can be seen as a single patch of the Essence patch array. To be able to detect the permittivity, different measurements and setups should be performed. These methods and setups will be discussed into more detail in this chapter.

4.1 System overview

To enable measurements of the skin permittivity with a pin and patch configuration, a code should be developed to describe the behaviour of the patch and to be able to perform measurements with this behavioural description. This code is implemented by Harshita Thippur Shivamurthy [72]. However, to enable measurements in a Matlab GUI interface, the code should be rewritten in a different manner. The new designed code will be discussed in the following section.

In addition to the creation of the new code, other steps required to enable skin permittivity measurements. The second step is to perform a calibration with known permittivity liquids. After calibration, the system can be evaluated regarding its performance by measuring independent known permittivity liquids. After validation of the known permittivity liquids, measurements for skin permittivity can occur.

The system setup also contains different connections, settings and interfaces which can influence the measurement and calibration performances. These influences can be seen in Figure 40. Each of these influences will be discussed and examined. These influences are examined in Appendix C.3

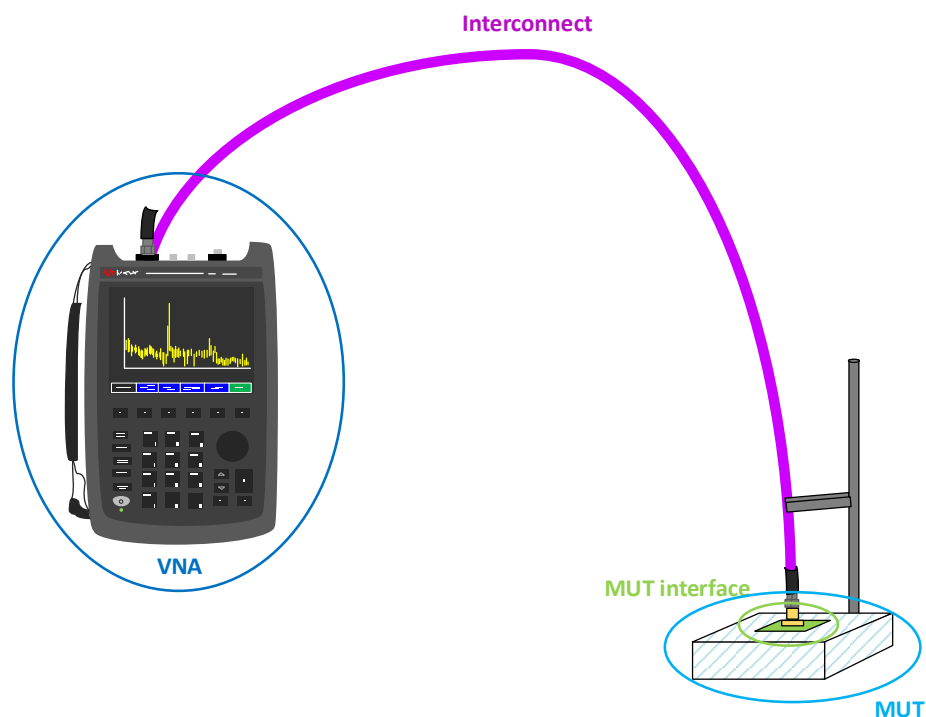


Figure 40: System overview with connections, settings and interfaces.

4.2 Matlab code to enable GUI interface measurements.

Two Matlab codes are created to enable GUI interface measurements. The first code is to create the known permittivity liquids with their according permittivity over a given frequency range. The second code is to generate a LUT, which will be used for performing measurements.

4.2.1 Matlab code for calibration liquids generation

As discussed in the previous section, a calibration is required to ensure the validation of the measurements. However, to perform this calibration three known permittivity liquids should be applied to the system. These liquids should give their known permittivity at certain frequencies points. Moreover, are the admittance, impedance and S11-parameter required.

With the use of the code from [72] calculation of the admittance, impedance and permittivity can be established. Generating of the S11-parameter can be performed and finally the resulting parameters can be saved in a structured manner to enable implementation in the GUI interface. The GUI interface, which will be used, is created and used by the company Vertigo Technologies. The resulting file can be found in Appendix C.1. Here each liquid is separately saved with its resulting parameters. A visual representation on how the generation of the calibration liquid, inhere methanol, is performed can be seen in Figure 41.

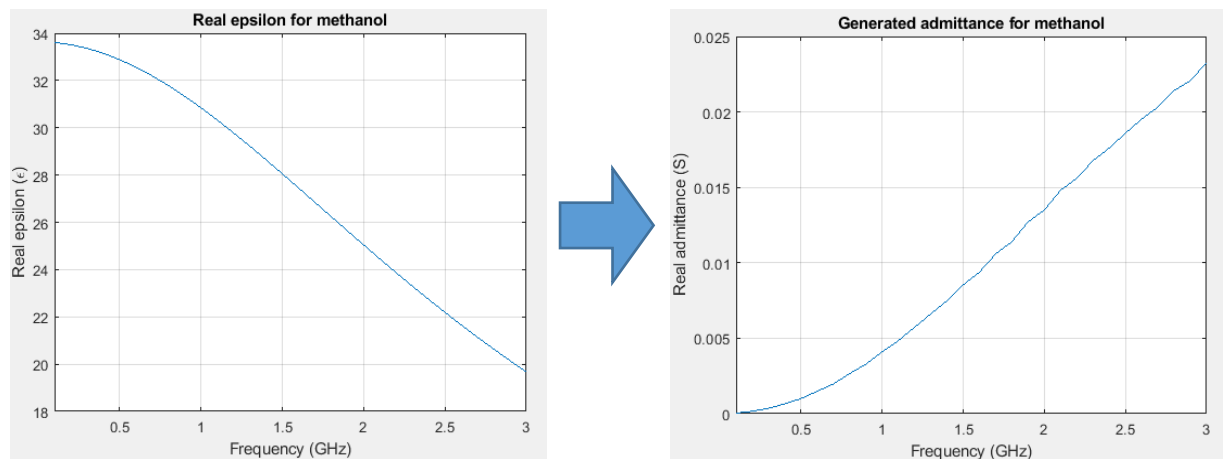


Figure 41: Creation of the real Admittance, from the real permittivity, for the calibration liquid methanol.

4.2.2 Matlab code for Look Up Table generation

For the calibration and the measurements a Look Up Table (LUT) is required. This LUT is generated as follows; first the frequency range should be defined. Then, a LUT with a certain array size should be defined. For instance when choosing a LUT with a size of 100x100 elements, it is possible to assign a real and imaginary permittivity range to this configuration. Therefore, choosing a real permittivity range from 1 to 81 with steps of the array size (100 points) gives a permittivity accuracy steps of $80/100=0.8$ epsilon. The resulting LUT will be a 3D array. Also, when defining the LUT table, it is possible to define the integration interval of the integrals, which will be used for calculating more precise permittivity's and admittance at different frequency points. The code to generate this LUT is given in Appendix C.2. A visual representations on how the generation of the real Admittance for the LUT works can be seen in Figure 42.

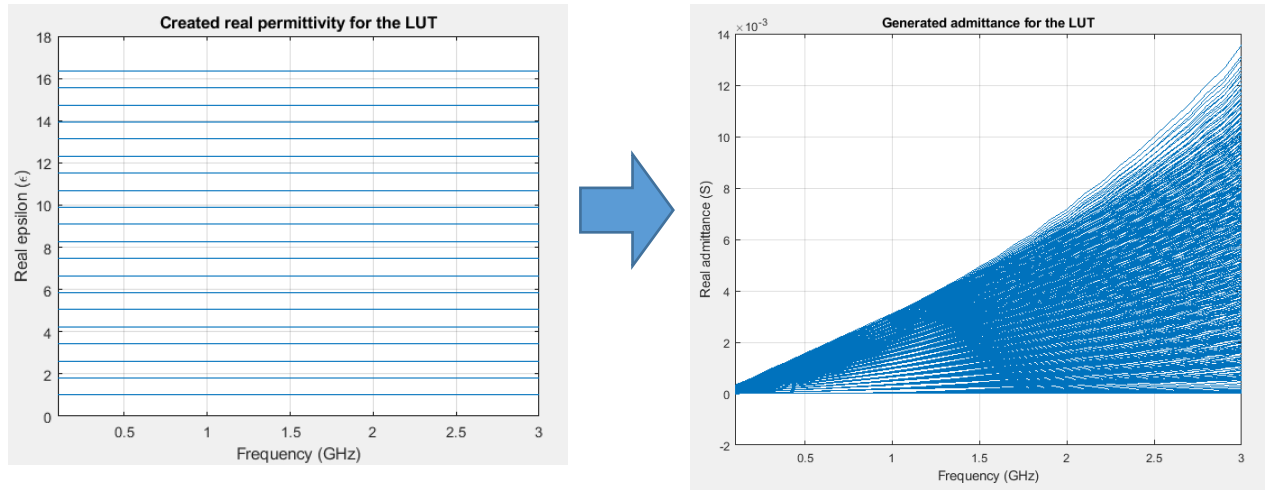


Figure 42: Creation of real Admittances, for a given real permittivity, for the LUT.

4.3 Calibration procedure

The measurement and calibration setup can be seen in Figure 43. In Figure 43 a calibration procedure is shown using for example, the three known permittivity liquids; butanol, ethanol and methanol. A Vector Network Analyser (VNA) also known as the Keysight microwave sensing device, is connected with a coaxial cable to a pin and patch with a SubMiniature version A (sma) connector. This pin and patch will be rinsed in a known permittivity liquid. And after each measurement, the liquid will be removed and the pin and patch will be dried using a tissue paper.

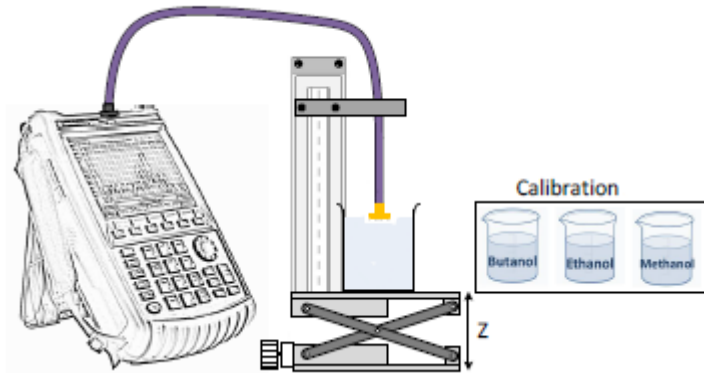


Figure 43: Measurement setup with pin and patch configuration.

4.3.1 Calibration setup

The calibration setup overview can be found in Figure 44. The calibration procedure works as follows. First, the pin and patch with the appropriate dimension should be chosen. Then, the frequency range with the frequency steps should be defined. After this setup of the calibration, it is possible to go from admittance to permittivity, by creating a Look Up Table or use an interpolated function. With the pin and patch measurements there is chosen to use the lookup table (LUT) configuration.

Thereafter, known liquids are placed on the patches with different radius. With these liquids, it is possible to find the admittance (Y) at different frequencies resulting in different permittivities. The admittance can be used to calculate the S_{11} -parameter. With the S_{11} -parameter the error terms can be calculated. These error terms remove the cable influence from the VNA to the Material Under Testing (MUT). Hence, now the measurements are actually performed on the MUT instead of the MUT with the coaxial cable connection.

An important notice is that the calibration should be performed by three known permittivity liquids and should be evaluated the entire measuring range. For instance, when the system is calibrated from the permittivity range of 1 to 20 epsilon and later a liquid is measured with a permittivity of 80, the system will not be able to map this value resulting in an invalid approximation permittivity. Also, here the same applies as when creating the LUT. Generating the permittivity for different frequency points is performed by solving integrals. The integral area can be changed to perform faster and less accurate measurements or slower and more precise measurements.

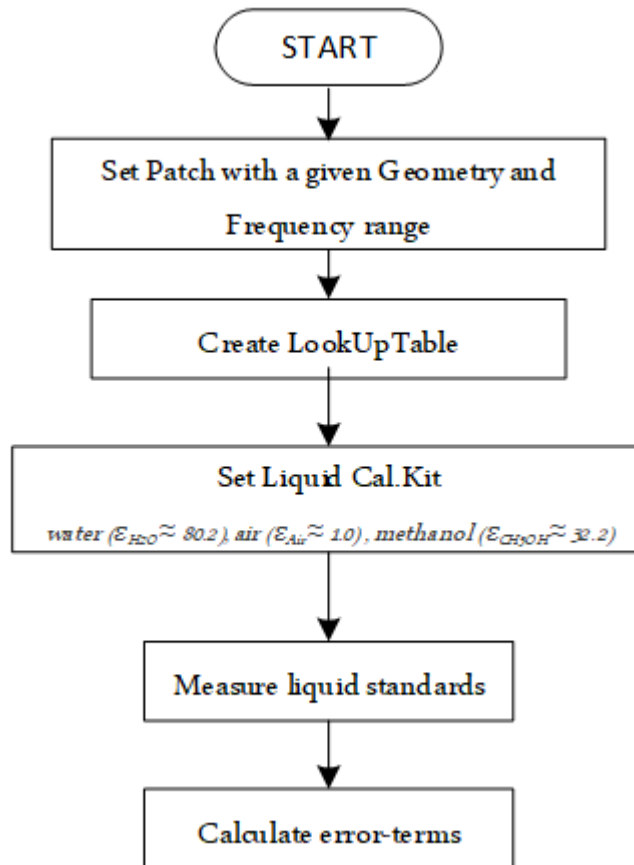


Figure 44: Calibration setup overview.

4.3.2 Patch geometry

The first given patches are created by Harshita Thippur Shivamurthy and has a square shape (see Figure 45f). However, to allow skin measurements, it is not allowed to perform measurements with a square shape, because this may inflict wounds on the skin. Therefore, new pin and patch are designed with a circular shape with different ground plane and patch radii. These circular patches top view can be seen in Figure 45.

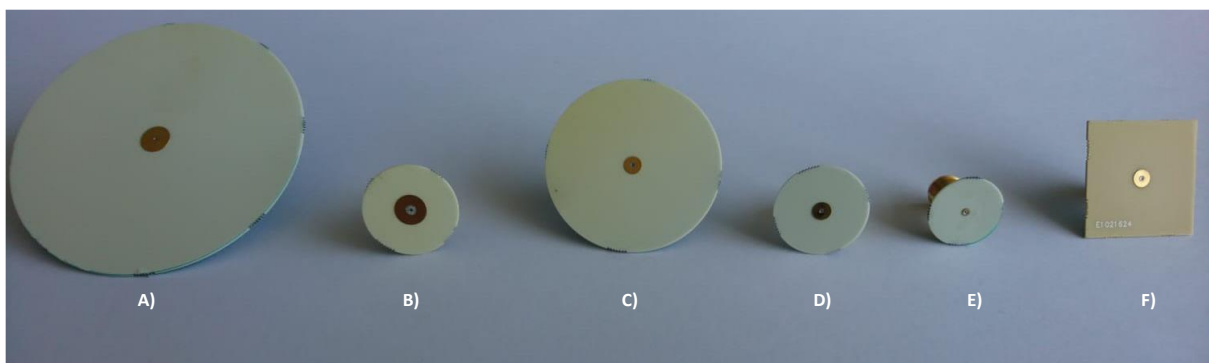


Figure 45: Top view for different geometry of the pin and patches.

The side view of the first patch and the designed circular patches can be found in Figure 46.

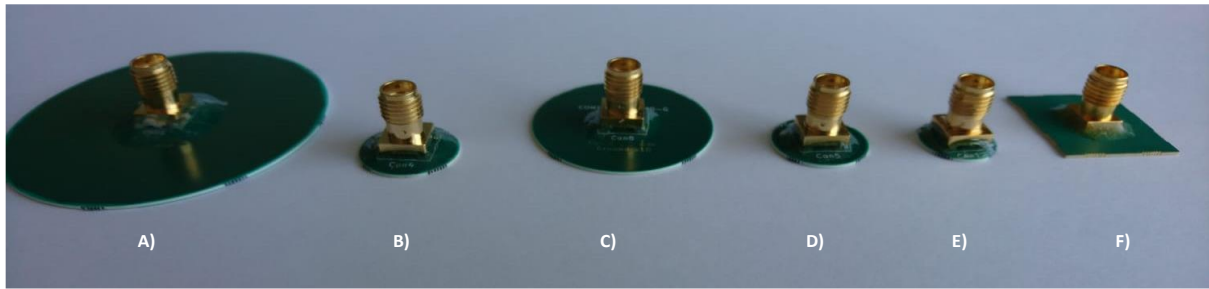


Figure 46: Side view for different geometry of the pin and patches.

4.3.3 Calibration results

When performing the calibration and collecting measurements results, it is possible to obtain the following graph (see Figure 47). Here are shown the input liquids; methanol and propanol used for the calibration (Cole-Cole model) and the measured results of these liquids. From these results, an accurate system where calibration can be obtained.

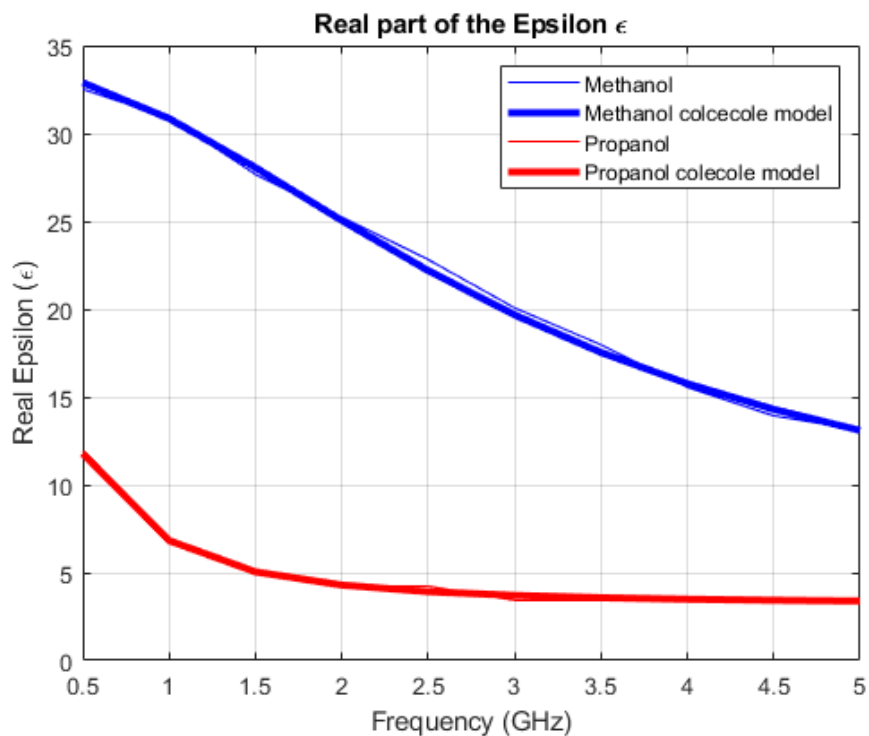


Figure 47: Calibration measurements.

4.4 Measurement setup

The total overview of how the measurement system works can be found in Figure 48. When performing a measurement, the calibration has already saved the error terms, which corresponds with the cable influence. These influences will be removed, which will generate the Γ_{raw} to the Γ_{meas} . Then, for each frequency point the measured gamma will be converted to an admittance that will be linked to the permittivity corresponding to this admittance and patch dimensions. The decision of choosing the right admittance is made by taking the minimum value of the Y_{measured} with the Y_{LUT} . This provides a real and complex permittivity and gives this as an output value. The data received from the measurement will be given in a structured manner, with S11-parameter, admittance and epsilon.

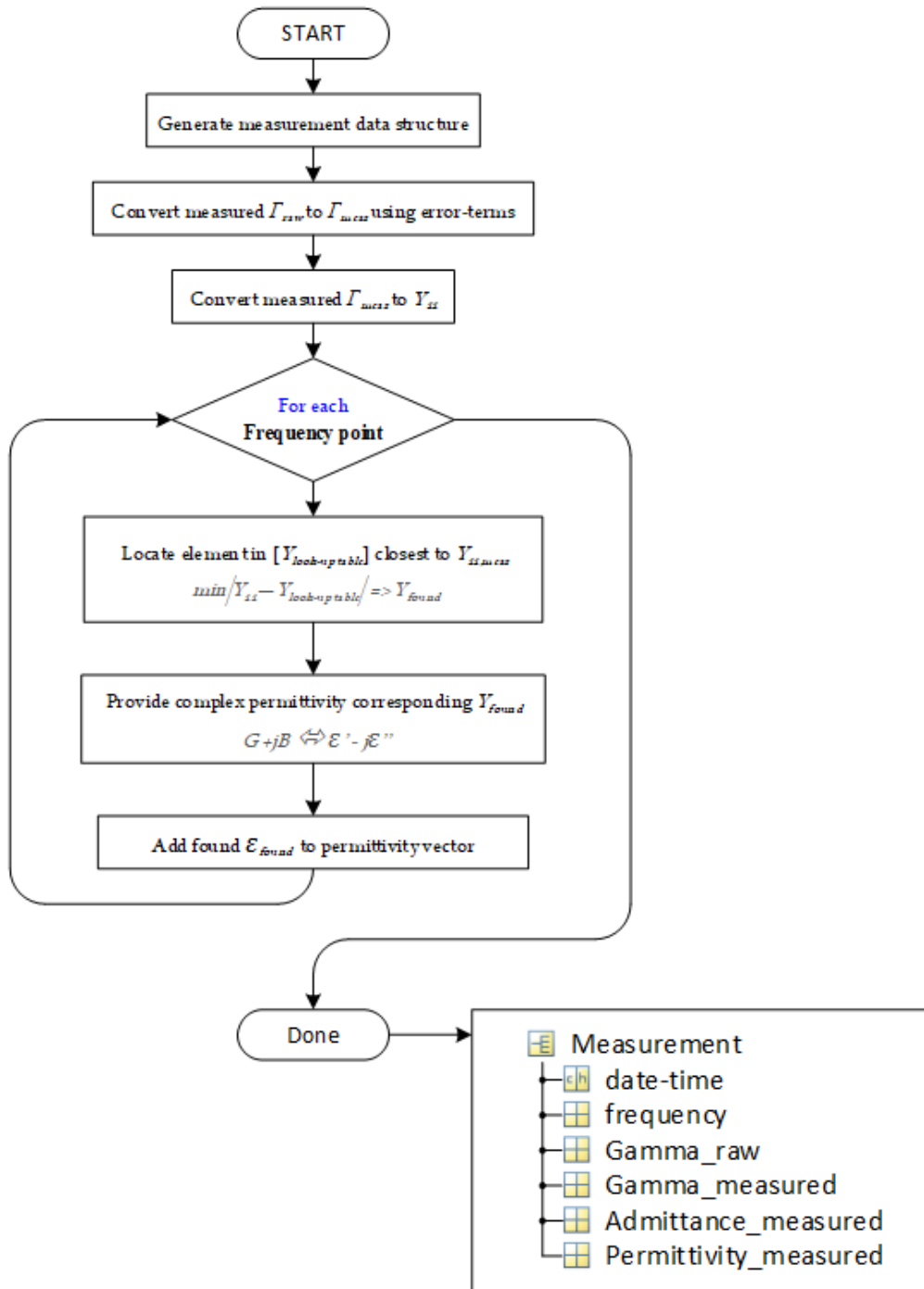


Figure 48: Measurement overview

The implementation of this algorithm is used in a GUI-interface in the program Matlab. This interface can be seen in Figure 49. First, the connection between the VNA and computer is established. This can be achieved by writing the IP address of the VNA to the GUI interface. After the connection between the VNA and the GUI interface is established, a frequency configuration should take place. Here, it is possible to choose between a single frequency or a frequency sweep measurement. Thereafter should be defined how the calibration will occur. For instance choosing the Liquid cal means that the calibration procedure will occur with liquids that have a defined permittivity for a given frequency range. After all these calibration setup steps, the calibration can be established. There should be three liquids chosen, which can be used for the calibration. After the Configuration of the calibration liquids and the measurements, measurement of different permittivities can be performed. For the measurement setup, it is possible to define the number of measurements for each liquid or point of skin and how many measurements you want to perform for this liquid or skin point. A measurement

will be performed in around one second. The resulting figures that will be shown, are the real and imaginary permittivity. When saving these measurements, the S11-parameter, admittance (Y) and permittivity will be saved.

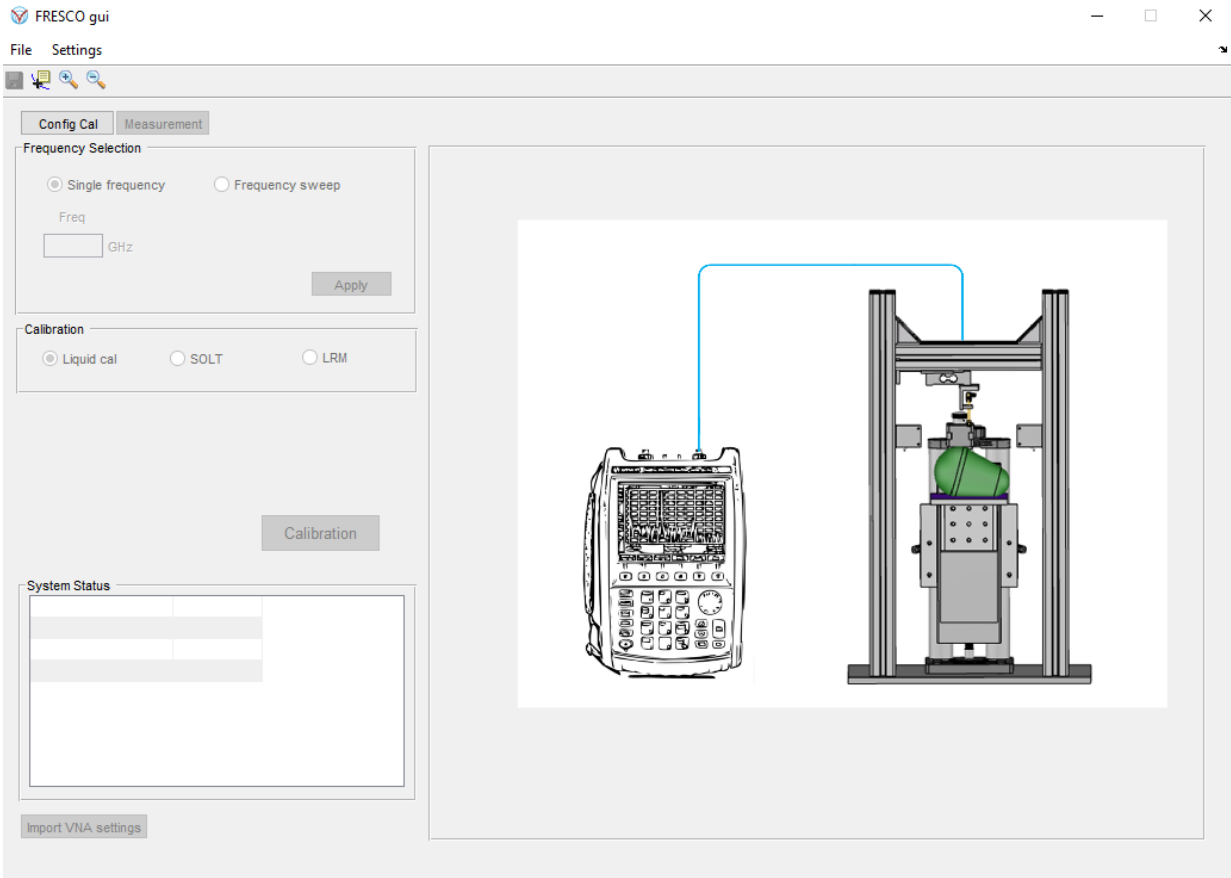


Figure 49: GUI interface for validation measurements.

4.5 Measurement result

From the calibration setup procedure, it was possible to change the following parameters;

- Integration Interval
- Size of the LUT (and thus the accuracy of the epsilon steps)
- Frequency range
- Epsilon real range
- Epsilon imaginary range
- Pin and patch dimensions
- Liquids used for the calibration
- Measurement liquids

With all of these variables, it is possible to have different measurements with different variables. These different measurements will be discussed regarding their outcomes and founding. Other parameters, which may influence the measurements results, are the cable distortion. For instance, moving or bending the cable can change the measurements in a wrong way. Another parameter that could influence the measurements results is the depth of the pin and patch in the liquids. These parameters will also be considered when performing the measurements. These influences are given in Appendix C.3.

4.6 Measurements results new liquids

Looking at the results from the previous measurements can be observed that there are several measurement errors while calibrating and measuring the liquids. This was due to the fact that the liquids are impure and/or the calibration setup is not performed in the right manner. To ensure that the impurity of the liquids does not influence with the calibration and measurements results, there is chosen to order new liquids and perform the calibration and measurement with these liquids. First, the liquid measurements will be discussed and secondly the skin measurements will be discussed.

4.6.1 Liquid measurements

For the new liquid measurements, the following variables hold;

- Frequency range is from 0.1 GHz till 3 GHz with 30 steps.
- IF bandwidth is 10 Hz.
- Output power is -10 dBm.
- Measurement is performed with deionized water.
- Integration interval is 1000 for generation LUT.
- Integration interval is 15000 for generation calibration liquids
- Calibration liquids are: water, methanol and propanol.

First, the calibration procedure will be examined. The S11-parameter results can be found in Figure 50. Looking at the zoomed version, one can see that the calibration for methanol and propanol is perfectly overlapping. However, the calibration measurement for water shows a different calibration. Here a lot of large translations occur when going to higher frequencies, resulting in more losses in the measurement.

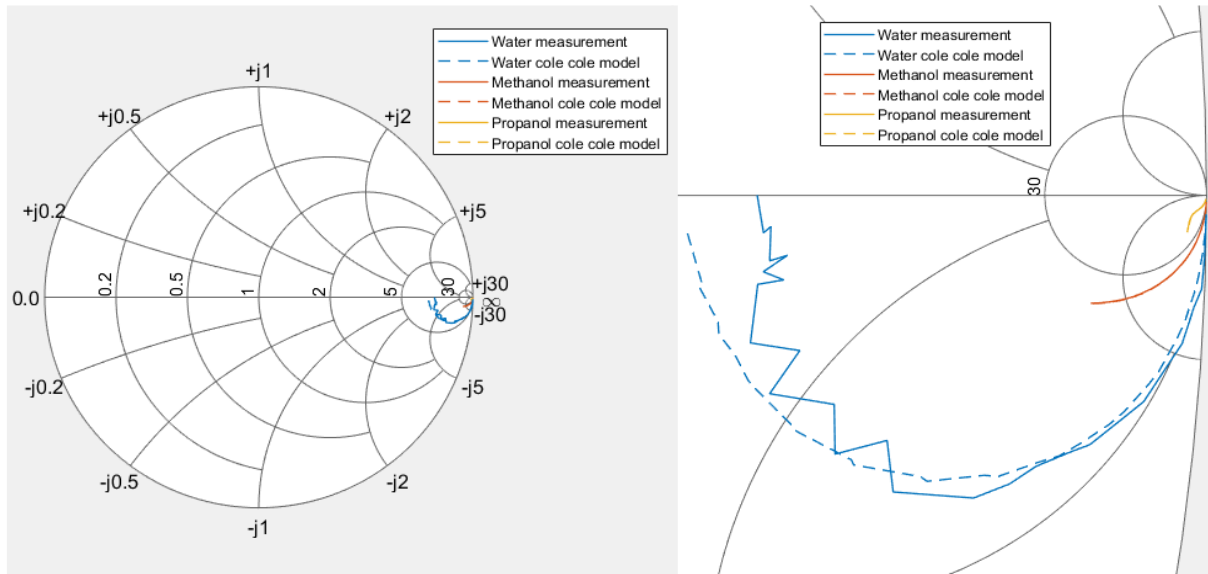


Figure 50: S11-parameter for calibration measurements a) overview b) zoom version

When converting these S11-parameters to epsilon, by using the LUT the real and imaginary epsilon for the calibration liquids can be obtained, see Figure 51. From these results the calibration liquids; methanol and propanol are clearly calibrated in the correct way. However, as expected from the S11 measurements, a high variation in the imaginary epsilon measurement can be detected. This can be a results of the liquid depth measurement and/or temperature and humidity in the measurement room and/or unstable connector. This effect is clearly visible for water. However, water can degraded fast in impurity, resulting in more oscillations for the imaginary measurements.

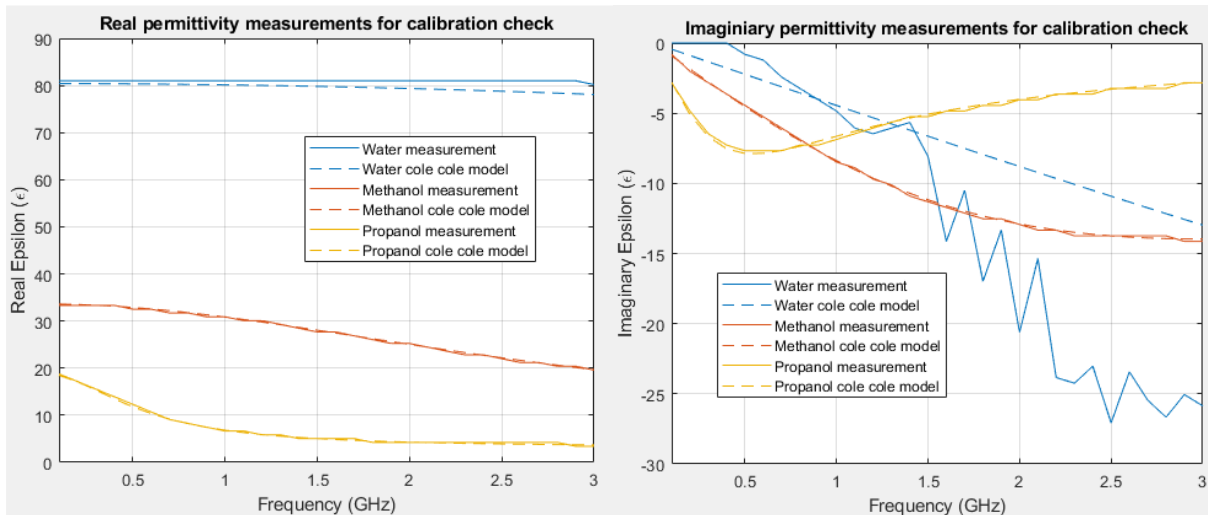


Figure 51: Permittivity measurements for calibration check.

To ensure the system works in a properly, independent liquid measurement is required. For this measurement is chosen to measure; air, butanol and ethanol. The zoomed version of the S11-measurement can be seen in Figure 52. Here can be noted that the measurements of butanol is closely to the predicted S11-parameter of the Cole-Cole model. Furthermore, shows the air measurement oscillations, which can also be an indication of bad connection and/or interconnection flaws. Looking at the ethanol measurements, results in an offset in the amplitude measurements.

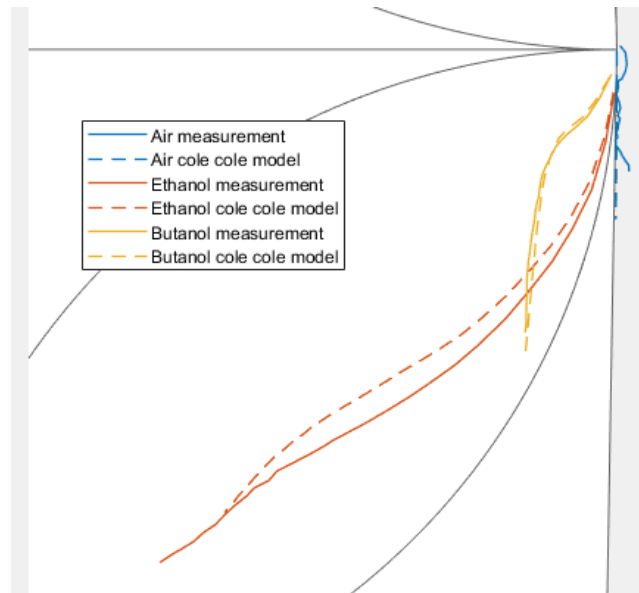


Figure 52: Zoom version of S11-parameter measurements for the independent liquids and air.

The resulting permittivity measurements can be seen in Figure 53. From these results, the amplitude offset can be seen for ethanol and the almost perfect measurement for butanol. Also, the measurements for air are the same as the expected Cole-Cole model, this due to the fact that the measurements from the S11-parameter results in a negative real permittivity. Nevertheless, this is impossible, since the LUT is only created for positive real permittivities, so the air measurement is showing the first available solution of one epsilon for the real permittivity and zero for the imaginary.

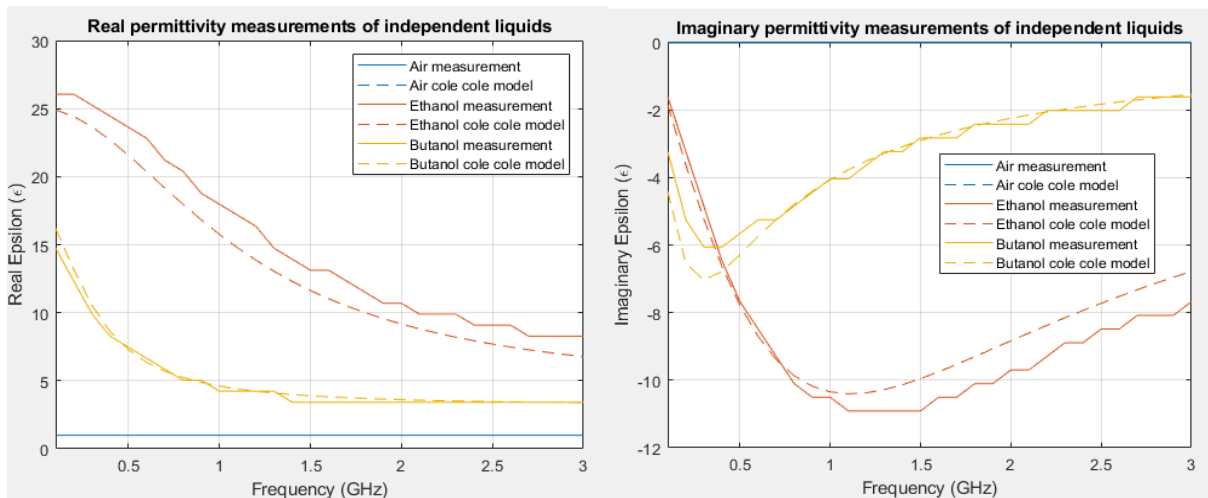


Figure 53: Permittivity measurements for the independent liquids and air.

The independent measurement results show enough promising results, even though the results are not exactly the same as the expected Cole-Cole model. Nevertheless, for the skin measurements we are looking at the delta epsilon difference between a hydrated skin and normal hydration level. Therefore, this system can be used for performing skin measurements.

4.6.2 Skin measurements

For the skin measurements the same setup and calibration is performed as described in section 4.6.1. To be able to detect the hydration level difference in the skin, the following setup measurement is used; first a zero-state measurement is performed. First, the hand is cleaned and dried. Then, a measurement is performed, which can be seen in Figure 54a. Here the skin permittivity is assumed to be in normal state and any contamination due to impure hands is removed. After finishing the zero state measurements, the hand is left in a beaker with water to enable absorption of water in the epidermis, see Figure 54b. The resulting hydration of the hand after 10 minutes of water absorption

can be seen in Figure 54c. This measurement was carried out by three different persons to ensure that a hydration difference between each person can be detected.

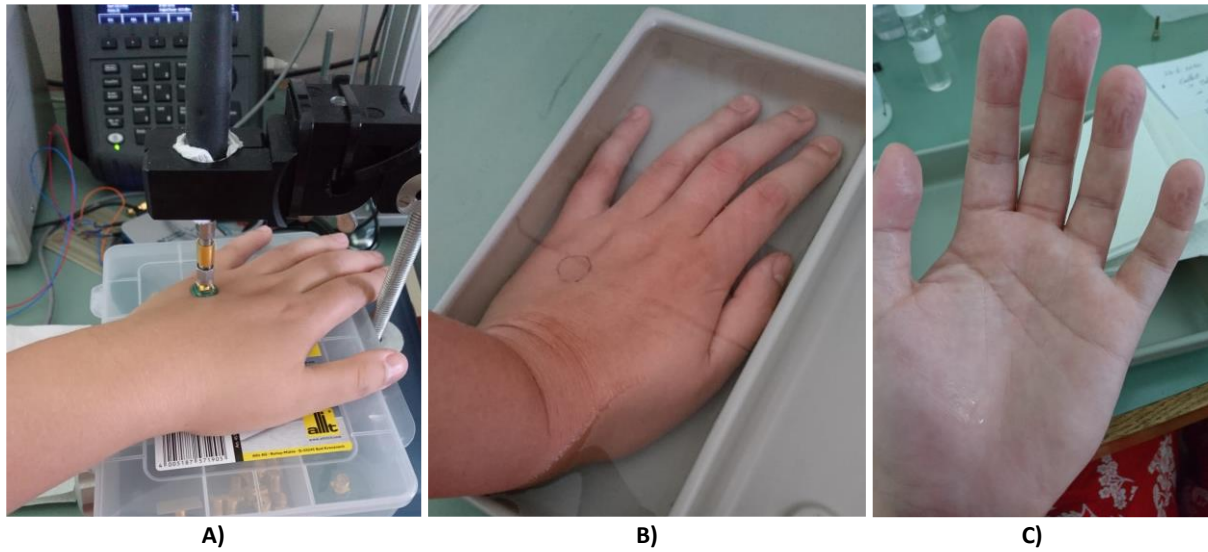


Figure 54: a) Zero-state measurement b) Putting the hand in water for 10 minutes c) Resulting hand hydration after 10 minutes of water.

First, zero-state measurement of each test person will be discussed. For the zero state measurements, five series of measurements are performed, this to average the results and thereby reducing the error.

4.6.2.1 Zero-state skin measurements

Converting the obtained S11-parameter measurements to permittivity results in a real and imaginary permittivity. The resulting real permittivity measurements can be seen in Figure 55. For the five serial measurements of each test person, a small deviation between each measurement can be observed. This due to the fact that a relaxing hand will never be relaxing in the same state. For instance, blood vessels pump the blood around in the hand and muscles can contract for a small portion when performing a measurement on the skin. While comparing the average zero-state skin measurement of each test person, a difference can be seen between the test persons. This is mainly due to different composition of nutrients, liquids and skin type (dry, grease etc.) in each of the persons.

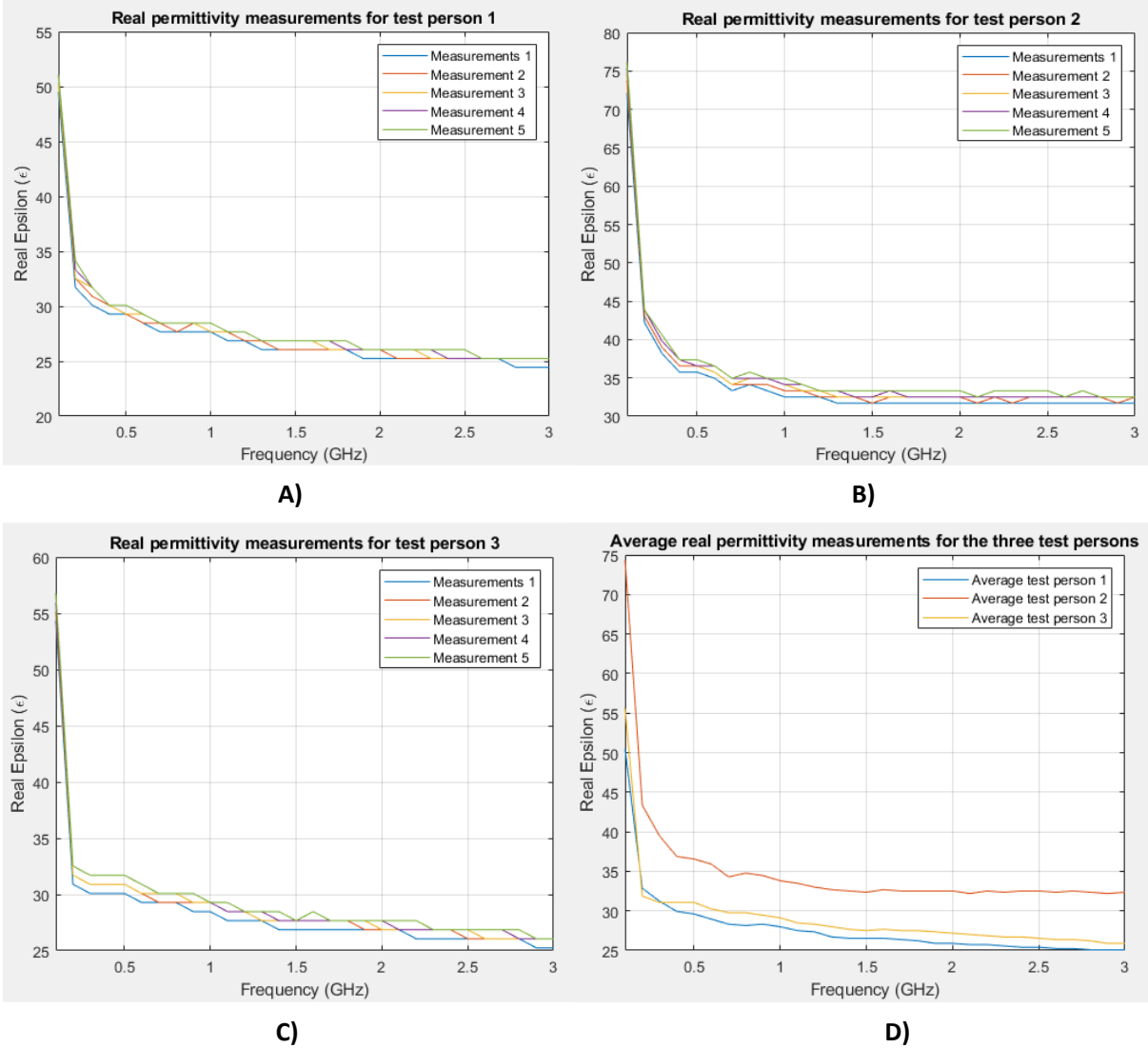


Figure 55: Real permittivity zero state skin measurements: a) test person 1 b) test person 2 c) test person 3 d) average of each test person compared to each other.

After looking at the real permittivity we can look at the according imaginary permittivity measurements, see Figure 56. Here the, same statements applies as for the real permittivity measurements.

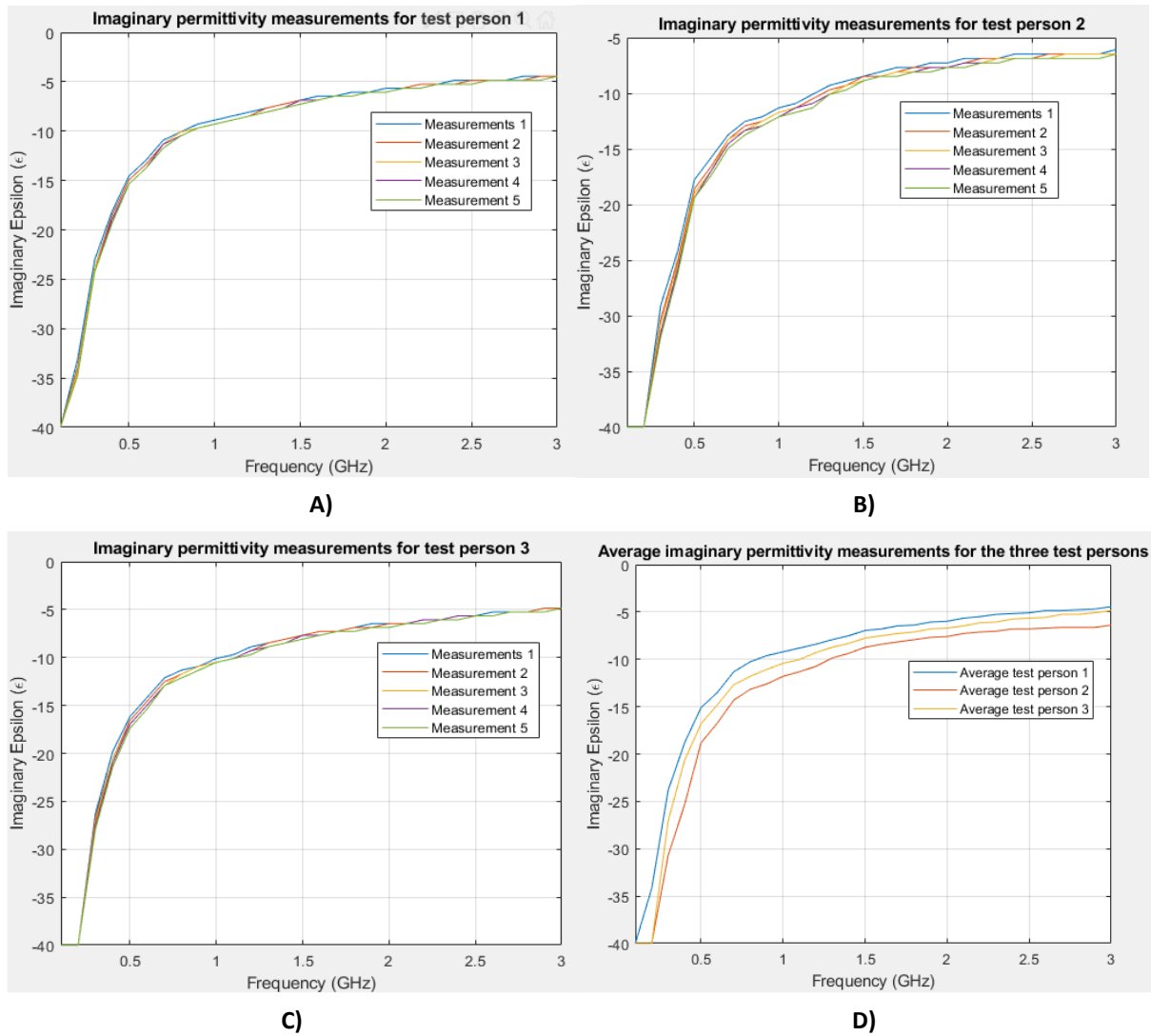


Figure 56: Imaginary permittivity zero-state skin measurements; a) test person 1 b) test person 2 c) test person 3 d) average of each test person compared to each other.

4.6.2.2 Hydrated-state skin measurements

Using the LUT to find the according epsilon results in the real permittivity measurements as given in Figure 57. Comparison of the skin measurements results for the hydrated-case with the zero-state case, results in the same conclusions as given for the zero-state skin measurements. Both curves should be plotted together, for more insight between the difference of the zero state measurements and hydrated skin measurements. After examination of the imaginary permittivity of each test person, this difference will be highlighted.

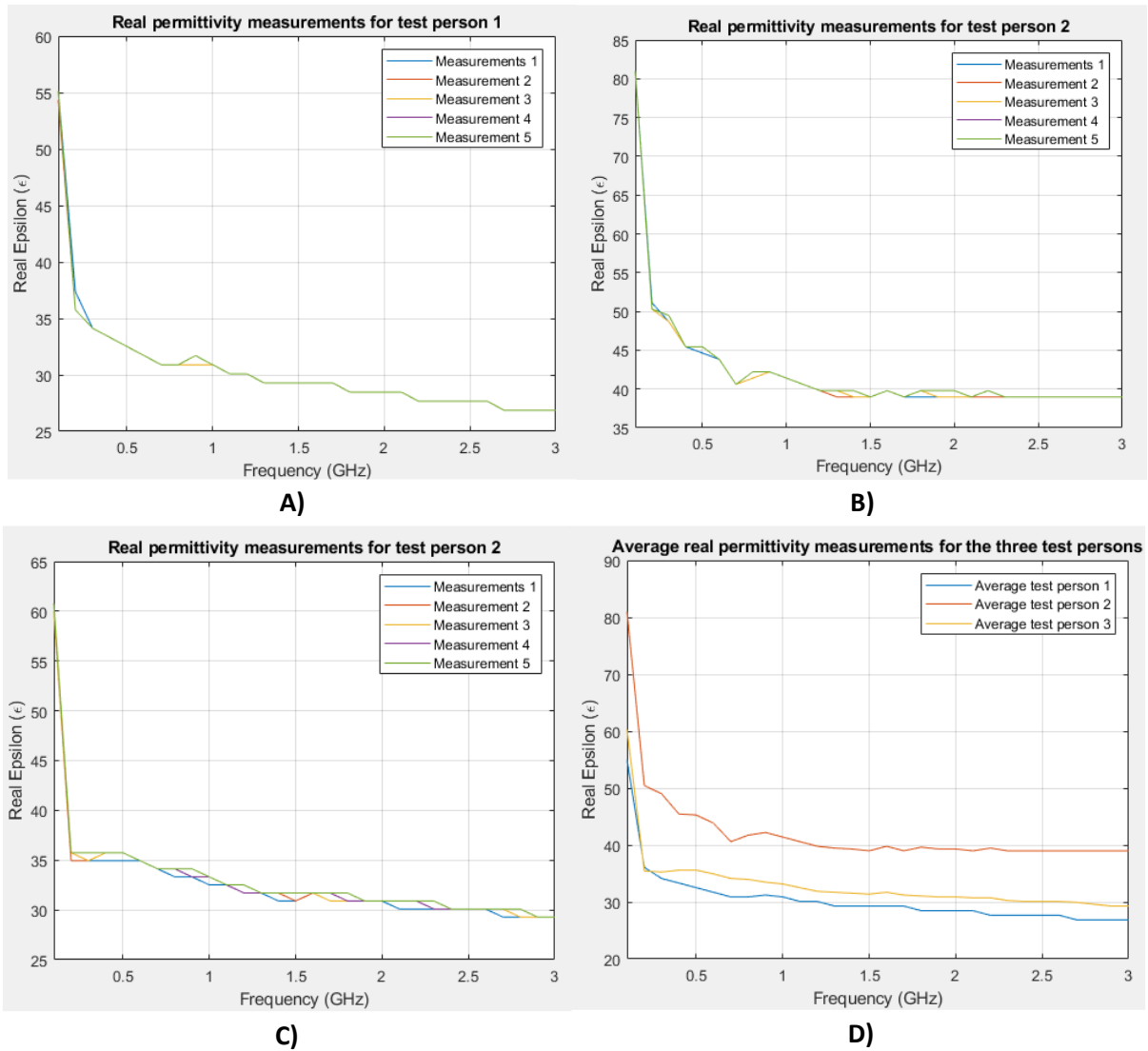
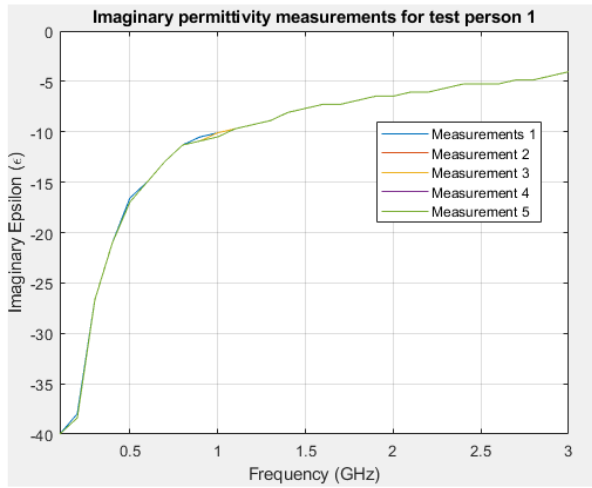
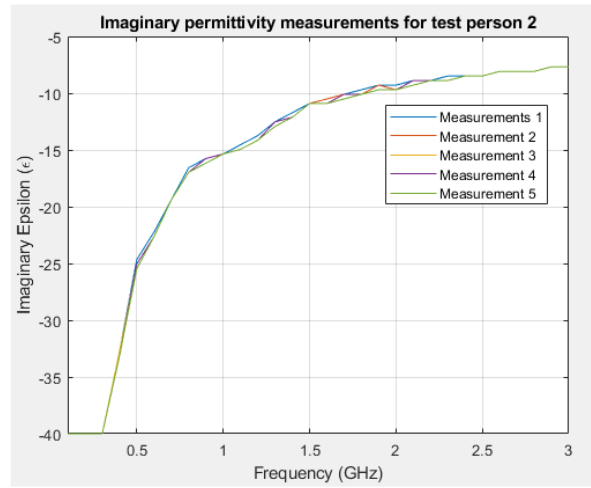


Figure 57: Real permittivity hydrated-state skin measurements; a) test person 1 b) test person 2 c) test person 3 d) average of each test person compared to each other.

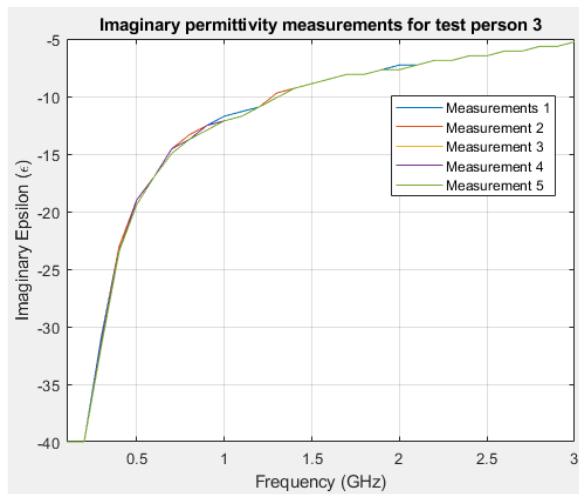
For the imaginary permittivity measurements in the hydrated case, the following obtained figures can be seen in Figure 58. The same conclusion applies for the hydrated imaginary permittivity as for the zero-state imaginary permittivity measurements.



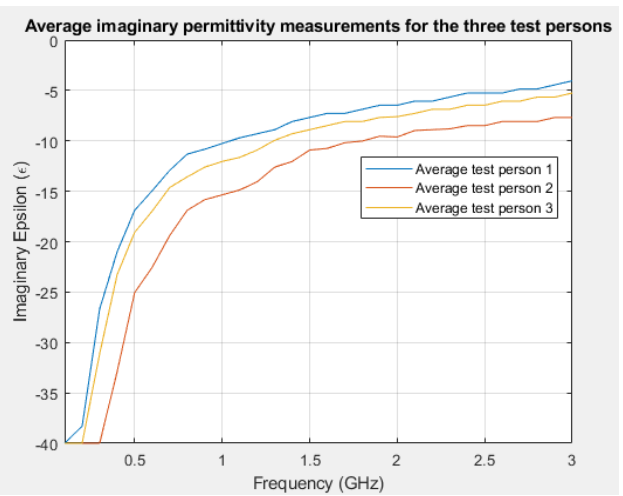
A)



B)



C)



D)

Figure 58: Imaginary permittivity hydrated-state skin measurements; a) test person 1 b) test person 2 c) test person 3 d) average of each test person compared to each other.

4.6.2.3 Comparison zero-state and hydrated-state

The obtained real permittivity of each test person can be seen in Figure 59. From these results a clear difference between the zero-state for each test person can be observed. For test person 1, the maximum real permittivity value between the zero-state and hydrated-state is 4.52ϵ and the minimum difference is 1.62ϵ . For test person 2, the maximum real permittivity value between the zero-state and hydrated-state is 9.54ϵ and the minimum difference is 6.30ϵ . Finally, for the third test person the maximum real $\Delta\epsilon = 4.6869$ and the minimum real $\Delta\epsilon = 3.39$.

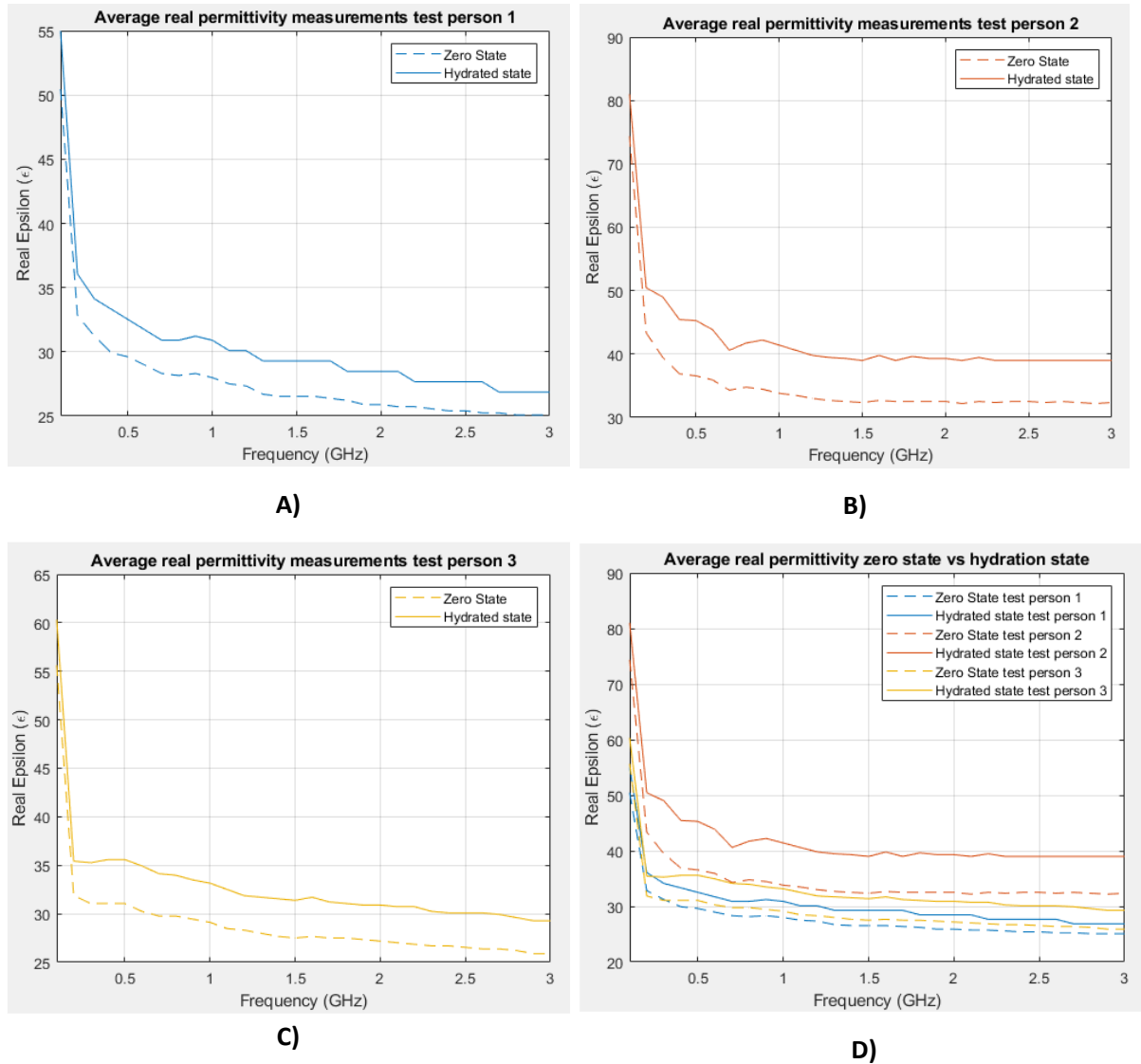


Figure 59: Real permittivity zero-state versus hydrated-state measurements; a) test person 1 b) test person 2 c) test person 3 d) test person comparison.

The resulting imaginary permittivity measurements for each test person is depicted in Figure 60. Also, for the imaginary permittivity measurements a clear difference between each test person is present between the zero- and hydration-state. For the first test person the maximum imaginary permittivity difference between the zero- and hydrated-state measurement is $\Delta\epsilon = 4.12i$ and the minimum imaginary permittivity $\Delta\epsilon = 0.40i$. The second test person has a maximum imaginary permittivity difference of $\Delta\epsilon = 9.29i$ and a minimum value of $\Delta\epsilon = 0i$. Finally, for the third test person the maximum imaginary $\Delta\epsilon = 4.04i$ and the minimum imaginary $\Delta\epsilon = 0i$.

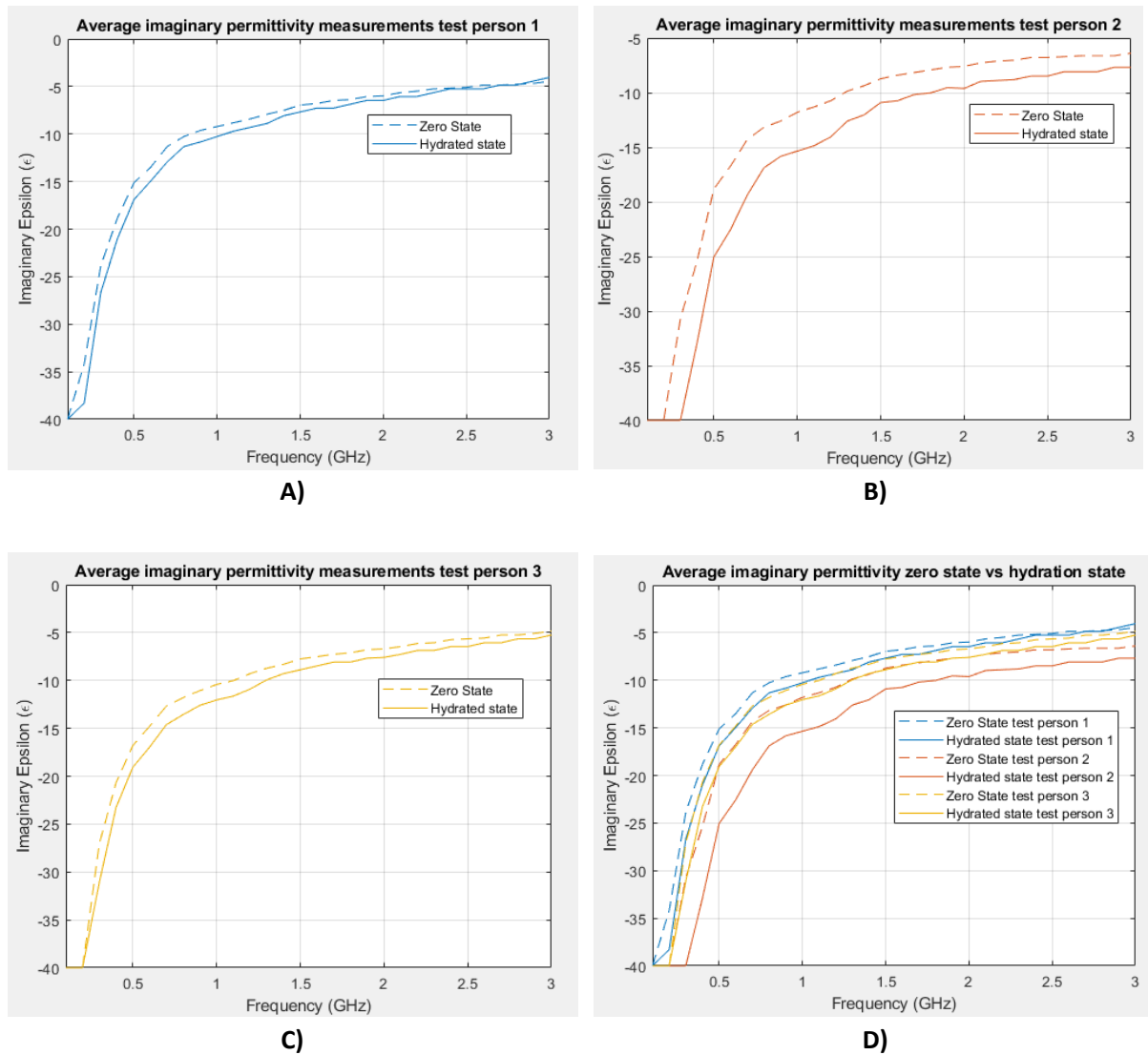


Figure 60: Imaginary permittivity zero state vs hydrated state measurements a) test person 1 b) test person 2 c) test person 3 d) test person comparison.

The difference between each person for the zero-state and hydrated-state regarding the average complex permittivity can be seen in Figure 61. Here the presented graphs show the absolute value of the hydrated-state regarding the zero-state. From Figure 61 it can be seen that difference is detectable between the hydration level of each test person. To conclude, from each individual the same behavior for the zero-state and hydration-state can be observed. When the skin becomes more hydrated a higher real permittivity difference can be detected. This could assume that when the skin becomes more hydrated the real permittivity measurement also becomes higher, independent of its zero-state.

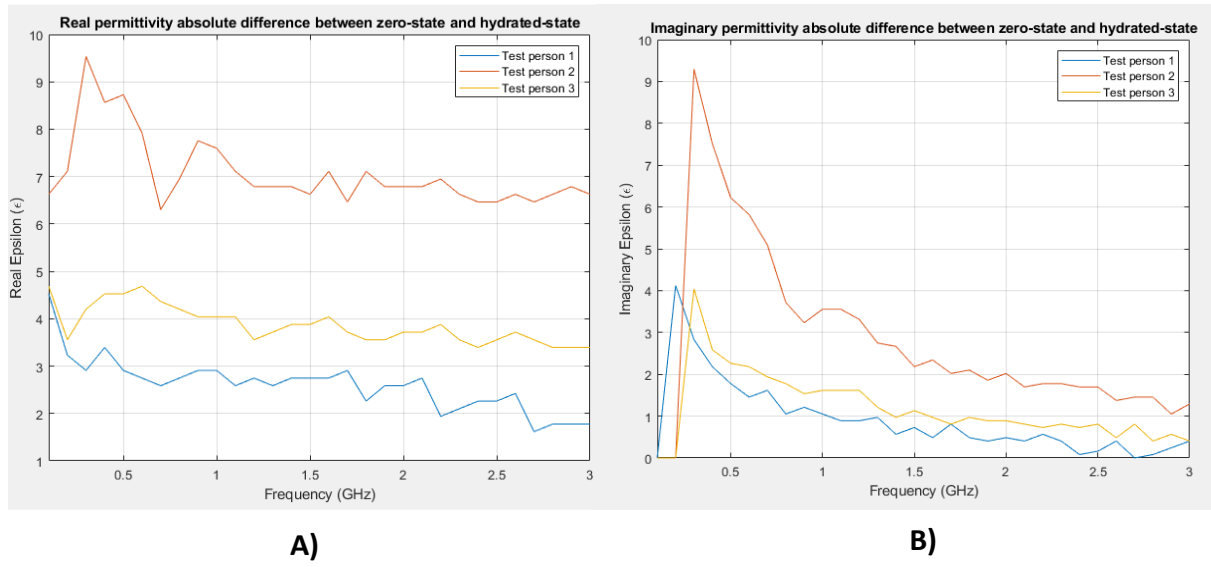


Figure 61: Absolute difference plotted for a) real permittivity b) imaginary permittivity.

4.7 Conclusion

The measurement system consists of different building blocks, with each of them can influence the performance of the measurements. The first influence, which is examined is the interconnection between the VNA and the pin and patch. Here the cable is tortured in multiply manners to detect the influence. From the measurements results noticeable is that the cable distortion does have an influence on the S11-parameter measurement and the imaginary measurements of the permittivity. Nevertheless, the imaginary permittivity can be connected to the distortion in the system and is therefore more sensitive to changes in the system. Although, the cable does influence the S11-parameter slightly and the imaginary permittivity, there is chosen to hold the cable in the same position while performing measurements.

The second influence, which is examined, is regarding the contact between the Material Under Test and the pin and patch surface. Here different immersion depths in the liquids are used for measurements. The results from these measurements can be observed in both the S11-parameter and the real and imaginary permittivity measurement. This due to the effect that by immersing the pin and patch too low into the liquid, results in a liquid around the attachment area and can lead to connection flaws. Also, immersing the pin and patch too less into the liquid results in bad spread of the liquids around the ground plane of the pin and patch and thereby will the measurement also result in less accurate. To avoid these influences regarding the MUT interface, each time a measurement occurs with a liquid the immersion level of the pin and patch should stay the same.

The third influence is considering the purity and influence of changing the calibration liquids. These results clearly show that problems are occurring with the liquids, which indicated that the liquids are not pure. It can also be clearly seen that when applying liquids with higher permittivity results in a more accurate measurement around that applied calibration liquids. For example, if you want to measure around 40 ϵ . It is more convenient to use calibration liquids which are around that permittivity.

After examination of the building blocks some precautions and ordering of new liquids is performed. Measurements with the new liquids clearly show progress in the calibration and measurement results. After completion of the calibration and measurements of the permittivity known liquids, skin measurements are performed. From these measurements a clear difference between a nature state of the skin and a hydrated state for three different test persons can be observed. With this difference in mind, it should prove that pin and patch measurements on the skin can give an indication of the hydration level of an individual person.

Finally, from the mentioned results, can be concluded that skin measurements with the designed CMOS permittivity sensor could give an indication of the hydration level of a person and that a same behaviour regarding the hydration state of the skin can be observed for different persons.

5. Proposed system

To enable measurements using the CMOS permittivity sensor, different components are required to create the input signals for the sensor. These components are described in the following section.

5.1 System block diagram

The system block diagram of the sensor system with inputs and readout system can be seen in Figure 62. The system consists of a crystal oscillator, which will work at the RF and LO frequency. The RF and LO frequencies are locked with each other and this can be achieved by using a PLL system. These signals will be fed to the permittivity sensor, which is discussed in section 2.4. From this sensor output signals are required from the differential bridge output. This output is from the connected part of the patch and the part without the connected patch (dummy result). Each output will be digitalized by an Analog Digital Converter (ADC). This can be one large ADC, which contains more inputs and outputs or two ADCs. After digitalization, an algorithm will be introduced to make the information readable and give a translation for the hydration level in the human body. Each of these components will be discussed in more detail.

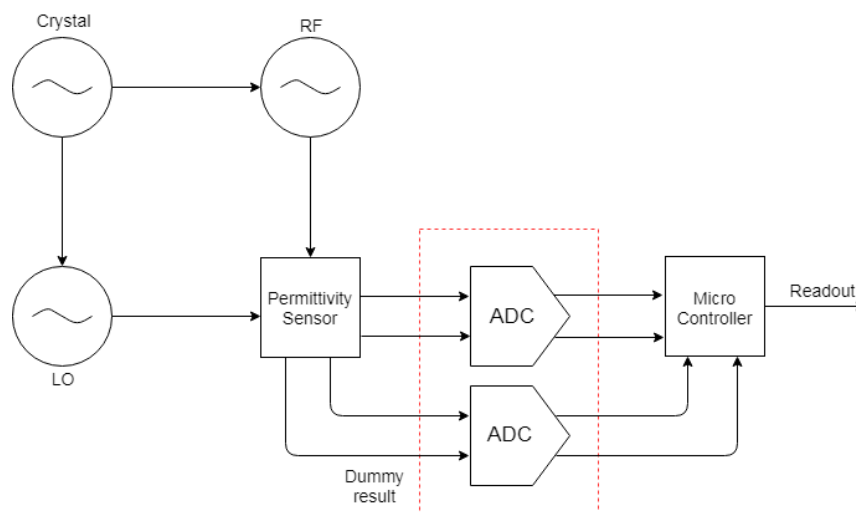


Figure 62: System overview of the sensor with input and readout circuit.

5.1.1 Crystal

It is desired to let the RF and LO work around the frequency range of 1-3 GHz. Therefore it is convenient to use a crystal oscillator which is used for the phase comparator of the PLL. Another large influence is regarding the phase noise. For instance, when the crystal operates at a frequency range of 10-100 MHz, it is desired that the phase noise should not increase too much in this range. When this is not happening the phase noise can flow through the whole system and increase the noise and thereby the performance of the circuit. Decided to use is the CWX813 fixed frequency Crystal Controlled Oscillator [73].

5.1.2 Phased Locked Loop (PLL)

To make sure that the LO and RF signals for the permittivity sensor are locked with each other it is necessary to use a PLL. The PLL should be able to have a frequency output range of 500 MHz till 4.4 GHz. Furthermore, it is in ease when the programming language of this PLL is a standard interface (SPI for example). Also it is desired to let the PLL have one input node for the crystal oscillator and four output signals for the RF-, RF+ and LO-, LO+ signals. Moreover, should the phase noise not contribute in a large amount to the overall noise (< -160 dBc/Hz). With these specifications in mind, there is chosen to use the LMX2581 Wideband Frequency Synthesizer with Integrated VCO [74].

5.1.3 Permittivity sensor

After the RF and LO signal are locked, these signals will be fed to the permittivity sensor, which was described in section 2.4. The permittivity sensor will give a dummy result (from the Wheatstone bridge

without the attached patch) and a real output from the Wheatstone bridge with the attached patch. Both of these signals should be examined and made digital for later calibration processes. The permittivity CMOS sensing array needs to have a RF and LO driver. Even though the selected PLL is able to generate two times a differential output frequency, there is chosen to use two PLLs instead of one. This due to the fact that both differential output frequencies are linked to each other and do not work independently, which is required for the RF and LO frequency.

5.1.4 Analog Digital Converter (ADC)

As mentioned before, both the dummy and real result should be converted to the digital domain. This can be achieved by implementing an ADC. Besides the voltage input range, is it handy to have an ADC that is also able to examine the result of the patch and the dummy result, by only using one big ADC with 4 inputs (2x differential). Furthermore, are the voltage outputs of the permittivity sensor small in amplitude (around the 0 till 1.2V). Therefore an amplifier can be used to enhance the voltage amplitudes to the full input swing of the chosen ADC.

5.1.5 Microcontroller

To create a readout signal, a microcontroller should be used to convert the digital signal from the ADC to a visual interpretation of the hydration level by applying an algorithm. The specifications for such a microcontroller are as follows:

- There should be enough memory available to perform signal readout on the real signal and dummy signal
- Security should be implemented on the microcontroller for human privacy.
- Communication between PC and microcontroller should be able

Instead of using both a microcontroller and an ADC there is chosen to use a st board. This board is capable of converting analogue signals to digital signals. This st board is called the STM32 Discovery kit [75].

6. Prototype design

To enable a portable readout system, a PCB should be designed where the measurements and the readout of the system can occur. This PCB will consist of the signal generation provided by the crystal oscillator. This frequency signal will be sent to the PLLs and the signal from the PLL will be sent to the CMOS sensing array. Finally the output signal will be read using the ST board. First, the total board design will be discussed. Secondly, from the total board overview each component will be discussed.

6.1 PCB board design

The final PCB board design schematic can be seen in Figure 63.

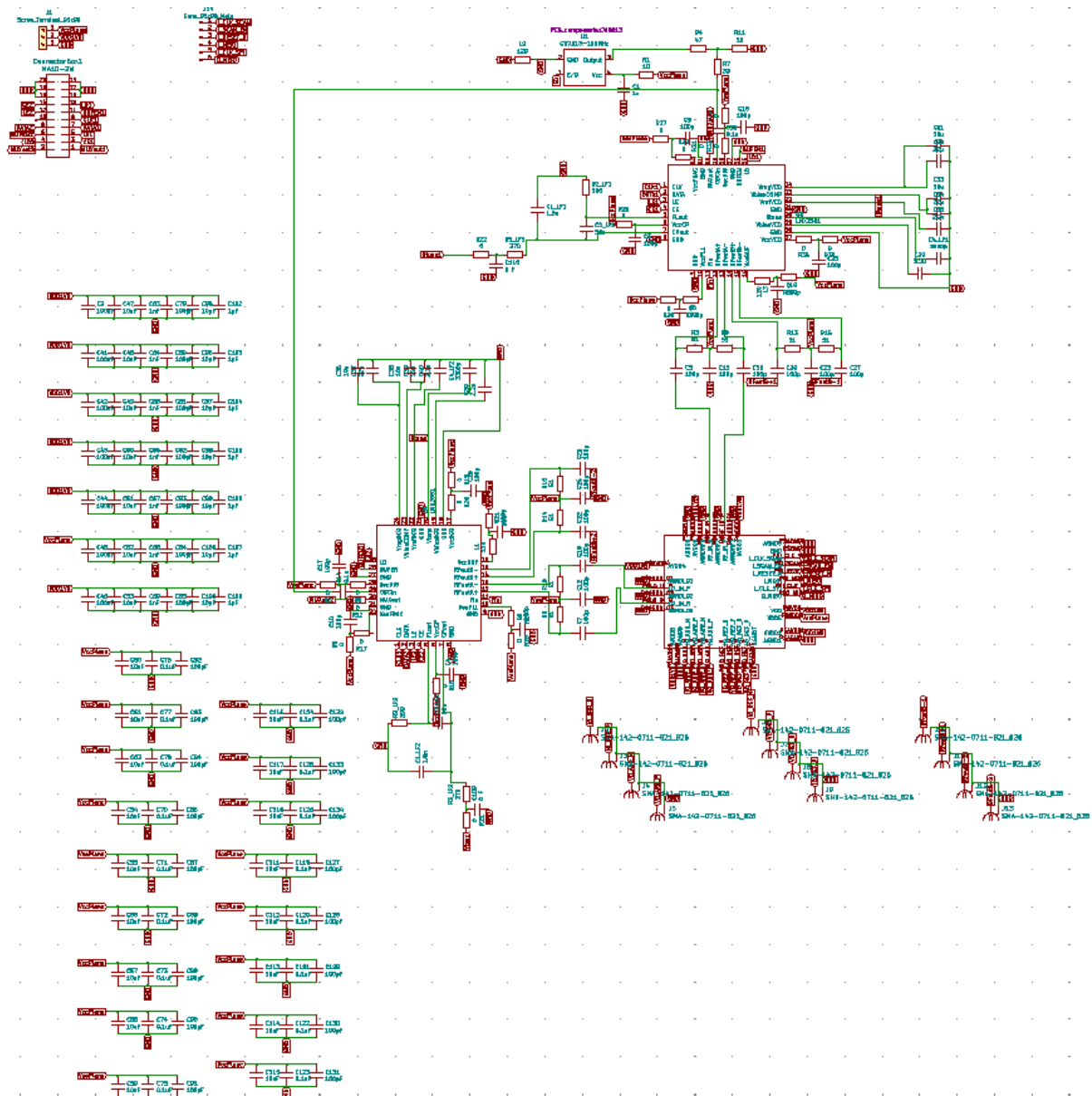


Figure 63: Schematic of input board for CMOS sensing array.

The created layout from the schematics can be found in Figure 64. There is chosen to design the PCB using 4 copper layers. The first copper layer is used for the connections of the components. The second copper layer is chosen to be a uniform layer and is the general ground plane. The third copper layer is chosen to be for the 3.3 V supply and the fourth copper layer is used for the 1.8V supply. Furthermore, a screw connection is chosen for the supply of the voltages and ground. The output voltages and currents from the CMOS sensing array is connected to a SMA coaxial connector. Also, the RFoutB+ and

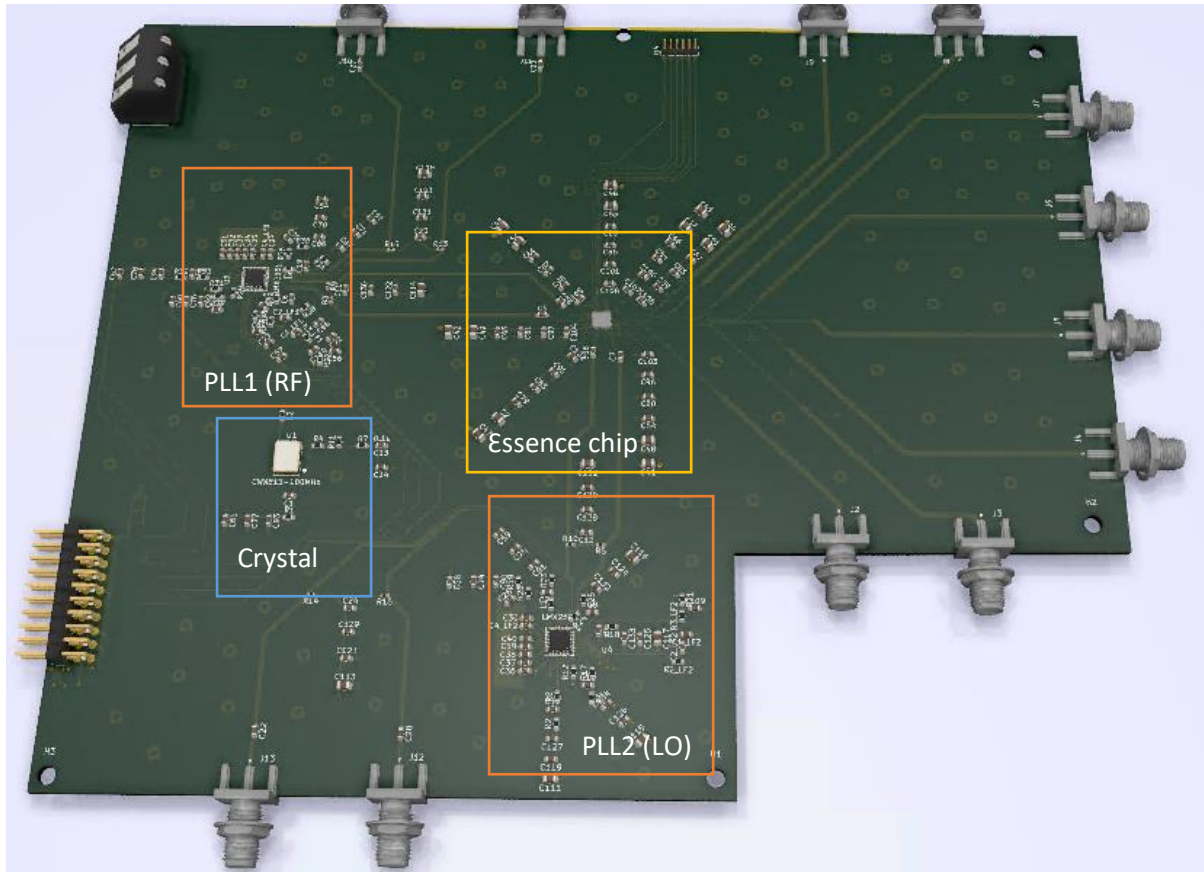


Figure 65: 3D view of the designed PCB layout.

6.2 Signal generation

As described in the proposed system section, there is chosen to use the CWX813 for the generation of the input frequency signal for the PLLs. First a schematic representation in a PCB generator should be performed in order to design the crystal oscillator implementation. For the PCB generator there is chosen to use the program KiCad. The designed schematic can be seen in Figure 66. To minimize crosstalk of the reference input, capacitor C1 can be placed between the supply voltage and the Vcc. Furthermore, the E/D pin should be left open to enable the output. Moreover, a ferrite bead is used between the GND_Osc and the common ground to prevent crosstalk. The resistors R4 (47 Ω), R15 (18 Ω) and R7 (33 Ω) are placed in such a way that a 50 Ω output impedance can be seen from the OSCin pin. Additionally, C13 is placed as DC blocker. Finally to create a uniform VccPlane, capacitors are created in the line to decouple the signal.

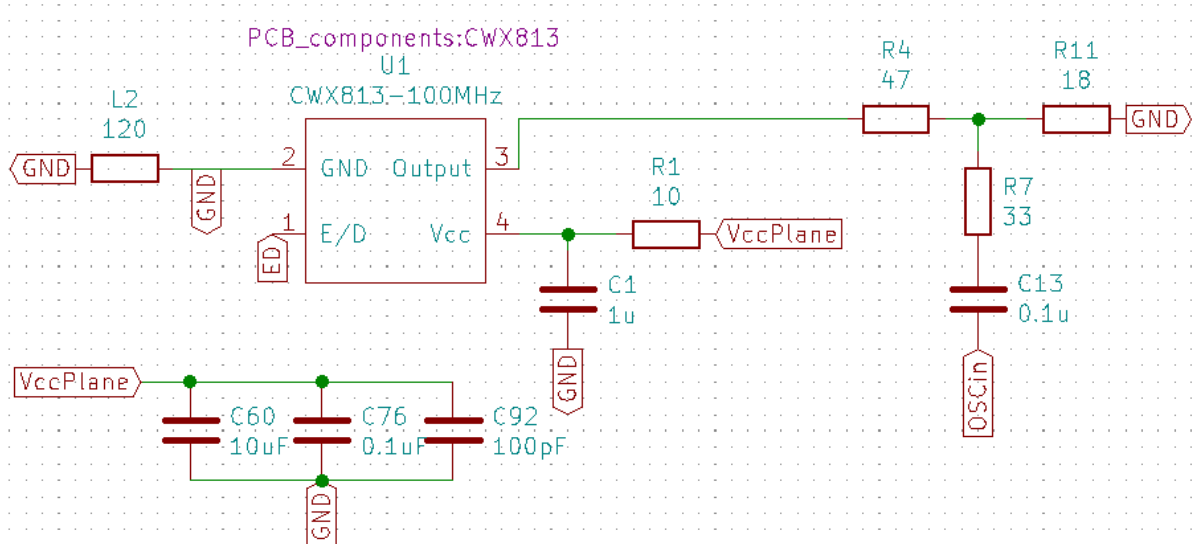


Figure 66: Schematic design for the crystal oscillator CWX813.

From the schematic design a PCB layout is generated (see Figure 67). Here can be seen that the VCCplane signal input voltage is defined in a different coper layer. Moreover, the ground pads are connected through a via to a different coper layer of the PCB. The crystal signal generator should drive two PLLs as explained in Section 5. Therefore, two capacitors are placed after the resistor divider and from both the capacitors the PLL get their OSCIn signal.

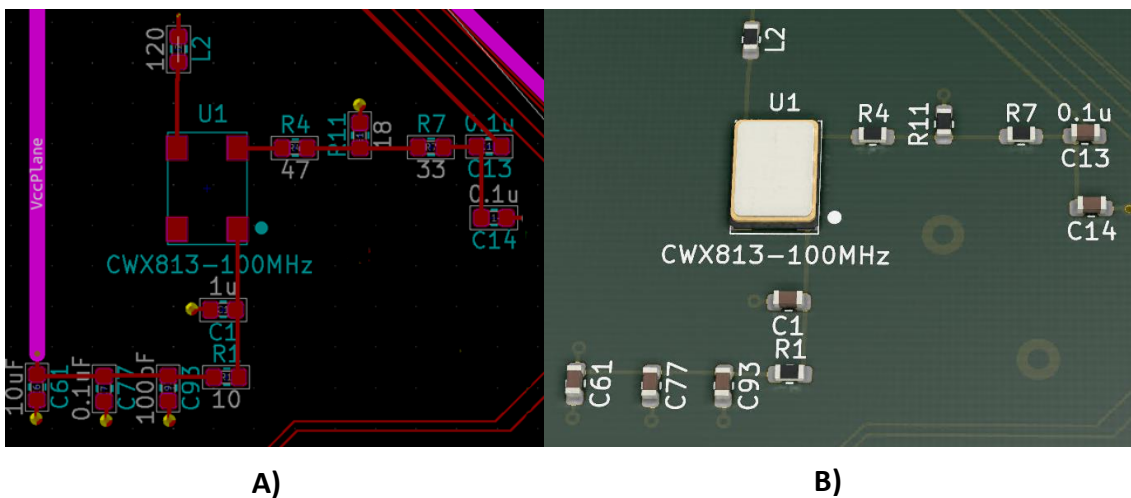


Figure 67: a) Layout of the crystal oscillator b) 3D view of the crystal oscillator.

6.3 PLL design

As mentioned in the proposed system section, two PLLs are required. When following the user's guide [76] to create the schematic, the creation of the schematic in Figure 68 in KiCad is accomplished. Note that only here the RFoutA+ and – will be sent to the CMOS sensing array. Moreover, 50 Ω RF lines are needed to prevent signal loss. The design of these RF lines will be discussed in the next section.

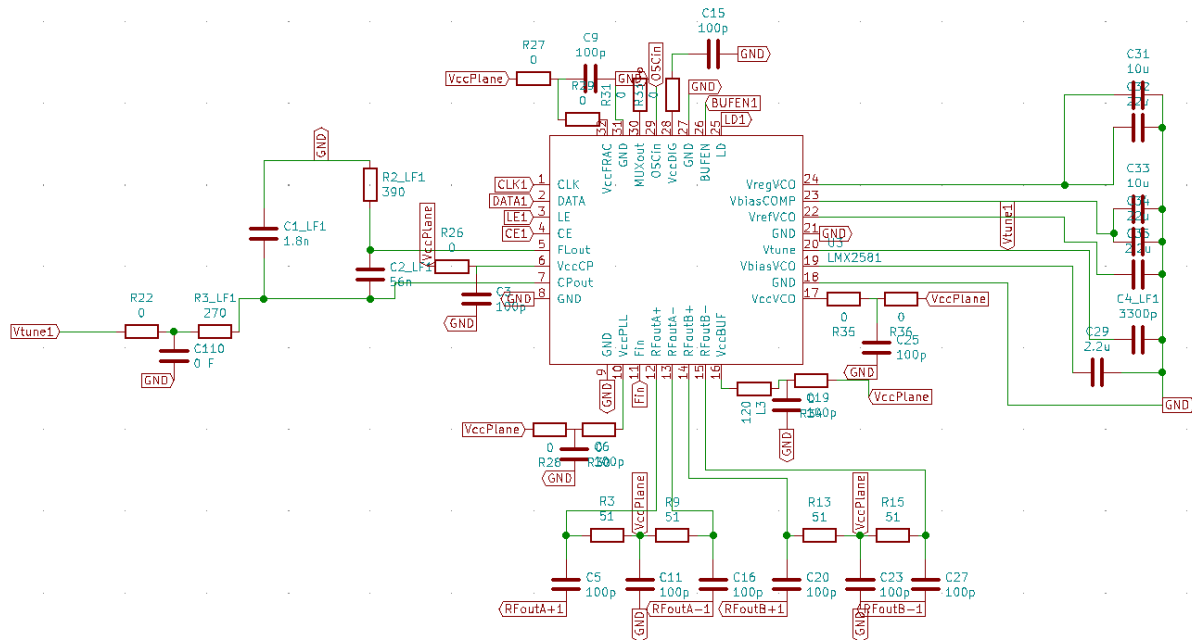


Figure 68: Schematic design for the PLL LMX2581.

The generated layout for a single PLL configuration can be seen in Figure 69. Vias are also used for the ground connections.

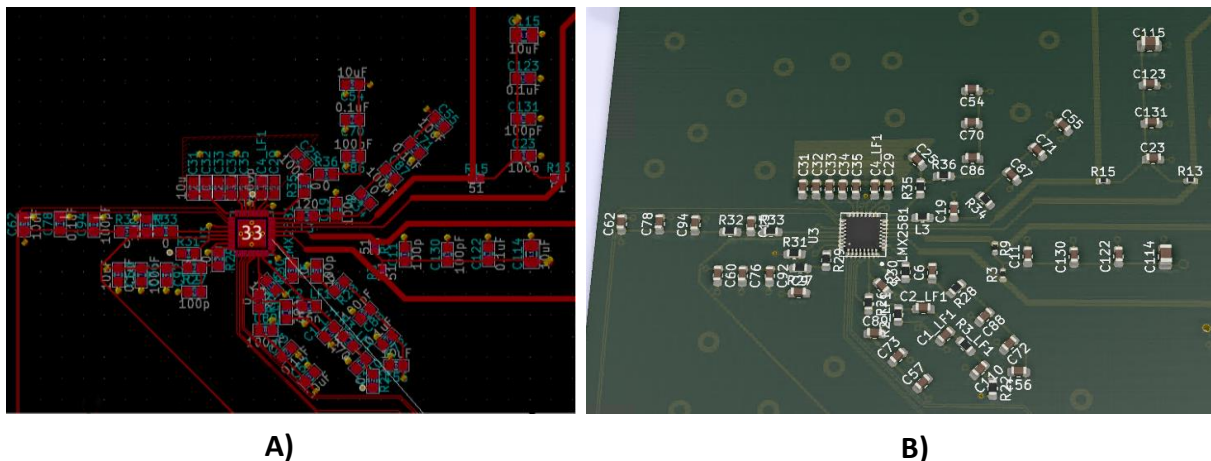


Figure 69: a) Layout of one PLL LMX2581 b) 3D view of the PLL LMX2581

6.4 RF line generation

The CMOS sensing permittivity array uses a RF frequency in the range of 1.01 GHz to 3.01 GHz. Then, the LO frequency uses the frequency range 1 GHz to 3 GHz. Resulting in an output frequency of approximately 0.01 GHz => 10 MHz. Especially for the RF and LO frequencies a, 50 Ω impedance line is needed. There is chosen to use a microstrip implementation for this.

Here the signal is fed to the CMOS sensing array using the top metal layer. The chosen ground plane layer is the second copper layer. The distance of these two layers is given by Eurocircuits [77] and is given to be 0.36 mm. Using the program Advanced Design System (ADS), the following line specifications can be found, see Figure 70. This results in a width of 0.72 mm in the first copper layer. The length can be changed to a self-chosen value.

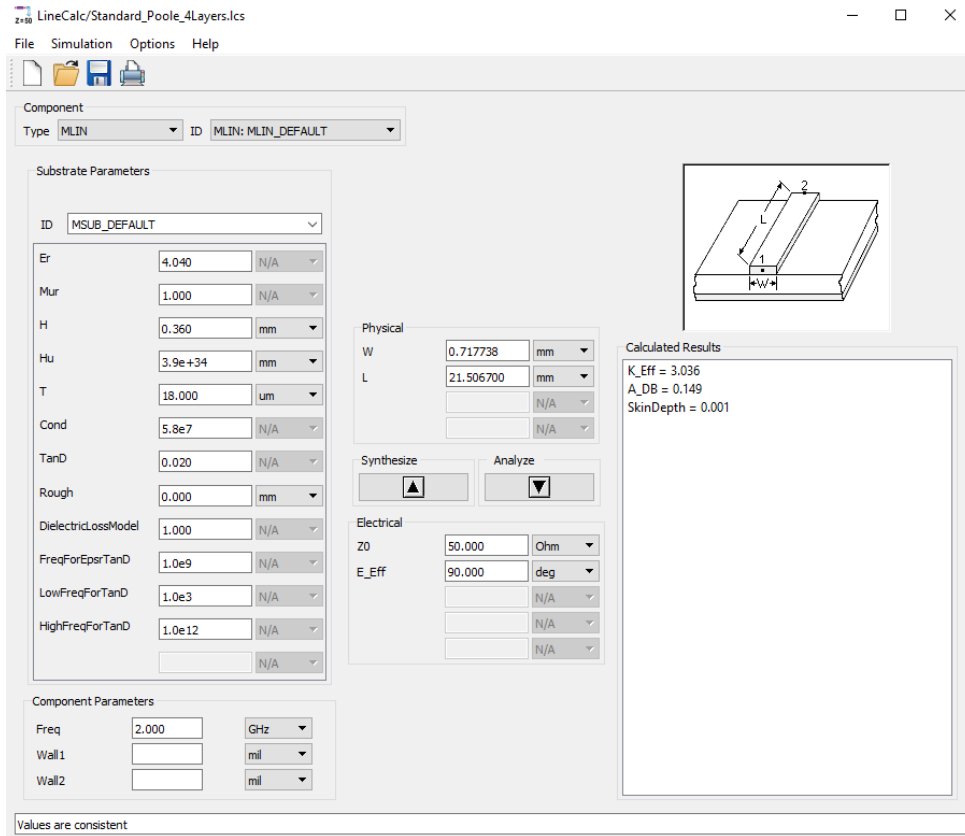


Figure 70: Calculation of RF line using ADS.

6.5 CMOS sensing array

The schematic of the CMOS informer chip can be seen in Figure 71. The input signals that are needed for CMOS chip are; the control signals from the μ Controller given by I_MISO, I_CLK_SPI, I_CLK_SCAN, I_RESET_N and I_SCAN_EN. The supplies needed are; supply of 1.8V, 3.3V and a ground connection. As described in section 2.4 the output signals are given for a single pixel readout system regarding the current and voltage. Also the array result is given in voltage and current representation. Finally it is able to read the state of the chip with the O_MISO pin. When communicating through a SPI interface to the chip, the chip can be considered to be the slave.

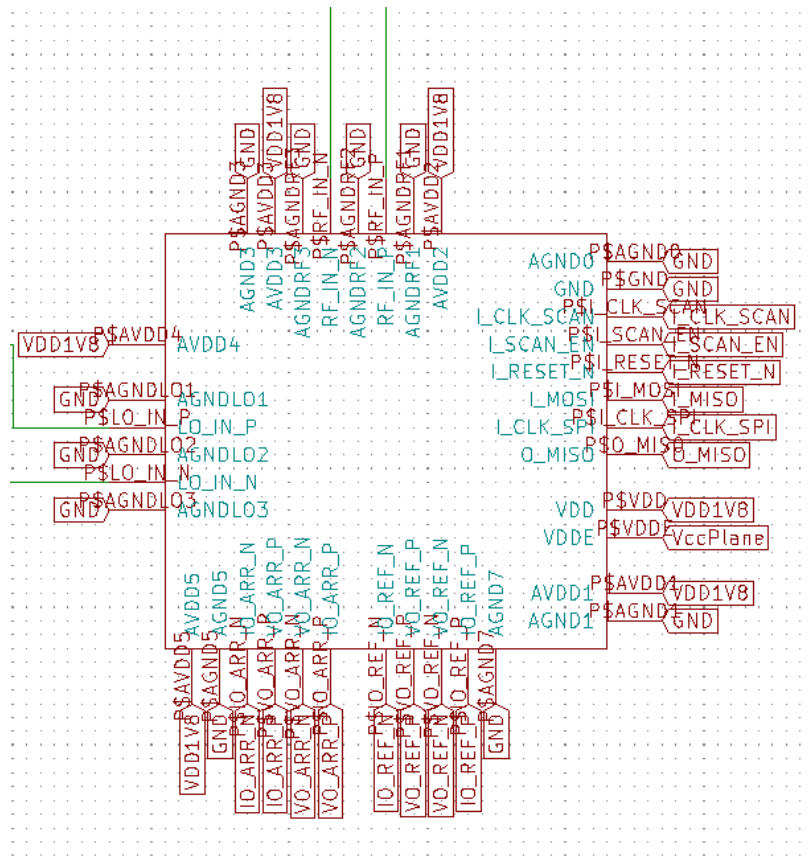


Figure 71: Schematic of the CMOS sensing array.

Transforming the schematic to a layout results in Figure 72. Due to the small size of the chip (2.5 by 2.3mm) the connections on the chip are also small. Furthermore, decoupling capacitors are present on each supply line towards the chip.

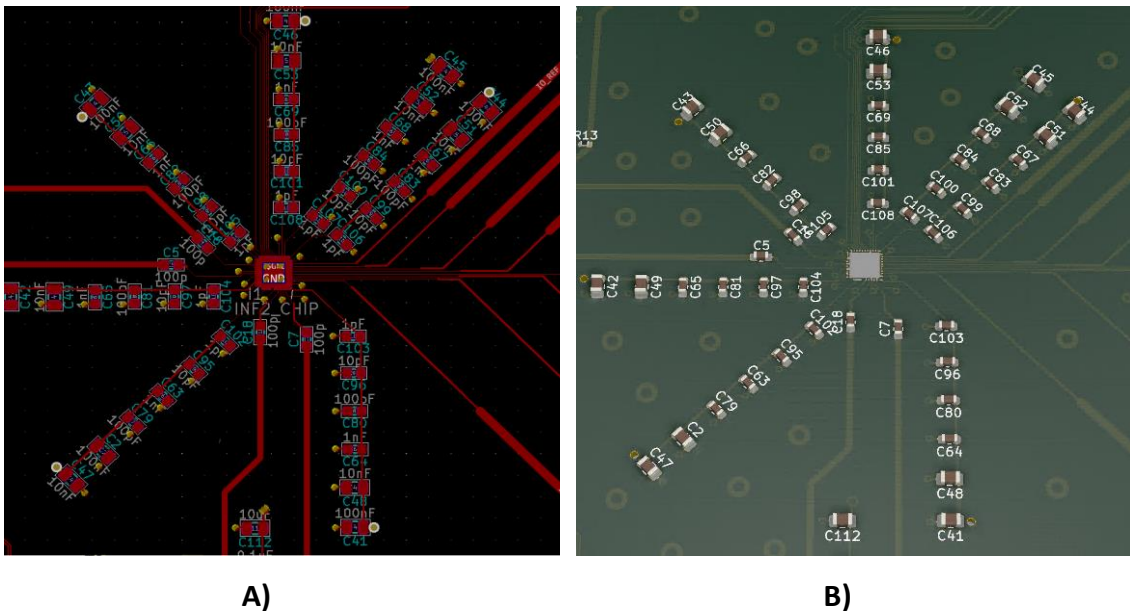


Figure 72: a) Layout of the CMOS permittivity sensor b) 3D view of CMOS permittivity sensor.

7. Conclusion

To conclude, for the design of a portable permittivity sensor three major adjustments are required on the existing CMOS permittivity sensing array chip. The first adjustment is the design of a packaging system where the chip is encapsulated from any harmful inputs. This packaging is initially processed by using bare silicon dummy wafers where SU8 metallized pillars are created and cavities in SU8 filled with metal particles. To create the SU8 metallized pillars, different parameters influenced the processing steps. First, the spin coating speed is examined regarding the SU8 created thickness. The second parameter that is examined, is regarding the metallization step of the SU8 pillars. Here a 4 μm aluminium layer is sputtered during a low power intensity with cooling down steps between. Finally, the spray coating of the AZ9260 and the etching time of the aluminium are carried out. From these dummy wafer results, it can be concluded that spin coating SU8 with a speed of 800 rpm creates a $> 200 \mu\text{m}$ SU8 pillar. Exposure time for the created SU8 pillars should be 1170 mJ/cm^2 and follows a development time of 30 minutes. Regarding the development of the AZ9260, an exposure dose of 900 mJ/cm^2 and development time of 3 minutes are required. However, these values could vary due to the created inequality of development between and on the SU8 pillars.

The second task is regarding the validation measurements. Validation measurements are performed using a pin and patch configuration. Here, different geometries are available for performing measurements. A Matlab code has to be designed to allow measurements in a GUI interface setting. During the measurements, different building blocks were able to influence the measurements. The first influence that is inspected, is regarding the interconnection influences. These results concluded that the interconnection did not influence the real permittivity measurements in a large manner. The second influence is regarding the MUT interface. Here different depth measurements are carried out and showed that the depth of the pin and patch in the liquid matters for the measurement. To minimize this influence in following measurement, is chosen to perform measurements at the same liquid depth for each liquid. The final influence that is inspected, is regarding the use of the calibration liquids. This result shows that using calibration liquids around the same MUT permittivity, gives a more precise measurement. Finally, the measurements regarding the skin hydration are performed. Here is a clear difference between a neutral skin state and a hydrated skin state visible, which concludes that detection of hydration is possible using a pin and patch configuration.

The final adjustment is to design a PCB layout, where the signals are generated for the CMOS permittivity sensor. To do this, different components are required, specifically; a crystal oscillator, two PLLs and the CMOS permittivity array chip. The PCB design is carried out in the program KiCad where a schematic implementation of the PCB first needs to be designed to finally generate a layout. In addition to the components to generate the signals, connectors and 50Ω RF lines are designed to allow better performance.

8. Discussion

This thesis contains the three major parts, which are the packaging, validation measurements and the PCB design. Regarding each part, a discussion and further recommendations can be given.

For the packaging, lots of factors are affecting the performance of the packaging solutions. More insight is generated on the dummy wafer processes. However, to ensure right alignment, a more precise layout of the CMOS permittivity sensor should be given. Due to the lack of information (no Gerber files with exact locations of the patch array), assumptions had to be made, which resulted in degraded alignment of the patches.

Furthermore, information regarding the material used in the patches was shared in a later stage of the project. This gave the insight that the patches were not made of pure Al, but made of an Al with Cu alloy instead. Copper is a contaminant that is not allowed in most processes and machines in the cleanroom. Therefore, an HSE step to remove native oxide on the Al alloy patches was not allowed. This led to the effect that a process needs to be designed or defined to be able to remove aluminium oxide, before depositing aluminium on the SU8 pillars.

Also, due to removal of the old mask aligner, a new training was needed for the new mask aligner, resulting in the lack of processing steps, which should be performed in the cleanroom.

For the final results an observation is made that the thickness of the SU8 is not consistent due to the height difference on the wafer. To perform an equal SU8 layer to this chip, it is convenient to place structures around the chip that have the same height as the chip. This creates a plateau and enables more accurate heights around the chips. Creation of this uniform plateau can be created by attachment of the residues that are located on the fabrication wafer of the chip.

In addition, the alignment of the pillars to the patches was far from ideal, due to the use of the alignment markers on both sides of the wafer. However, as designed in the masks, there are two patches which will be sacrificed for the alignment. By moving the microscopes, alignment can be performed using the patches as alignment markers instead of the standard alignment markers given on the left and right side of the wafer. Nevertheless, as mentioned before, it is this not allowed in the new mask aligner and therefore the tool owner should be contacted to perform these alignments or a different machine should be used.

Regarding the validation measurements, the following discussion points are present. The code received from the previous user to generate the pin and patch S11-parameters, was not working for the first few iterations. Due to this unknowing fact, attempts to let the code work were carried out. After discovery of the incomplete code, changes had to be made and a new code had to be developed to work with the changes. Furthermore, due to impurity of the liquids, new liquids had to be ordered. However, the company responsible for this, waited 3 months before delivering, which resulted in time management issues.

To improve the skin measurements and to get more insight into the hydration of the human skin, other measurements can be carried out. The first measurement is to look at the hydration level after exercising when a person is sweating. The second measurement is when a person has consumed a lot of water, thereby moisturizing the skin.

For these measurements, the VNA is used with a cable connector. Using a different VNA whereby no cable connector is needed can also improve the measurements and is more convenient in use.

Finally, when looking at the PCB, there are some recommendations that can be taken into account. To enable a small portable sensor, the readout system can also be designed with the current, already designed signal generation for the CMOS sensor. Establishing a Bluetooth connection allows a wearable portable sensor without wires.

Bibliography

- [1] D. E. Bloom, "7 billion and counting," *Science*, vol. 333, no. 6042, pp. 562-569, 2011.
- [2] B. M. Popkin, K. E. D'Anci, and I. H. Rosenberg, "Water, hydration, and health," *Nutrition reviews*, vol. 68, no. 8, pp. 439-458, 2010.
- [3] W. L. Kenney and P. Chiu, "Influence of age on thirst and fluid intake," *Medicine science in sports exercise*, vol. 33, no. 9, pp. 1524-1532, 2001.
- [4] M. Frangeskou, B. Lopez-Valcarcel, and L. Serra-Majem, "Dehydration in the elderly: a review focused on economic burden," *The journal of nutrition, health aging*, vol. 19, no. 6, pp. 619-627, 2015.
- [5] J. Lemmetyinen *et al.*, "Snow density and ground permittivity retrieved from L-band radiometry: Application to experimental data," vol. 180, pp. 377-391, 2016.
- [6] M. F. Anatomy and Physiology II, Electrolyte, and Acid-Base Balance, "Body Fluids and Fluid Compartments," *OER services*, 2019.
- [7] J. Kanitakis, "Anatomy, histology and immunohistochemistry of normal human skin," *European journal of dermatology*, vol. 12, no. 4, pp. 390-401, 2002.
- [8] D. Chu, "Overview of biology, development, and structure of skin. K. Wolff, LA Goldsmith, SI Katz, BA Gilchrist, AS Paller, & DJ Leffell," ed: New York: McGraw-Hill, 2008.
- [9] BCcampus. (2019). *ANATOMY AND PHYSIOLOGY*.
- [10] T. G. Berger, D. M. Elston, and W. James, *Andrews' diseases of the skin: clinical dermatology*. Saunders Elsevier, 2006.
- [11] C. Härle-Bachor and P. Boukamp, "Telomerase activity in the regenerative basal layer of the epidermis in human skin and in immortal and carcinoma-derived skin keratinocytes," *Proceedings of the National Academy of Sciences of the United States of America*, vol. 93, no. 13, p. 6476, 1996.
- [12] M. L. Huggins, "The structure of collagen," *Proceedings of the National Academy of Sciences of the United States of America*, vol. 43, no. 2, p. 209, 1957.
- [13] T. Myers, *Mosby's dictionary of medicine, nursing & health professions*. Mosby Inc, 2006.
- [14] T. Mauro and L. Goldsmith, "Biology of eccrine, apocrine, and apoeccrine sweat glands," *Fitzpatrick's dermatology in general medicine*, vol. 7, pp. 713-720, 2008.
- [15] P. A. Kolarsick, M. A. Kolarsick, and C. Goodwin, "Anatomy and physiology of the skin," *Journal of the Dermatology Nurses' Association*, vol. 3, no. 4, pp. 203-213, 2011.
- [16] G. Murphy, "Histology of skin: Lever's histopathology of skin," ed: Philadelphia: Lippincott Raven, 1997.
- [17] R. F. Rushmer, K. J. Buettner, J. M. Short, and G. F. Odland, "The skin," *Science*, pp. 343-348, 1966.
- [18] P. J. Coenraads, "Skin hydration discussion," E. v. d. Lingen and A. Steijlen, Eds., ed, 2019.
- [19] D. Schoeller, R. Kushner, P. Taylor, W. Dietz, and L. Bandini, "Measurement of total body water: isotope dilution techniques," in *Ross Conference on Medical Research*, 1985.
- [20] W. P. Bartoli, J. M. Davis, R. R. Pate, D. S. Ward, and P. D. Watson, "Weekly variability in total body water using 2H₂O dilution in college-age males," *Medicine science in sports exercise*, vol. 25, no. 12, pp. 1422-1428, 1993.
- [21] P. Ritz, "Bioelectrical impedance analysis estimation of water compartments in elderly diseased patients: the source study," *The Journals of Gerontology Series A: Biological Sciences Medical Sciences*, vol. 56, no. 6, pp. M344-M348, 2001.

- [22] N. Bohnen, D. Terwel, M. Markerink, J. A. Ten Haaf, and J. Jolles, "Pitfalls in the measurement of plasma osmolality pertinent to research in vasopressin and water metabolism," *Clinical chemistry*, vol. 38, no. 11, pp. 2278-2280, 1992.
- [23] L. Armstrong, J. Soto, and F. Hacker, "Urinary indices during dehydration, exercise, and rehydration," *Occupational Health Industrial Medicine*, vol. 2, no. 40, p. 97, 1999.
- [24] L. E. Armstrong *et al.*, "Urinary indices of hydration status," *International Journal of Sport Nutrition Exercise Metabolism*, vol. 4, no. 3, pp. 265-279, 1994.
- [25] J. M. Saavedra, G. D. Harris, S. Li, and L. Finberg, "Capillary refilling (skin turgor) in the assessment of dehydration," *American journal of diseases of children*, vol. 145, no. 3, pp. 296-298, 1991.
- [26] L. E. Armstrong, "Hydration assessment techniques," *Nutrition reviews*, vol. 63, no. suppl_1, pp. S40-S54, 2005.
- [27] G. Vlachogiannakis *et al.*, "A compact energy efficient CMOS permittivity sensor based on multiharmonic downconversion and tunable impedance bridge," in *2018 IEEE International Microwave Biomedical Conference (IMBioC)*, 2018, pp. 1-3: IEEE.
- [28] Y. Nikawa and S. Nakamura, "Microwave application in medical sensing," in *2015 9th International Symposium on Medical Information and Communication Technology (ISMICT)*, 2015, pp. 131-133: IEEE.
- [29] F. Zhu and J. Spronck, "A capacitive tactile sensor for shear and normal force measurements," *Sensors Actuators A: Physical*, vol. 31, no. 1-3, pp. 115-120, 1992.
- [30] J. Nehring, M. Bartels, R. Weigel, and D. Kissinger, "A permittivity sensitive PLL based on a silicon-integrated capacitive sensor for microwave biosensing applications," in *2015 IEEE Topical Conference on Biomedical Wireless Technologies, Networks, and Sensing Systems (BioWireleSS)*, 2015, pp. 1-3: IEEE.
- [31] N. R. Kellogg, "Capacitive tactile sensor," ed: Google Patents, 1986.
- [32] H.-W. Wu, "Label-free and antibody-free wideband microwave biosensor for identifying the cancer cells," *Transactions On Microwave Theory Techniques*, vol. 64, no. 3, pp. 982-990, 2016.
- [33] P. Mehrotra, B. Chatterjee, and S. Sen, "EM-Wave Biosensors: A Review of RF, Microwave, mm-Wave and Optical Sensing," *Sensors*, vol. 19, no. 5, p. 1013, 2019.
- [34] K. Grenier *et al.*, "Integrated broadband microwave and microfluidic sensor dedicated to bioengineering," *Transactions on microwave theory techniques*, vol. 57, no. 12, pp. 3246-3253, 2009.
- [35] A. A. Helmy *et al.*, "A self-sustained CMOS microwave chemical sensor using a frequency synthesizer," *IEEE journal of solid-state circuits*, vol. 47, no. 10, pp. 2467-2483, 2012.
- [36] M. Yuan, E. C. Alocilja, and S. Chakrabartty, "A novel biosensor based on silver-enhanced self-assembled radio-frequency antennas," *IEEE Sensors Journal*, vol. 14, no. 4, pp. 941-942, 2013.
- [37] X. Huang *et al.*, "Epidermal impedance sensing sheets for precision hydration assessment and spatial mapping," *IEEE Transactions on Biomedical Engineering*, vol. 60, no. 10, pp. 2848-2857, 2013.
- [38] E. Pickwell, B. E. Cole, A. Fitzgerald, M. Pepper, and V. Wallace, "In vivo study of human skin using pulsed terahertz radiation," *Physics in Medicine Biology*, vol. 49, no. 9, p. 1595, 2004.
- [39] E. Pickwell, B. Cole, A. Fitzgerald, V. Wallace, and M. Pepper, "Simulation of terahertz pulse propagation in biological systems," *Applied Physics Letters*, vol. 84, no. 12, pp. 2190-2192, 2004.
- [40] Z. D. Taylor *et al.*, "THz medical imaging: in vivo hydration sensing," *IEEE transactions on terahertz science technology*, vol. 1, no. 1, pp. 201-219, 2011.

- [41] J. Y. Suen *et al.*, "Towards medical terahertz sensing of skin hydration," in *MMVR*, 2009, pp. 364-368.
- [42] P. Tewari *et al.*, "Role of collagen in terahertz absorption in skin," in *Advanced Biomedical and Clinical Diagnostic Systems VII*, 2009, vol. 7169, p. 71691A: International Society for Optics and Photonics.
- [43] N. Meyne, G. Fuge, A.-P. Zeng, and A. F. Jacob, "Resonant microwave sensors for picoliter liquid characterization and nondestructive detection of single biological cells," *IEEE Journal of Electromagnetics, RF Microwaves in Medicine Biology*, vol. 1, no. 2, pp. 98-104, 2017.
- [44] H. Torun, F. Cagri Top, G. Dundar, and A. Yalcinkaya, "An antenna-coupled split-ring resonator for biosensing," *Journal of Applied Physics*, vol. 116, no. 12, p. 124701, 2014.
- [45] H. Griffiths, "Magnetic induction tomography," *Measurement science technology*, vol. 12, no. 8, p. 1126, 2001.
- [46] H. Griffiths, "Magnetic induction tomography," *Electrical Impedance Tomography: Methods, History Applications*, p. 213, 2004.
- [47] J. Grant, R. Clarke, G. Symm, and N. Spyrou, "In vivo dielectric properties of human skin from 50 MHz to 2.0 GHz," *Physics in Medicine Biology*, vol. 33, no. 5, p. 607, 1988.
- [48] D. B. Bennett, W. Li, Z. D. Taylor, W. S. Grundfest, and E. R. Brown, "Stratified media model for terahertz reflectometry of the skin," *IEEE Sensors Journal*, vol. 11, no. 5, pp. 1253-1262, 2010.
- [49] P. Maillard *et al.*, "An automated procedure for the assessment of white matter hyperintensities by multispectral (T1, T2, PD) MRI and an evaluation of its between-centre reproducibility based on two large community databases," vol. 50, no. 1, pp. 31-42, 2008.
- [50] J. L. Schepps and K. R. Foster, "The UHF and microwave dielectric properties of normal and tumour tissues: variation in dielectric properties with tissue water content," *Physics in Medicine Biology*, vol. 25, no. 6, p. 1149, 1980.
- [51] D. Cavallo, W. Syed, and A. Neto, "Closed-form analysis of the decoupling properties of artificial dielectric layers," in *2014 IEEE Antennas and Propagation Society International Symposium (APSURSI)*, 2014, pp. 231-232: IEEE.
- [52] P. Aberg, I. Nicander, J. Hansson, P. Geladi, U. Holmgren, and S. Ollmar, "Skin cancer identification using multifrequency electrical impedance-a potential screening tool," *IEEE transactions on biomedical engineering*, vol. 51, no. 12, pp. 2097-2102, 2004.
- [53] E. Topsakal, T. Karacolak, and E. C. Moreland, "Glucose-dependent dielectric properties of blood plasma," in *2011 XXXth URSI General Assembly and Scientific Symposium*, 2011, pp. 1-4: IEEE.
- [54] D. Mittleman, M. Gupta, R. Neelamani, R. Baraniuk, J. Rudd, and M. Koch, "Recent advances in terahertz imaging," *Applied Physics B*, vol. 68, no. 6, pp. 1085-1094, 1999.
- [55] D. B. Bennett *et al.*, "Terahertz sensing in corneal tissues," *Journal of biomedical optics*, vol. 16, no. 5, p. 057003, 2011.
- [56] Z. Moore, D. Patton, S. L. Rhodes, and T. O'Connor, "Subepidermal moisture (SEM) and bioimpedance: a literature review of a novel method for early detection of pressure-induced tissue damage (pressure ulcers)," *International wound journal*, vol. 14, no. 2, pp. 331-337, 2017.
- [57] A. S. M. Mathiesen, K. Nørsgaard, M. F. B. Andersen, K. M. Møller, and L. H. Ehlers, "Are labour-intensive efforts to prevent pressure ulcers cost-effective?," *Journal of medical economics*, vol. 16, no. 10, pp. 1238-1245, 2013.

- [58] L. Demarré *et al.*, "The cost of prevention and treatment of pressure ulcers: a systematic review," *International journal of nursing studies*, vol. 52, no. 11, pp. 1754-1774, 2015.
- [59] T. Ziemssen and T. Siepman, "The Investigation of the cardiovascular and sudomotor autonomic nervous system—a review," *Frontiers in neurology*, vol. 10, 2019.
- [60] P. M. Quinton, "Cystic fibrosis: lessons from the sweat gland," *Physiology*, vol. 22, no. 3, pp. 212-225, 2007.
- [61] K. Sato, W. Kang, K. Saga, and K. Sato, "Biology of sweat glands and their disorders. II. Disorders of sweat gland function," *Journal of the American Academy of Dermatology*, vol. 20, no. 5, pp. 713-726, 1989.
- [62] D. Ayotte and M. P. J. Corcoran, "Individualized hydration plans improve performance outcomes for collegiate athletes engaging in in-season training," *Journal of the International Society of Sports Nutrition*, vol. 15, no. 1, p. 27, 2018.
- [63] Z. Sonner *et al.*, "The microfluidics of the eccrine sweat gland, including biomarker partitioning, transport, and biosensing implications," *Biomicrofluidics*, vol. 9, no. 3, p. 031301, 2015.
- [64] G. Vlachogiannakis, M. A. Pertijs, M. Spirito, and L. C. de Vreede, "A 40-nm CMOS complex permittivity sensing pixel for material characterization at microwave frequencies," *IEEE Transactions on Microwave Theory Techniques*, vol. 66, no. 3, pp. 1619-1634, 2017.
- [65] Z. Hu, G. Vlachogiannakis, M. A. Pertijs, L. de Vreede, and M. Spirito, "A 5×5 Microwave Permittivity Sensor Matrix in 0.14-μm CMOS," in *2018 IEEE/MTT-S International Microwave Symposium-IMS*, 2018, pp. 1160-1163: IEEE.
- [66] T. H. Lee, *The design of CMOS radio-frequency integrated circuits*. Cambridge university press, 2003.
- [67] B. Razavi and R. Behzad, *RF microelectronics*. Prentice hall New Jersey, 1998.
- [68] R. Bagheri *et al.*, "An 800-MHz–6-GHz software-defined wireless receiver in 90-nm CMOS," *IEEE Journal of Solid-State Circuits*, vol. 41, no. 12, pp. 2860-2876, 2006.
- [69] K. Biswas and S. J. M. j. Kal, "Etch characteristics of KOH, TMAH and dual doped TMAH for bulk micromachining of silicon," vol. 37, no. 6, pp. 519-525, 2006.
- [70] Tresky, "Die Bonder Flip Chip Bonder Die Sorter," Tresky, <http://www.emeaelectrosolutions.com/images/Productos/3-Microelectronics/DieBonding/trautomationbrochure.pdf>.
- [71] Microchem. SU-8 2000 PERmanent Epoxy Negative Photoresist Processing Guidelines for: SU-8 2025 SU-8 2035, SU-8 2050, SU-8 2075 [Online].
- [72] H. T. Shivamurthy, "On the Design and Analysis of Micro-metric Resolution Arrays in Integrated Technology for Near-Field Dielectric Spectroscopy," degree of doctor, Electrical Engineering, Delft University of Technology, <http://repository.tudelft.nl/>, ISBN 000-00-0000-000-0, 2019.
- [73] T. C. W. Corporation, "5.0x7.0mm Surface Mount CMOS Clock Oscillator Series," C. Winfield, Ed., ed. <http://www.conwin.com/datasheets/sm/sm126.pdf>, 2008.
- [74] T. Instruments, "LMX2581 Wideband Frequency Synthesizer with integrated VCO," T. Instruments, Ed., ed. https://www.ti.com/lit/ds/symlink/lmx2581.pdf?ts=1593168053479&ref_url=https%253A%252F%252Fwww.ti.com%252Fproduct%252FLMX2581%253Futm_source%253Dgoogle%2526utm_medium%253Dcpc%2526utm_campaign%253Dasc-null-null-GPN_EN-cpc-pf-google-wwe%2526utm_content%253DLMX2581%2526ds_k%253DLMX2581%2526DCM%253Dyes%2526gclid%253DCj0KCQjwudb3BRC9ARIsAEa-

vUtdLoU7pc9kkoS3ENvt 4kqCoN64euVV4CAcWsxLSrKFzdQPhNWxv4aAniFEALw wc B%2526gclsrc%253Daw.ds, 2014.

- [75] S. M. NV, "Ultra-low-power Arm Cortex -M4 32-bit MCU+FPU, 100DMIPS, up to 1 MB Flash, 128 KB SRAM, USB OTG FS, analog, audio," STMicroelectronics, Ed., ed. <https://www.st.com/resource/en/datasheet/stm32l475vg.pdf>, 2019.
- [76] T. Instruments, "LMX2581EVM User's Guide," T. Instruments, Ed., ed. <https://www.ti.com/lit/ug/snau136c/snau136c.pdf?ts=1588082362519>, 2013.
- [77] Eurocircuits. (2020). *PCB calculator*.

Appendix A

Here the graph representations of the measured permittivity from [47] for different skin places are given.

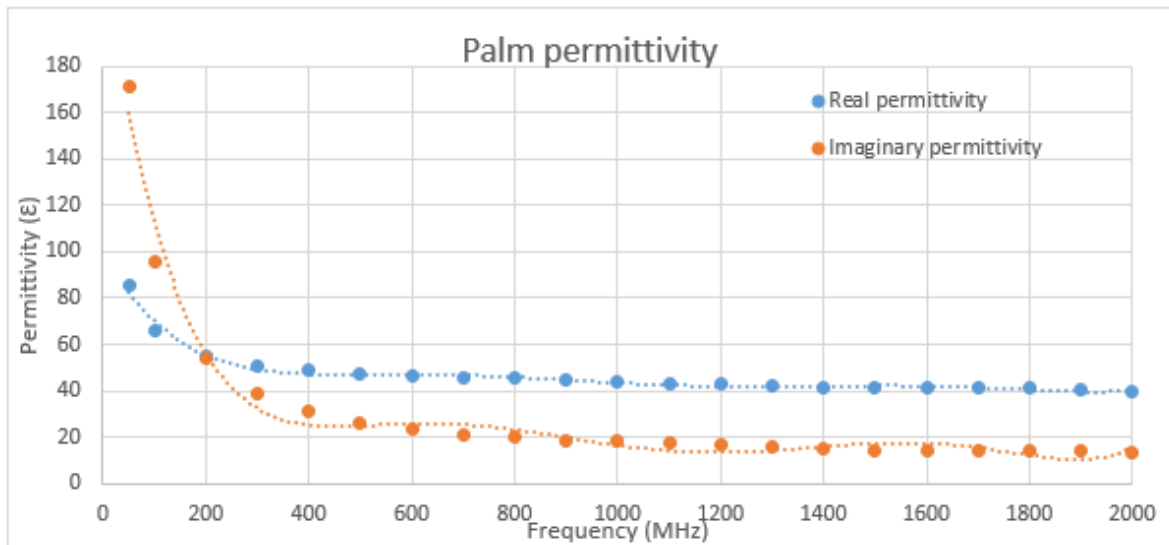


Figure 73: Complex permittivity of the palm measured in vivo [47].

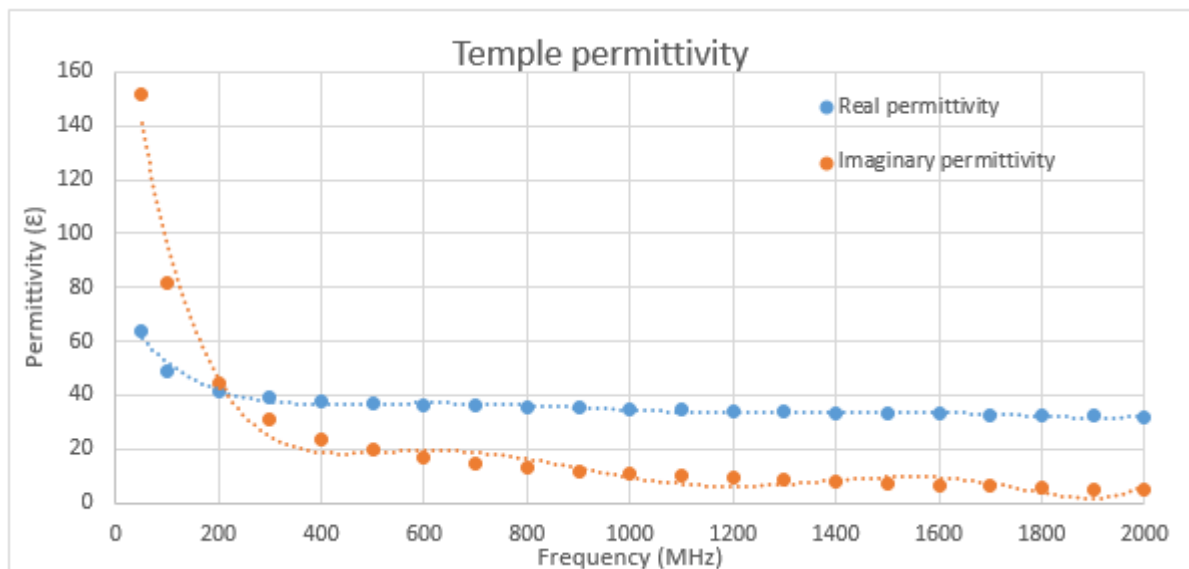


Figure 74: Complex permittivity of the temple measured in vivo [54].

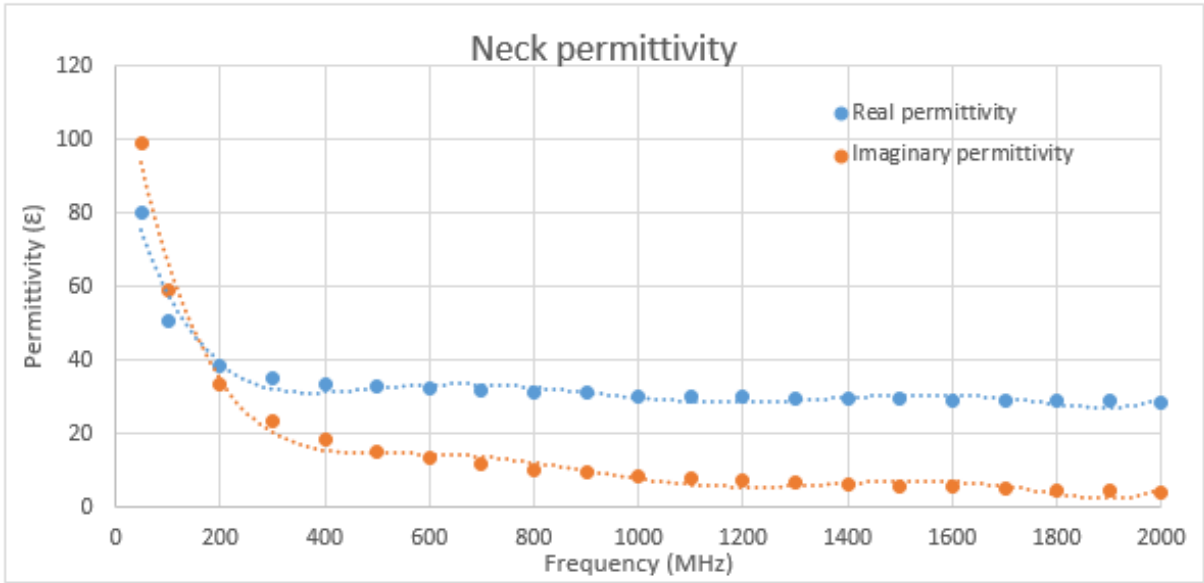


Figure 75: Complex permittivity of the neck measured in vivo [54].

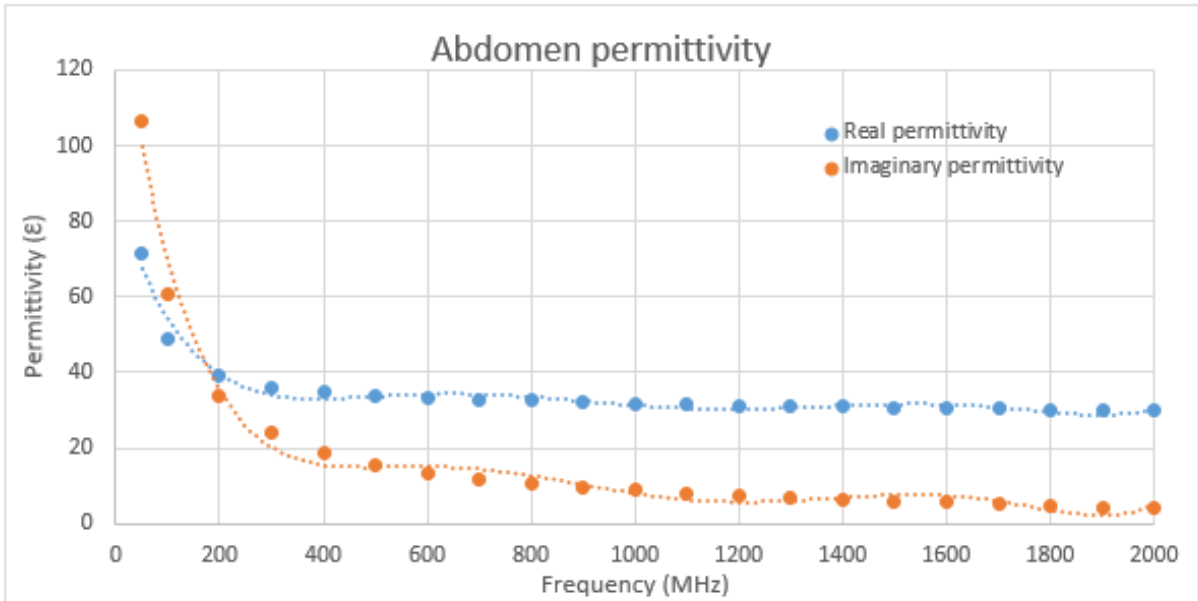
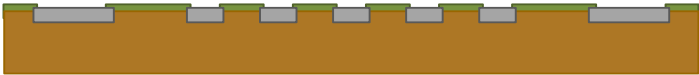


Figure 76: Complex permittivity of the abdomen measured in vivo [54].

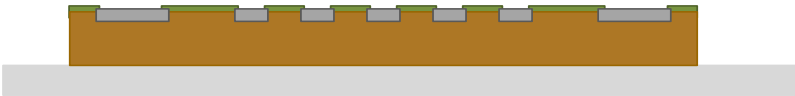
Appendix B

Appendix B.1 Visual representation of processing step for SU8 metalized pillars

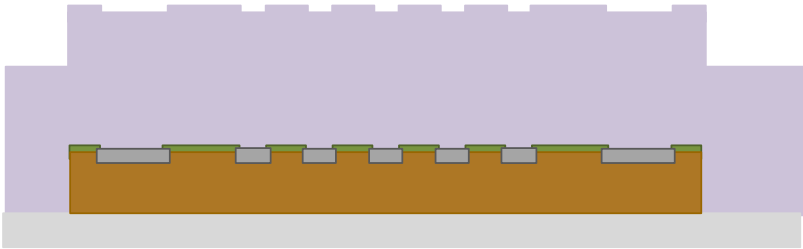
In this section the visual representation for creation of SU8 metalized pillars is given.



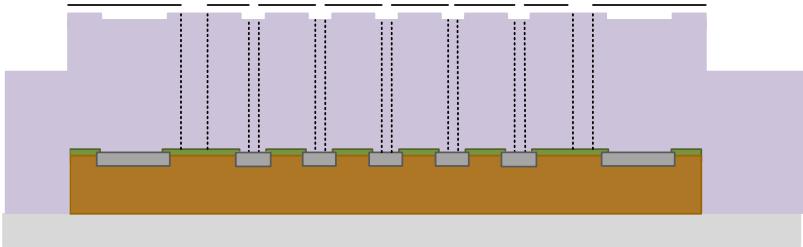
1. The chip



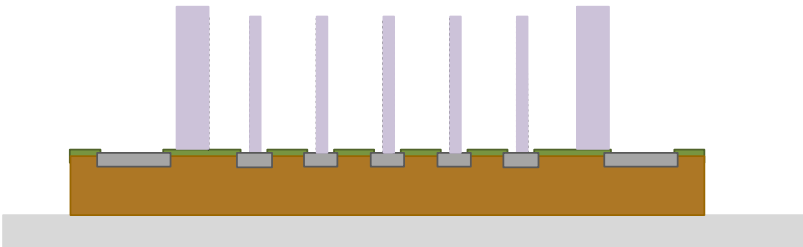
2. Glue the chip to a carrier wafer



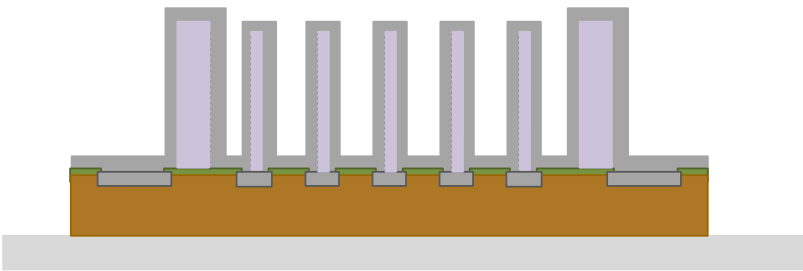
3. Coat with SU8



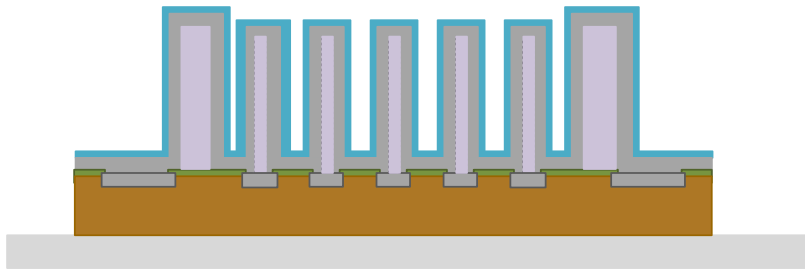
4. Expose in the EVG420 mask aligner



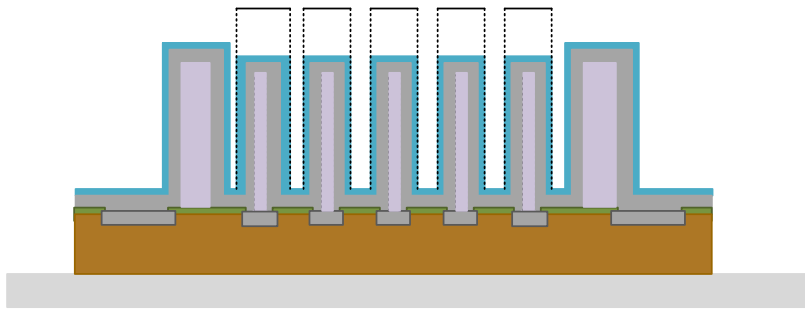
5. Develop in PGMEA



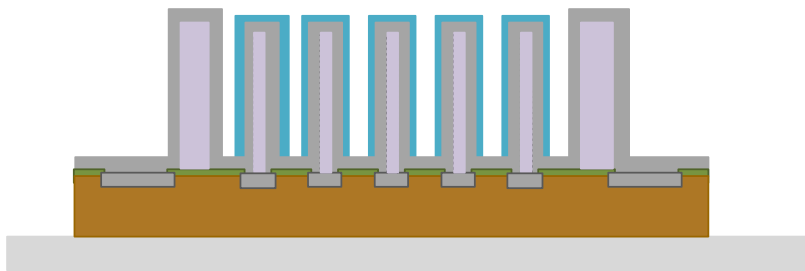
6. Sputter Aluminium + 1% Si



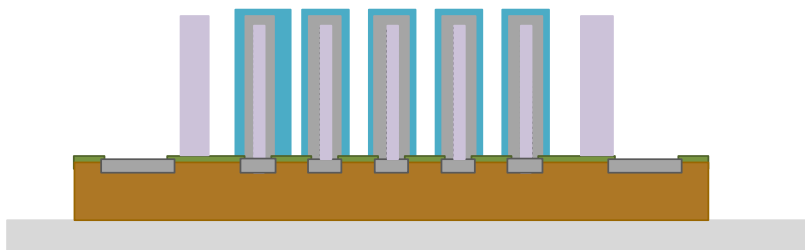
7. Spray coat photoresist EVG spray coater



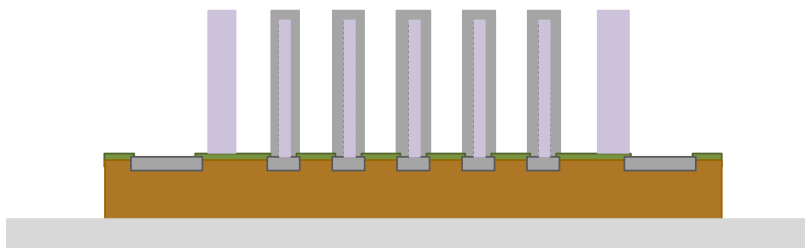
8. Expose in the EVG420 mask aligner



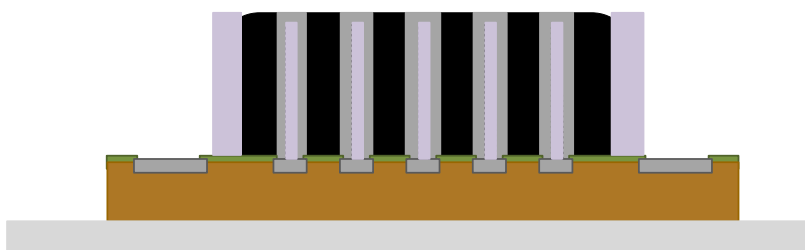
9. Develop (AZ Developer)



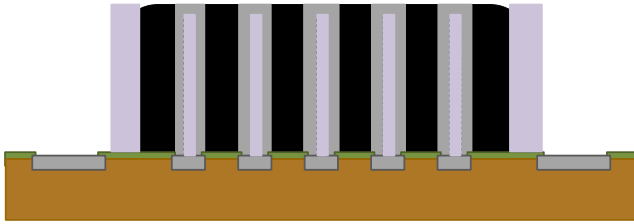
10. Wet etch aluminium



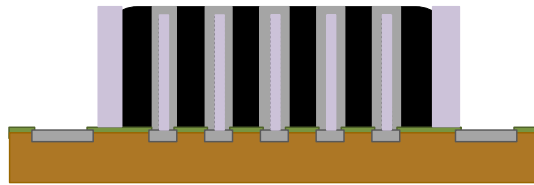
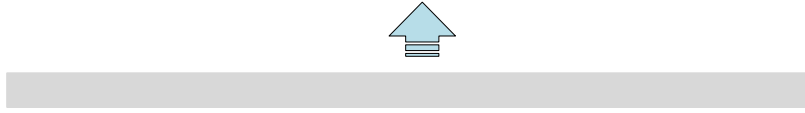
11. Remove photoresist in acetone



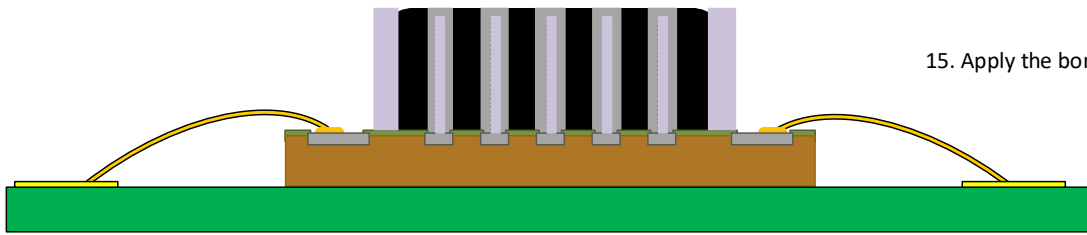
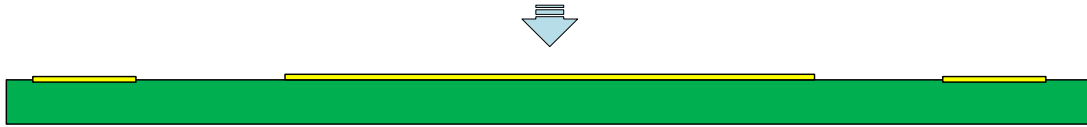
12. Apply compound glue



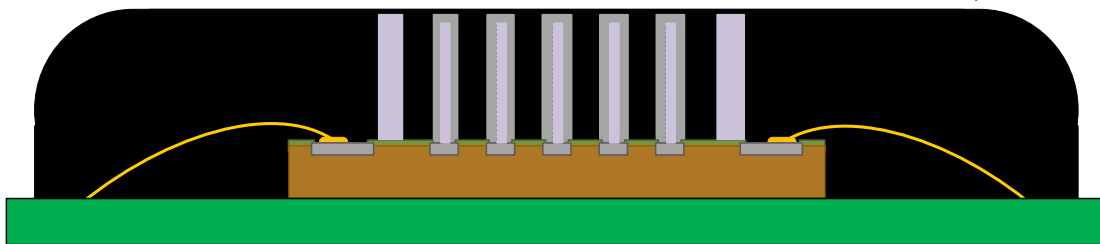
13. Remove the carrier wafer



14. Place the chip on the PCB



15. Apply the bondwires



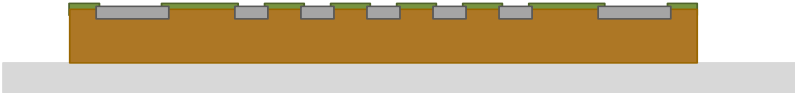
16. Encapsulate the bondwires

Appendix B.2 Visual representation for creation SU8 cavities

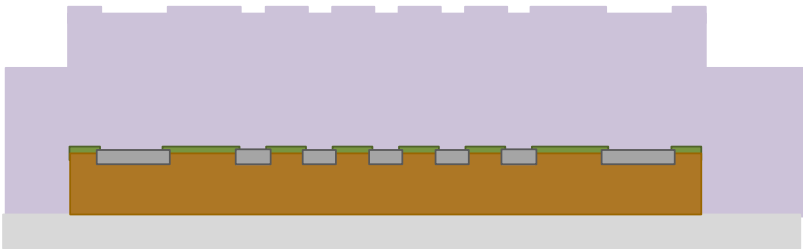
In this section the visual representation for creation of cavities in SU8 are given.



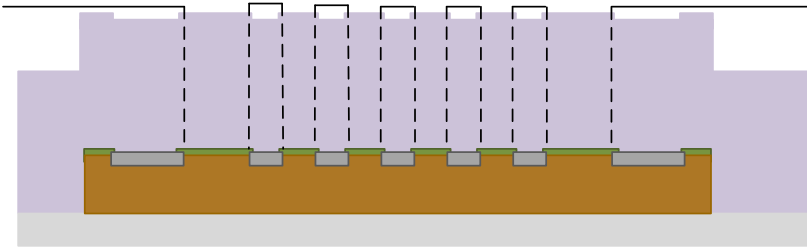
1. The chip



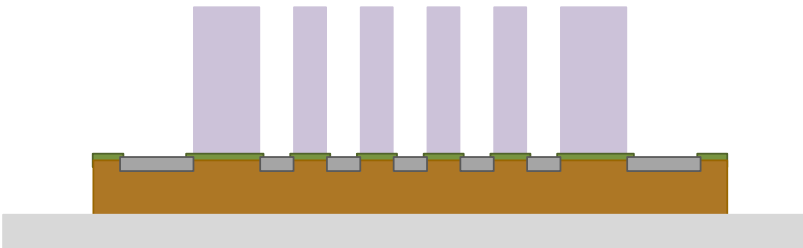
2. Glue the chip to a carrier wafer



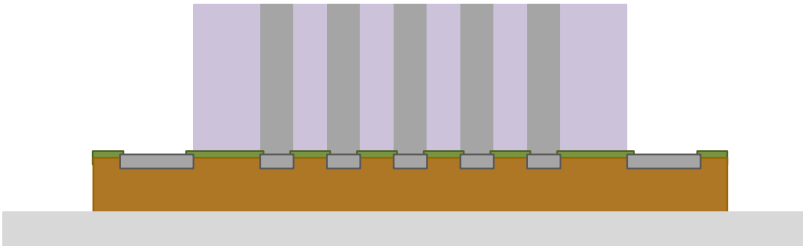
3. Coat with SU8



4. Expose in the EVG420 mask aligner



5. Develop in PGMEA



6. Fill the cavities with aluminium particles

Appendix B.3 [Flowchart](#)

One can find the flowchart designed to perform processing steps in the Cleanroom at the EEMCS faculty.

Esence packaging

FLOWCHART

VERSION 01

Valid from January 2020

Name of Owner:	Elke van der Lingen	Mask Set:	
Name of Mentor:	Daniel Yi/ Henk van Zeijl	Mask Box:	
Run Number:	EC2442	Die size:	2.5 by 2.3 mm
Wafer Amount:	8	Start Date:	1-1-2020
Subject to PCC:		PCC Approved:	

Materials: SU8 – 2075, AZ9260, PGMEA, Al-1% Si, AZN1of2000 Series
Labs: Polymer Lab, Cleanroom 100, Cleanroom 1000

DELFT UNIVERSITY OF TECHNOLOGY ELSE KOOI LABORATORY	
Adress	: Feldmannweg 17, 2628 CT Delft, The Netherlands
P.O. Box	: 5053, 2600 GB Delft, The Netherlands
Phone	: +31 - (0)15 - 2783868
Fax	: +31 - (0)15 - 2622163
Website	: www.tudelft.nl/ewi/onderzoek/faciliteiten/else-kooi-lab

GENERAL RULES

CLEANROOM BEHAVIOUR

- 1 Always follow the "Security and Behavior" rules when working in the EKL laboratories.
 - 2 Always handle wafers with care during processing. Use cleanroom gloves and work as clean as possible!
 - 3 Use cleanroom gloves when working with vacuum equipment. Do not touch the inside or carriers with bare hands.
 - 4 Always check equipment and process conditions before starting a process. Do NOT make unauthorized changes!
- Directly notify the responsible staff member(s) when there are problems with the equipment (like malfunction or contamination). Flip the status card on the machine over to **DOWN** to warn other users. Also change the status of the system to **DOWN** in the "[Phoenix Living Database](#)" system.
- 6 **DO NOT TRY TO REPAIR OR CLEAN EQUIPMENT YOURSELF**, and **NEVER** try to refresh a contaminated etch or cleaning bath! Only authorized staff members are allowed to do this.

WORKING WITH NON-STANDARD MATERIALS

- 1 All substrates, layers and chemicals which are not CMOS compatible are considered to be "**NON-STANDARD**" materials. These materials may cause contamination of bathes, equipment, wafer boxes, etc..
 - 2 The use of "non-standard" materials for processing in the class100 and SAL cleanroom must **ALWAYS BE EVALUATED** and **APPROVED** by your mentor and the EKL contamination officer. It is strictly forbidden to use these materials without permission.
 - 3 Wafers that are contaminated may **NEVER** be processed in any of the bathes or equipment without permission. Special precautions may be required, like the use of a separate container or special substrate holder or carrier.
- You must work according to the rules from the "[EKL Preventive Cross Contamination \(PCC\)](#) document, available on the [Sharepoint webpage](#)", and the **Materials** database from the "[Phoenix Living Database](#)" system.

CLASS 100 RULES

CLEANING OF WAFERS

After 4 hours of storage wafers must always be cleaned before performing a **COATING, FURNACE, EPITAXY** or **DEPOSITION** step. Use the correct cleaning procedure:

- Tepla stripper ⇒ for removal of implanted or plasma etched photoresists.
- Acetone ⇒ for removal of photoresist that is not implanted or plasma etched.
- HNO₃ 99% (Si) ⇒ for CMOS compatible wafers which do not need a HNO₃ 69.5% step.
- HNO₃ 99% (Al) ⇒ for wafers which are or have been in contact with "green" metals (e.g.: Al, Al(1%Si), Ti, Mo, Zr, ...).
- HNO₃ 99% (Si) + HNO₃ 69.5% (Si) ⇒ for all other CMOS compatible wafers.

Note: The above described cleaning procedures are only valid for CMOS compatible wafers with CMOS compatible materials on them. **For all other wafers follow the PCC rules and check the Phoenix Materials database.**

Wafers do **NOT** have to be cleaned **after** a furnace, epitaxy or deposition step if the next process step will be performed immediately, unless the wafers are covered with particles.

FURNACE RESTRICTIONS

Wafers that are covered with photoresist or a metal layer may **NEVER** be processed in any of the furnaces. This also applies for wafers from which a metal layer has been removed by etching. Only alloying in tube C4 is allowed for wafers with an aluminium layer.

MEASUREMENTS

Always perform all the measurement and inspection steps, and **write down the results in your journal and in the logbooks that can be found at some of the equipment**. The results are used to monitor the processes and/or equipment.

It is possible to measure directly on your (CMOS compatible) process wafers with the following Class 100 equipment:

- The Leitz MPV-SP, the WOOLLAM and the KEYENCE microscope. The first 2 systems are used for thickness measurements of transparent layers, and the third system is used for 3D surface metrology. The measurements are non-destructive and without contact to the wafer surface.
- The Dektak 8 surface profilometer. This system is used for step height measurements. In this case a needle will physically scan over the wafer surface, which can be destructive for structures. It is a contact measurement.
- The XL50 or Hitachi SEM. They can be used for inspection of your wafers and for width, depth or thickness measurements.

Note:

- After certain measurements **cleaning of your wafers** may be required for further processing.
- An extra wafer must be processed when other measurements are required (like sheet resistance and junction depth measurements). These wafers can not be used for further processing.

STARTING MATERIAL

Use **SINGLE SIDE** polished **LOW RESISTIVITY** (L_{RES}) wafers,
with the following specifications:

Type: p/B (p-type, boron)

Orientation: $\langle 100 \rangle$

Resistivity: 2-5 Ωcm

Thickness: $525 \pm 15 \mu\text{m}$

Diameter: 100 mm

NOTE: When storing the wafers after SU8 coating, store the wafers not downside but in horizontal wafer position (backside of wafer is horizontal and not vertical in the box) position.

GLUE THE CHIPS ON THE WAFER CARRIER

Use double sided kapton tape to glue the chips on the carrier wafer. Place the chips in such a way that you create a 3x3 array.

MANUAL SPINNER PREPERATION

Location: Class 100 Cleanroom

Equipment name: Brewer Science Manual Spinner 1 or 2

Coat the manual spinner with aluminium foil all around the spinning area.

Change the aluminium foil at the end of the process.

Use the rubber uncontaminated vacuum wafer holder.

Dispose the tissues and aluminium foil in a dustbin with an extraction on top in the class 100.

SU8 POURING AND FLOODING

Equipment name: Brewer Science Manual Spinner 1 or 2

Use 1 ml SU8.

Flood SU8 on the wafer to coat the structures on the surface of the wafers.

SU8 SPINNING 200 μm

Note: Spinning speed and time will be optimized for specified substrate and topology based on the results of the test runs.

Recipe: x_SU8_2075_200um_EBR

Step 1: 300 rpm in 60 second (acceleration rate 100 rpm/s), check if the SU8 covers complete surface.

Step 2: 1000 rpm in 60 seconds (acceleration rate 300 rpm/s)

Step 3: 10 rpm in 300 seconds (acceleration rate 300 rpm/s)

Remove the aluminium foil at the end of the process. Dispose the tissues and aluminium foil in a dustbin with an extraction on top in the class 100.

EDGE AND BACKSIDE CLEANING

Use the cotton swabs to clean the edges and the backside of the wafer use Acetone. If done correctly thee should be no SU8 on the backside.

Visual inspection.

Remove the wafer from the chuck and clean the chuck with Acetone and the spinning bin with IPA.

Clean the glass lid with IPA and the metal lid with Acetone.

Visual inspection

PRE-EXPOSURE SOFT BAKING

Perform baking on the brewer science hotplate 1 or 2 or the manual hotplate.

Use clean dummy wafer

A recommended soft bake time for 200um is 80 min at 95 °C.

(How to check: remove the wafer from hotplate, wait until it cool down, clamp the wafer with your tweezer, observe if the tweezer leaves marks on the SU-8 film, if yes, bake more).

ALIGNMENT AND EXPOSURE

Exposure will be performed on the EVG420 Contact Aligner.

Align the mask to the markers on the wafer.

Exposure time: 2 minutes use Hard Contact. If the wafer sticks to the mask then the soft bake time was too short.

Note 1: Clean the chuck after use with Acetone and IPA

Note 2: Use dark mask no structures at the edge of the wafer

Note 3: Store existing mask in dedicated mask container in personal cupboard. Take special precaution if cleaning is needed.

POST EXPOSURE BAKING

Perform baking on the hotplate next to the manual spinner

Use clean dummy wafer.

Step 1: 65°C -5 minutes
Step 2: 95 °C -15 minutes

Note: Allow slow cool down to room temperature

DEVELOPMENT

Location: Polymer Lab

Use PGMEA Developer at room temperature.

Time: 40 minutes (Do extra development if needed)

Rinse the wafers with IPA. If white residue is seen, develop longer.

Immerse the wafer in IPA for 10 minutes in a beaker.

Immerse the wafer in Water for 10 minutes in a beaker.

Note 1: Dispose chemicals in 'Halogeen arme- organische stoffen' III use bottle SAL

Note 2: Store SU8 and developer in the chemical room. Inform Robert about carrier nr.

DRYING OF THE WAFERS

Rest the wafer on a clean tissue under the fume hood on a hotplate set at 50 °C. The IPA will evaporate very soon.

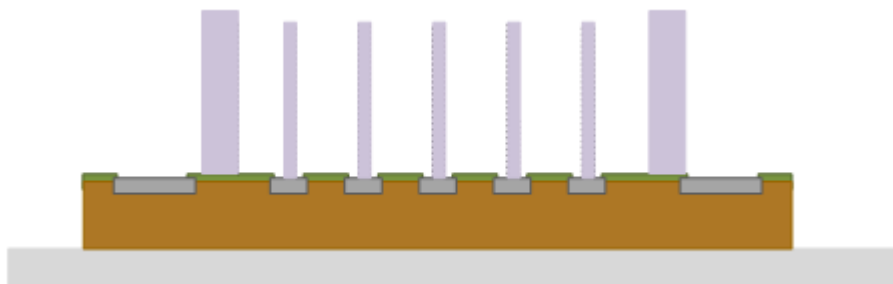
HARDBAKE

Location: Photoresist oven

For curing and degassing bake at 120 °C for 1 hour under vacuum in oven. Perform baking horizontal on a clean dummy wafer to prevent contamination.

MEASUREMENT AND INSPECTION

Perform SEM XL50 inspection to check the SU8 Height and surface. Result:



METALLIZATION

Note: LUT Test needed to perform deposition. Specification $LUR \leq 2 \times 10^{-6}$ Torr L/s. Use the Trikon Sigma 204 sputter coater for the deposition of an Al/Si layer on the wafers. Follow the operating instructions from the manual when using this machine.

Use recipe **AlSi_Organic_RT_25C**, if you open this recipe you will see two sub-steps,

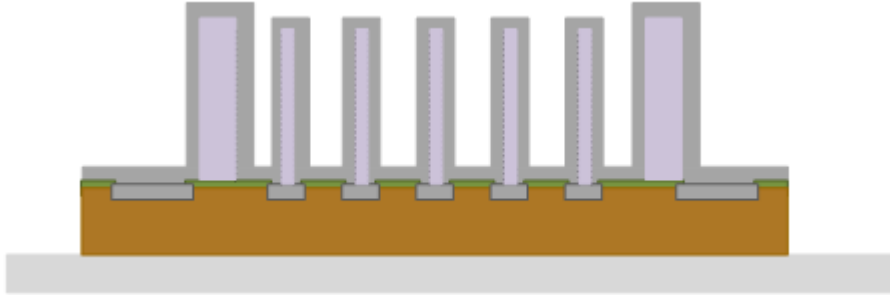
1) HSE_etch,

2) AlSi_Organic_1000nm.

The HSE etch is used to clean native oxide on the Al pads before deposition to have a good electrical contact.

To obtain 4 μm thick Al/Si(1%) layer, we need to repeat deposition steps.

Use recipe Al/Si for organics @ 25 °C with 4 times 4 deposition cycle of 250 nm and 3 cycles of cooling down to sputter a 4 μm layer.



SPRAY COATING AND BAKING

Processing will be performed on the EVG101 Spray coater. Perform an HMDS (hexa methyl disilazane) treatment with nitrogen carrier gas for 5 minutes. Follow the instructions specified for this equipment, **and always check the temperature of the hotplate first.**

Repeat 3 times:

- Use Coating Program 'HP_1000mbar_2m1_8layers' (resist thickness 6 μm) with AZ 9260.
- Perform a post baking step at 110 °C for 1 minute.

Last round 5 minutes post baking at 100 °C.

Wait for 30 minutes for rehydration, AZ9260 requires rehydration for exposure.

ALIGNMENT AND EXPOSURE

Exposure will be performed on the EVG420 Contact Aligner.

Check the dose of the EVG420 to correct the time is necessary. Dose was around 15 mJ/cm².

Align the mask to the markers on the wafer.

Exposure time: 20 Seconds use Hard Contact. If the wafer sticks to the mask then the soft bake time was too short.

Note 1: Clean the chuck after use with Acetone and IPA

Note 2: Use dark mask no structures at the edge of the wafer

Note 3: Store existing mask in dedicated mask container in personal cupboard. Take special precaution if cleaning is needed.

POST EXPOSURE BAKING

Perform a post-exposure bake at 115 °C for 1 minute.

Hotplate – Spray Coater.

DEVELOPMENT

Location: Polymer Lab

Use AZ400K:H₂O (1:2) (AZ developer) at room temperature.

Time: 30 seconds (Do extra development if needed)

Rinse the wafers with DI water. If white residue is seen, develop longer.

Dry the wafers with a gentle stream of air or nitrogen.

For (1:4) use 2 minutes

Note 1: Dispose chemicals in 'Halogeen arme- organische stoffen' III use bottle SAL

HARDBAKE

Location: Photoresist oven

For curing and degassing bake at 120 °C for 1 hour under vacuum in oven. Perform baking horizontal on a clean dummy wafer to prevent contamination.

WET ETCHING ALUMINIUM ETCH, RINSE DRY

Moisten	Rinse for 1 minute in wet bench A/B in the SA Lab 'H ₂ O/ Triton X-100 tbv Al. Ets'. The bath contains 1 ml Triton X-100 per 5000 ml Deionized water.
Etching	Use wet bench A/B in the SA Lab. 1 litre buffered aluminium etch fluid contains: 770 ml concentrated phosphorus acid (H ₃ PO ₄ 85 %), 19 ml concentrated nitric acid (HNO ₃ 65%) 140 ml concentrated acetic acid (CH ₃ COOH 100%) and 71 ml deionized water.
Etch time	26 minutes. 4000 aluminium would be removed (because 30 seconds is 75 nm)
QDR	Rinse in deionized water.
Drying	Rest the wafer on a clean tissue under the fume hood on a hotplate set at 50 °C.

PHOTORESIST LAYER STRIPPING

Dissolve the photoresist in acetone for 2 -3 minutes. Put the wafers in the Acetone carrier boxes and perform cleaning in Demi water and dry the wafer.

MEASUREMENT AND INSPECTION

Perform SEM XL50 inspection to check the SU8 Height and metallization height.

MEASUREMENT AND INSPECTION

Measure the device characteristics on the process wafers.

Appendix B.4 Process with spin coating SU8 at 1300 rpm and 800 rpm

B.4.1 Process with spin coating SU8 at 1300 rpm to create SU8 metalized pillars

SU8 metallization with 1300 rpm spin coating of SU8

Using the SEM_Philips_XL50, a tilt image can be created. The resulting images can be seen in Figure 77. Figure a) shows a single chip SU8 metallization. Here can clearly be seen that there is no height on the dike. Meaning that the SU8 for the dike has been removed. This can have several causes. The first probable cause is that during the deposition of the aluminium too much stress was introduced on the SU8 structures and thereby the SU8 dike got detached from the wafer. The second probable cause is that after development the baking time is chosen too short, also resulting in detachment of SU8. For clarification of the causes, there is chosen to compare two dikes to each other and see when the detachment occurred. The comparison can be seen in Figure 77c. Looking to the top part of the first dike shows that metallization is performed on the wafer. However, in the second bottom dike, no metallization can be found and the bare silicon wafer is visible. This means that during and after deposition the SU8 dikes have been removed. This evidence, results in the same two causes, to ensure that the next metallization steps on SU8 wafers do not result in the same detachment of the SU8. There is chosen to use an Al + 1% Si deposition with cooling down steps in between. Also a lower deposition energy is chosen. The results show the need for longer baking steps after development.

Figure 77b shows the dimension of the created SU8 pillars. These dimension show again that the created height is too small and that the diameter of the pillars is approximately $94 \pm 2 \mu\text{m}$, where it should be approximately $88 \mu\text{m}$. This concludes that the separation between the mask and wafer can be reduced or that a hard or soft contact should be chosen. Finally, represents Figure 77d a high-resolution picture of the metallization on a SU8 pillar. Here is shown that the metal particles are attached to the SU8.

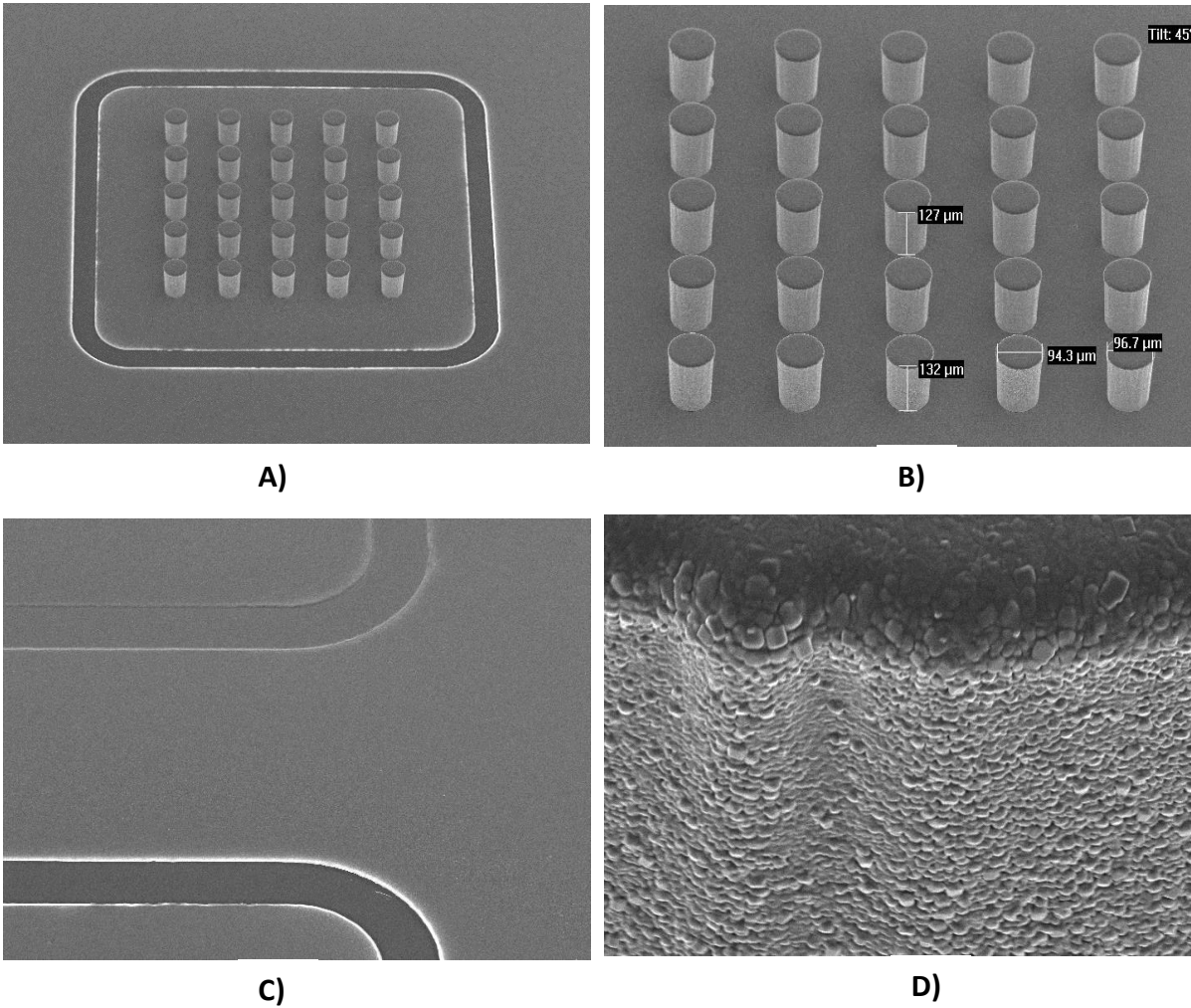


Figure 77: Tilt images from SU8 metalized pillars: a) Total overview of a single chip SU8 metallization, b) SU8 pillar metallization for the 5x5 array, c) Two dike images of two chips SU8 metallization, d) High resolution metallization on top view of SU8 pillar.

B.4.2 Process with spin coating SU8 at 800 rpm to create SU8 metalized pillars

The vertical measurements of the third attempt, where a spin speed of 800 rpm is used, can be seen in Figure 78. The first measurement, which is performed, is regarding the height of the dike according to a vertical plane distance. This height is defined in the figure by [1] and is given as 217 μm . The pillar height is given by [3] and is 218 μm .

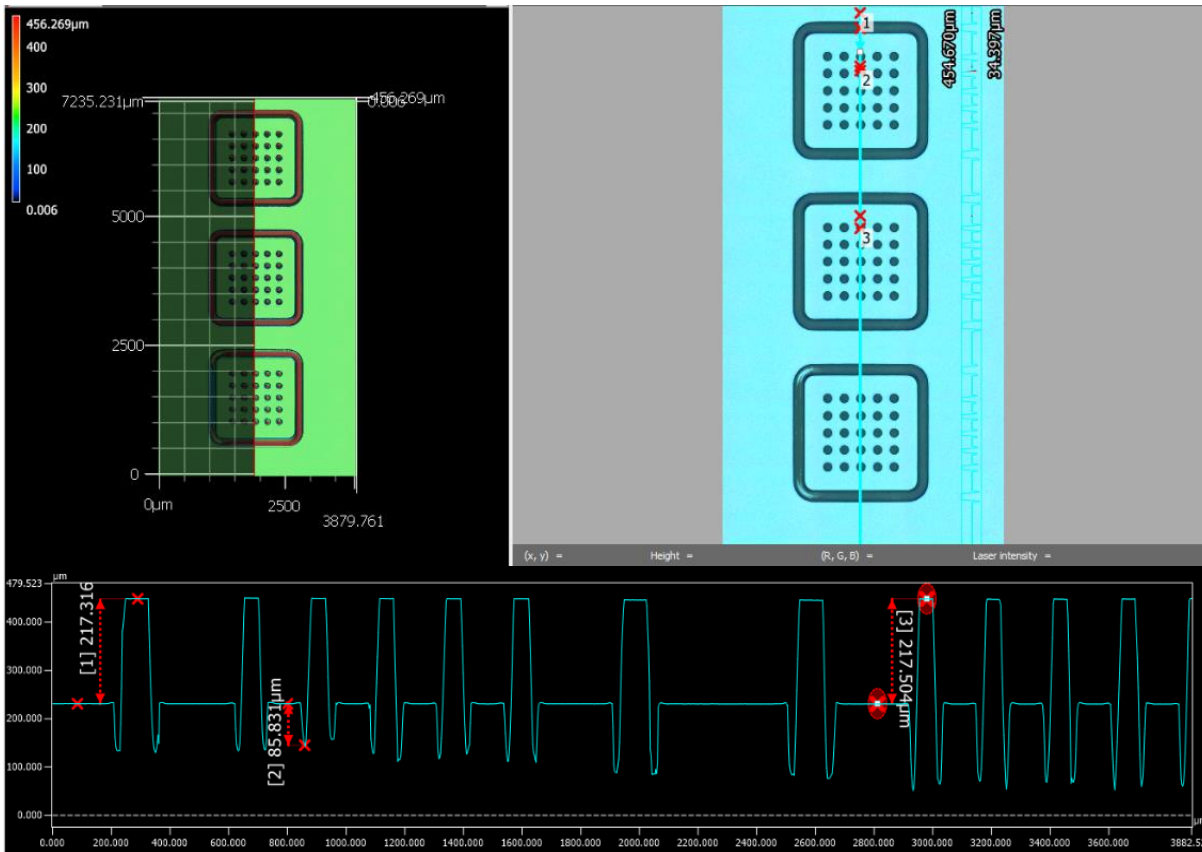


Figure 78: Vertical height measurements of spin coating SU8 with 800 rpm.

The height measurement according the horizontal plane measurements is given in Figure 79. Here the first measurement, annotated by [1] in Figure 79, is not a measurement as expected. There is not a pillar shown, but a valley. This is due to the fact that during the spin coating an air bubble was trapped inside the SU8. This air bubble was located at exactly this place and therefore introduced a valley in the measurements instead of a pillar. Nevertheless is the right side of the dike still present and the height measurement is given by [4], which is 223 μm . Furthermore, the height of the first pillar (annotated by [2]) is 223 μm . In addition to the height measurements with the Keyence, a height measurements is performed using the Dektak. For this profilometer measurement a height of 221 μm for the dike and 200 μm for the pillar is observed, resulting in valid height measurements for the Keyence optical and laser microscope.

Comparing both the horizontal and vertical plane height difference results in a slightly deviation of the SU8 thickness, this is again due to the viscosity of SU8. Once more, these deviations can be neglected and does not influence the further process. Secondly, both height measurements are given to be > 200 μm , which is required for the bondwire height.

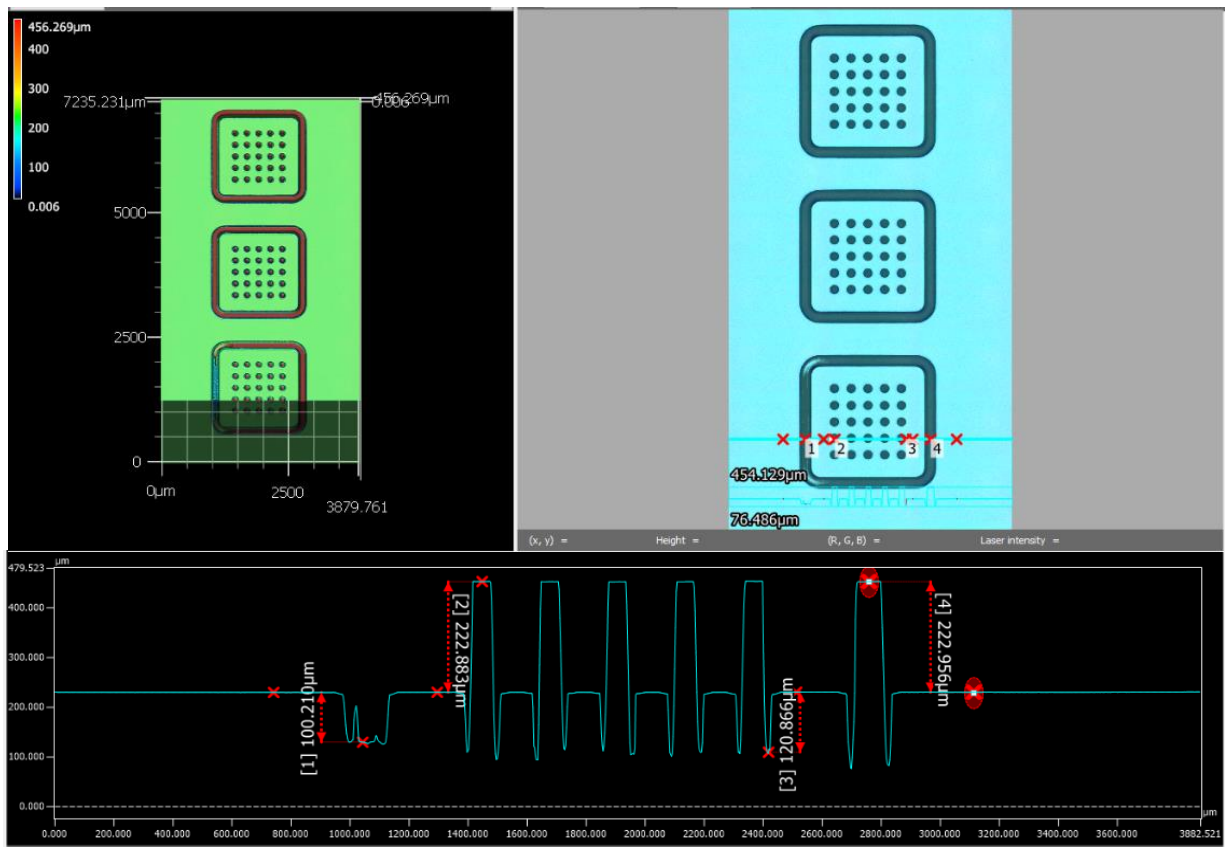


Figure 79: Horizontal height measurements of spin coating SU8 with 800 rpm.

The next step that should be performed is, deposit an aluminium with 1% silicon layer of 4 μ m on the SU8 pillars. The dummy wafers results according to the 1300 rpm speed, 1100 rpm and 800 rpm coating speed are discussed.

SU8 metallization with 800 rpm spin coating of SU8

Figure 80a shows the overall overview of a single chip metallization of the SU8 structures. From these results can be concluded that after deposition all the SU8 structures are still present. Figure 80b shows the dimensions of a single pillar. Again, the same mushroom type of shape is present similar to the SU8 pillar, where a spin speed of 1100 rpm was used. This results in the same conclusions as given for the 1100 rpm SU8 structures. Figure 80c represents a higher magnification of the deposited metal. Figure 80d shows a pillar representation at higher electron acceleration voltage, showing more features.

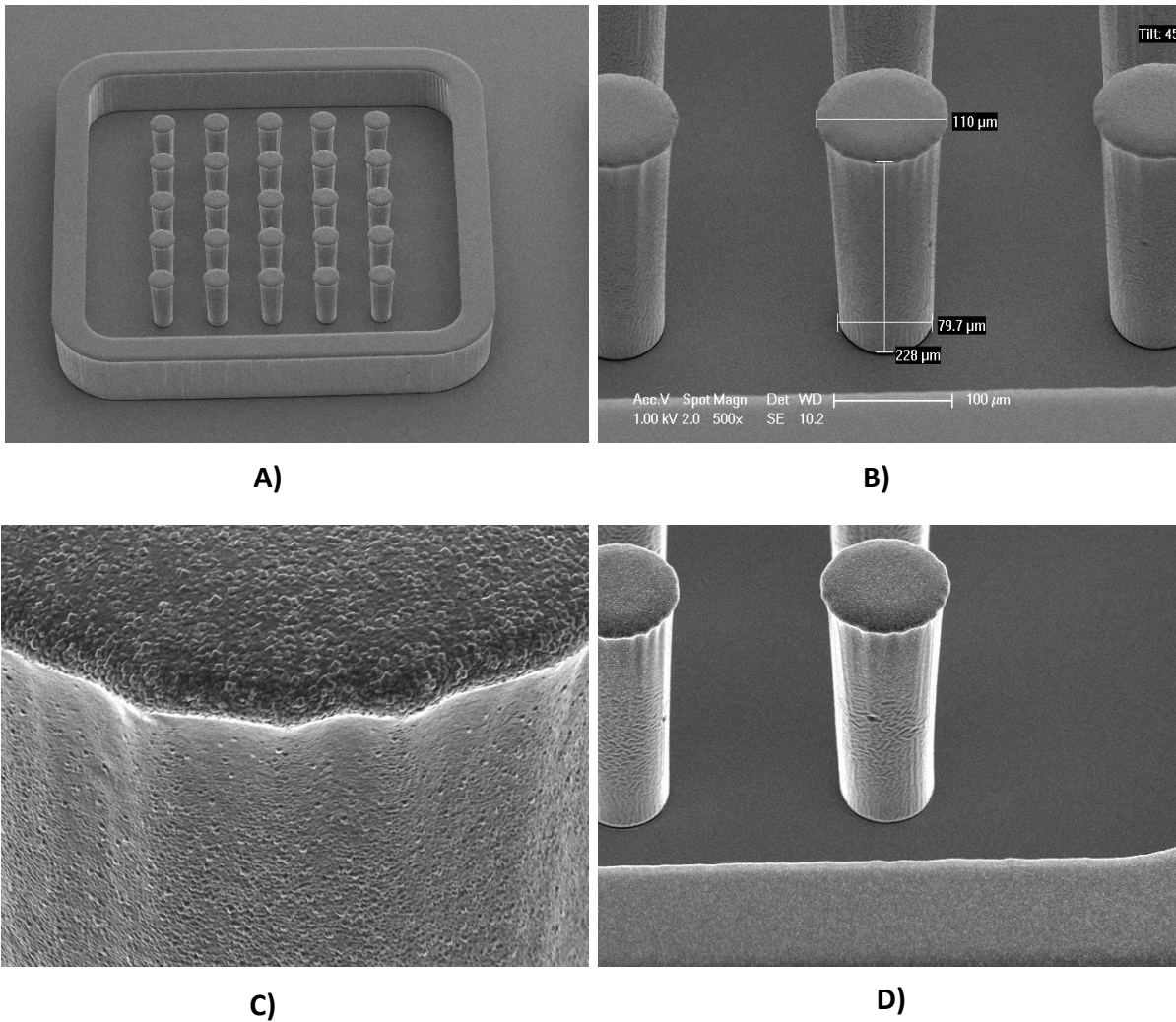
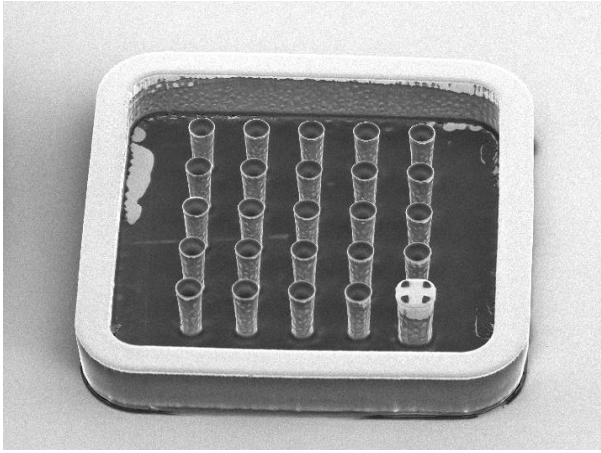


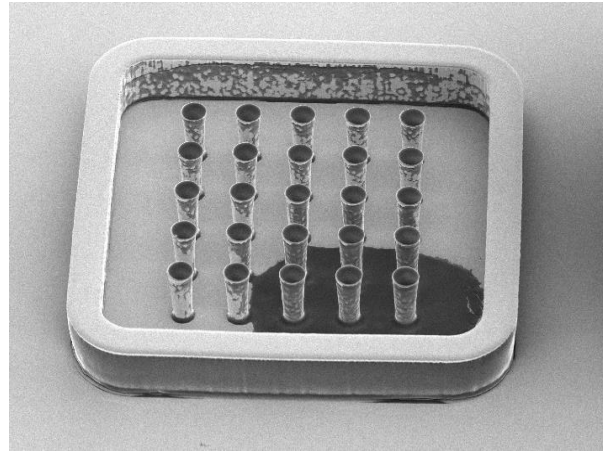
Figure 80: Tilt images from SU8 metallized pillars: a) Overall overview of a single chip SU8 metallization, b) SU8 pillar metallization for single pillar with dimensions, c) High resolution metallization on top view of SU8, d) Single pillar image.

Development of the AZ9260 on the 800 rpm spin coated SU8.

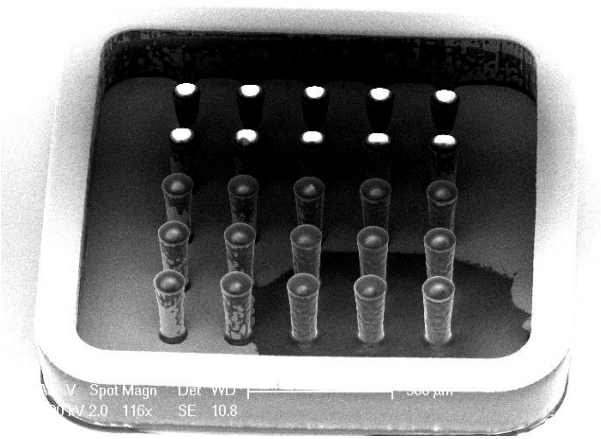
A representation of three chips with AZ9260 development is given in Figure 81 a, b and c. Here the same development occurred as for the 800 rpm spin coating. Note, that for each single chip development a different development pattern occurs, meanwhile the same development occurred at the wafer. Figure 81a clearly shows that the development was too short and that the photoresist is still in between the pillars. However, for Figure 81b and c development is also too short but only the bottom right part of the pillars are connected to each other. Furthermore, shows Figure 81d that the AZ9260 on the sides of the pillars is removed and will introduce pinholes when wet etching of aluminium is performed.



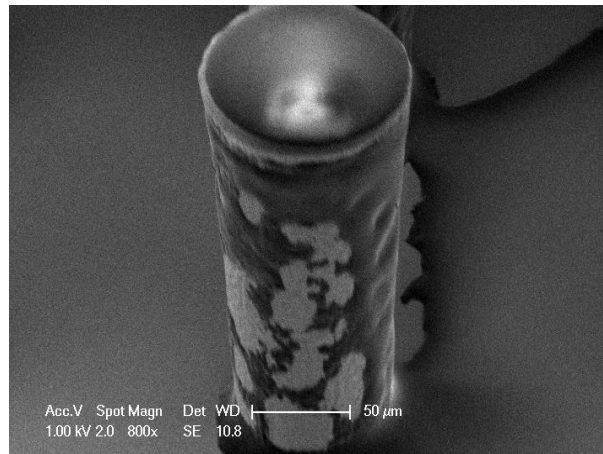
A)



B)



C)



D)

Figure 81: Tilt images from SU8 metalized pillars after AZ9260 development: a) Total overview of a single chip, b) Second chip total overview, c) Third chip total overview, d) High resolution development on pillar side.

B.4.3 Process with spin coating SU8 at 1000 rpm to create cavities in SU8

Creation of SU8 cavities for 1000 rpm spin coated SU8.

The results regarding the cavities, created in the 1000 rpm spin coated SU8 can be seen in Figure 82. Figure 82a represents a single chip overview of the cavities created in SU8. In this overview, the edges are not as sharp as the previous creation of the cavities. Moreover, do all the cavities have different diameters and the surface is not as smooth as expected. Figure 82b shows the dimension of a single cavity. Here, a better image is represented at a higher magnification. Nevertheless, is the cavity created till the silicon of the wafer. From these results, can be conclude that the baking step before development is performed too short and that the exposure energy was too high and/or that the development was too long.

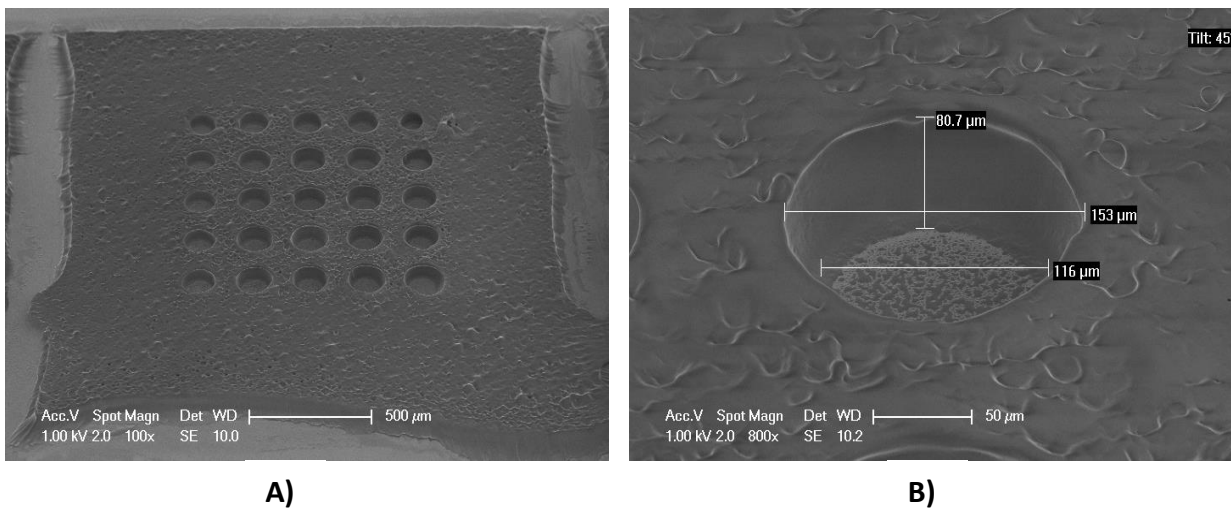


Figure 82: Tilt images for cavities in SU8 a) Overview of single chip b) Cavity dimensions.

Appendix C

Appendix C.1 Creation of calibration liquids

In the following section the code to generate the calibration liquids are given.

```
function CreateCalkitFilesForOneLiquid
close all;
clear all;
clc;

GHz = 1e9;
freq = linspace(1*GHz,3*GHz,3);    % Points in frequency from 1 GHz to 3 GHz in 3 points

[eta,eps,k,freq,lambda,omega,~,GHz,MHz,mm,um] = constants_LUT(freq);
Vs = 1;
[a,b,h,c] = dimensions(mm,um);
col = 'r';
[water,propanol,butanol,methanol,ethanol,air] = permittivity_colecole(freq);

%% For Water
epsr_med = water;
std_label = 'Water';
int_val = 15e3;

[freq,Y_total_new,Z_new,std_label,gamma] =
Admittance_MAIN_new(epsr_med,eta,eps,k,freq,lambda,omega,Vs,GHz,MHz,mm,um,a,b,h,c,std_label,int_val);
Water = struct('freq',freq,'eps',water.','y',Y_total_new,'z',Z_new,'gamma',gamma,'std_label',std_label);

name_file = [std_label, '.mat'];
save(['\Documents\' name_file])

% Plot the s-parameters on the smith chard
figure()
smithplot(Water.freq,Water.gamma.S11)
legend('Water');

%% For Propanol
epsr_med = propanol;
std_label = 'Propanol';
int_val = 2e3;
```

```

[freq,Y_total_new,Z_new,std_label,gamma] =
Admittance_MAIN_new(epsr_med,eta,eps,k,freq,lambda,omega,Vs,GHz,MHz,mm,um,a,b,h,c,std_label,int_val);

Propanol =
struct('freq',freq,'eps',propanol.','y',Y_total_new,'z',Z_new,'gamma',gamma,'std_label',std_label);

name_file = [std_label, '.mat'];
save(['\Documents\' name_file])

figure()
smithplot(Propanol.freq,Propanol.gamma.S11)
legend('Propanol');

%% For Butanol
epsr_med = butanol;
std_label = 'Butanol';
int_val = 2e3;

[freq,Y_total_new,Z_new,std_label,gamma] =
Admittance_MAIN_new(epsr_med,eta,eps,k,freq,lambda,omega,Vs,GHz,MHz,mm,um,a,b,h,c,std_label,int_val);

Butanol =
struct('freq',freq,'eps',butanol.','y',Y_total_new,'z',Z_new,'gamma',gamma,'std_label',std_label);

name_file = [std_label, '.mat'];
save(['\Documents\' name_file])

figure()
smithplot(Butanol.freq,Butanol.gamma.S11)
legend('Butanol');

%% For Methanol
epsr_med = methanol;
std_label = 'Methanol';
int_val = 2e3;

[freq,Y_total_new,Z_new,std_label,gamma] =
Admittance_MAIN_new(epsr_med,eta,eps,k,freq,lambda,omega,Vs,GHz,MHz,mm,um,a,b,h,c,std_label,int_val);

```

```

Methanol =
struct('freq',freq,'eps',methanol.','y',Y_total_new,'z',Z_new,'gamma',gamma,'std_label',std_label
);

name_file = [std_label, '.mat'];
save(['\Documents\' name_file])

figure()
smithplot(Methanol.freq,Methanol.gamma.S11)
legend('Methanol');

%% For Ethanol
epsr_med = ethanol;
std_label = 'Ethanol';
int_val = 2e3;

[freq,Y_total_new,Z_new,std_label,gamma] =
Admittance_MAIN_new(epsr_med,eta,eps,k,freq,lambda,omega,Vs,GHz,MHz,mm,um,a,b,h,c,std_label,int_v
al);

Ethanol =
struct('freq',freq,'eps',ethanol.','y',Y_total_new,'z',Z_new,'gamma',gamma,'std_label',std_label)
;

name_file = [std_label, '.mat'];
save(['\Documents\' name_file])

figure()
smithplot(Ethanol.freq,Ethanol.gamma.S11)
legend('Ethanol');

%% For Air
epsr_med = air;
std_label = 'Air';
int_val = 2e3;

[freq,Y_total_new,Z_new,std_label,gamma] =
Admittance_MAIN_new(epsr_med,eta,eps,k,freq,lambda,omega,Vs,GHz,MHz,mm,um,a,b,h,c,std_label,int_v
al);

Air =
struct('freq',freq,'eps',air.','y',Y_total_new,'z',Z_new,'gamma',gamma,'std_label',std_label);

name_file = [std_label, '.mat'];
save(['\Documents\' name_file])

```

```
figure()
smithplot(Air.freq,Air.gamma.S11)
legend('Air');

%% When you want to plot all the liquids together in 1 Smithchart
figure()
smithplot(Water.freq,Water.gamma.S11)
hold on;
smithplot(Propanol.freq,Propanol.gamma.S11)
smithplot(Butanol.freq,Butanol.gamma.S11)
smithplot(Methanol.freq,Methanol.gamma.S11)
smithplot(Ethanol.freq,Ethanol.gamma.S11)
smithplot(Air.freq,Air.gamma.S11)
hold off;
legend('Water','Propanol','Butanol','Methanol','Ethanol','Air');
end
```

Appendix C.2 Creation of the Look Up Table

In this section the Matlab code to generate the look up table is given.

```
%%%%%%%%%%%%%%%%%%%%%%%%%%%%%%%%%%%%%%%%%%%%%%%%%%%%%%%%%%%%%%%%%%%%%%%%
%%%%%%%%%%%%%%%%%%%%%%%%%%%%%%%%%%%%%%%%%%%%%%%%%%%%%%%%%%%%%%%%%%%%%%%%
%%%%%%%%%%%%%%%%%%%%%%%%%%%%%%%%%%%%%%%%%%%%%%%%%%%%%%%%%%%%%%%%%%%%%%%%          9 LUT PROF trying with 1 medium
%%%%%%%%%%%%%%%%%%%%%%%%%%%%%%%%%%%%%%%%%%%%%%%%%%%%%%%%%%%%%%%%%%%%%%%%          100 points
%%%%%%%%%%%%%%%%%%%%%%%%%%%%%%%%%%%%%%%%%%%%%%%%%%%%%%%%%%%%%%%%%%%%%%%%          Epsilon Complex (negative imag part)
%%%%%%%%%%%%%%%%%%%%%%%%%%%%%%%%%%%%%%%%%%%%%%%%%%%%%%%%%%%%%%%%%%%%%%%%
% 15 points for TauR due to new limits found.
% look at TauR_for_2 (up)
close all;
clear all;
clc;

tic;
GHz = 1e9;
freq_points = 3;                % step size for the frequency
f = linspace(1*GHz,3*GHz,freq_points); % Points in frequency from 1 GHz to 3 GHz
thickness = 1000;
num_lay = 1;                    % 1 medium
size = 100;                    % defines the matrix dimensions for the LUT

% FOR THE COAXIAL CABLE
% inner_radius = 0.523; %[mm]
% outer_radius = 1.5; %[mm]

% TEST FOR DIFFERENT SIZES MATRIX
% y_x1 = [(1:0.1:40) (41:1:80)];
% y_y1 = (0:0.1:40);           % generation of imag epsilon (start:step:stop)

% For standard generation of 100x100 LUT
y_x1 = linspace(1,81,size);
y_y1 = linspace(0,50,size);

% CONSTANTS FOR THE PIN AND PATCH
[eta,eps,k,freq,lambda,omega,Vs,GHz,MHz,mm,um] = constants_LUT(f);

% FOR THE PIN AND PATCH THE DIMENSIONS
[a,b,h,c] = dimensions(mm,um);

col = 'r';
N_port = 0;
N_pin = 1;
N_attach = 0;
Total_N = N_port+N_pin+N_attach;
delta_pin = h;
delta_pin_port = 0;
```

```

delta_pin_attach = 0;

br = 1;                %% br = 1, backing reflector is present
epsr = 3.55-1i*0.0096;    % PCB

start_time = tic;
Y_total = zeros(size,size,freq_points);
cnt1 = 0;
cnt2 = 0;
tempo2 = zeros(size,1,'uint64');
tempo1 = zeros(size,1,'uint64');
cycle1time_sec = zeros(size,1,'uint64');
cycle2time_sec = zeros(size,1,'uint64');

for p = 1:freq_points
    cnt1 = cnt1 + 1
    cnt2 = 0;
    for w = 1:length(y_x1)
        tempo2(w,1) = tic;
        cnt2 = cnt2 + 1
        cnt3 = 0;
        for q = 1:length(y_y1)
            cnt3 = cnt3 + 1
            tempo1(q,1) = tic;
            % We create the Epsilon:
            epsilon_cycle(w,q,p) = y_x1(w)-1i*y_y1(q);
            % This Look Up Table is made with less cycles.
            % The value taken are write up in the code. Easy to implement.
            % Now we need a way to take the correct value in the fastest way.

            % epsilon = squeeze(epsilon_cycle(w,q,:));
            % FOR THE COAXIAL CABLE
            % y_mango_9(w,q,:) =
Admittance_coax(epsilon9,num_lay,inner_radius,outer_radius,thickness,f);

            % FOR THE PIN AND PATCH
            % Y_total(w,q,:) = Admittance_pin_patch_LUT(epsilon,a,b,h,c,eta,eps,k,omega,Vs);
            int_val = 1e3;
            int_val_adm = 1e3;
            int_val_adm2 = 1e3;
            [Zmom,Vmom] =
Impedance_matrix(k(p),a,b,c,h,Vs,omega(p),eta,eps,N_port,N_pin,N_attach>Total_N,delta_pin_port,de
lta_pin,...
delta_pin_attach,int_val,int_val_adm,int_val_adm2,br,epsr,epsilon_cycle(w,q,p));
            Admittance = inv(Zmom);
            C_num = cond(Zmom);
            Voltage = Vmom.';

```

```

        Imom = Admittance*Voltage;
        N_basis = 1;
        [z_pos_prime] =
z_pos_prime_export(h,N_basis,N_port,N_pin,N_attach,delta_pin,delta_pin_port,delta_pin_attach);

        Apin = -
1.*Imom.*Vmom_z_function(k(p),a,b,h,Vs,omega(p),eta,N_basis,N_port,N_pin,N_attach,eps,delta_pin_p
ort,delta_pin,delta_pin_attach,...
z_pos_prime,int_val_adm2,br,epsr,epsilon_cycle(w,q,p));

        Apatch = -
Imom.*Vmom_rho_function(k(p),eta,a,b,c,h,Vs,br,epsr,epsilon_cycle(w,q,p),int_val_adm);
        Admi = Apin+Apatch;
        Y_pinpatch(w,q,p) = Admi;
        Y_sc(w,q,p) = Yext_sc_function_str(k(p),a,b,eta,Vs,epsr,epsilon_cycle(w,q,p),h);
        Y_total(w,q,p) = Y_pinpatch(w,q,p)+Y_sc(w,q,p);

    end
end

%     if ~exist Admittance_LUT_clp5mm,'dir'
%         mkdir(Admittance_LUT_clp5mm);
%
        if mod(p,1)==0
            Y_LUT(:, :, p) = Y_total(:, :, p);
            epsilon_LUT(:, :, p) = epsilon_cycle(:, :, p);

            name_file = 'Admittance_LUT_freq3p_1p0_3p0_100p_TEST.mat';
            save(['LUT\' name_file], 'Y_LUT', 'epsilon_LUT', 'f');
            clear Y_total;
            clear epsilon_cycle;
            clear Y_pinpatch;
            clear Y_sc;
        end
end
timing_cicle_sec = toc(start_time); % x s
timing_cicle_min = timing_cicle_sec/60; % x min
timing_cicle_sec = toc(start_time) % x s
timing_cicle_min = timing_cicle_sec/60 % x min

```

Appendix C.3 Building blocks influences

C.3.1 Interconnect influences

For these measurements the following setup is considered.

- Frequency range is from 0.5 GHz till 2.5 GHz with 5 steps.
- Calibration liquids used are water, methanol and air.
- IF bandwidth is 30 Hz
- Output power is -10 dBm
- Measurement is performed on methanol cable distortion.
- Integration interval is 1000

With the cable measurements the following cable distortions were applied to the cable. The 'cable influence 1' is where the cable has not experienced any movement or bending, so the measurement occurs in the ideal case. 'Cable influence 2' is when hitting on the cable was applied during a measurement. For 'cable influence 3' the cable has been waggged.

The S11-parameter measurement of the cable distortion can be found in Figure 83. From this figure can be seen that the ideal case is slightly off with the different cable influence measurements. Also the ideal measurement result is not the same as the measurement where no cable distortion occurs. This could be because of the calibration with one of the three liquids was not that accurate as should be for the measurement. This can be due to the fact that or the liquids where impure or the pin and patch has not been cleaned properly, resulting in a mixture of different liquids. One thing that can be seen from the S11-parameter measurement is that the cable distortion with different types of malfunctioning the cable does not have an influence on the measurements. This means that distortion of the cable does not influence the S11-parameter measurements.

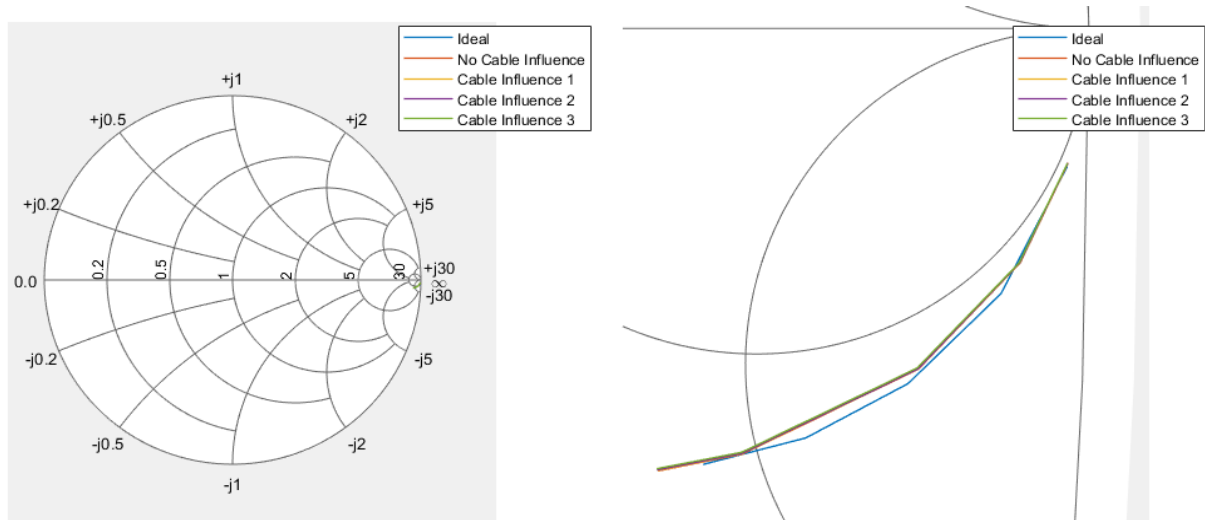


Figure 83: a) S11-parameter of the cable influence measurements b) Zoom version of the S11-parameter

When conversion of the S11-parameters to admittance occurs and using the LUT to find the according epsilon, the following figures can be found (see Figure 84). Here is also shown the difference with the ideal ethanol permittivity Cole-Cole model and with the measurements with and without cable distortion. This is due to the fact explained in the S11-parameter measurement. However, when looking at the measurements only without the ideal case and looking at the real epsilon permittivity measurement, can be observed that there is no difference between cable distortion and no cable distortion. This does not apply for the imaginary part of the permittivity. Here a small change between the cable distortion and without cable distortion can be observed. However, this difference does not have an impact on the measurement, because mostly the real permittivity part will be concerned when examining hydration in the human skin.

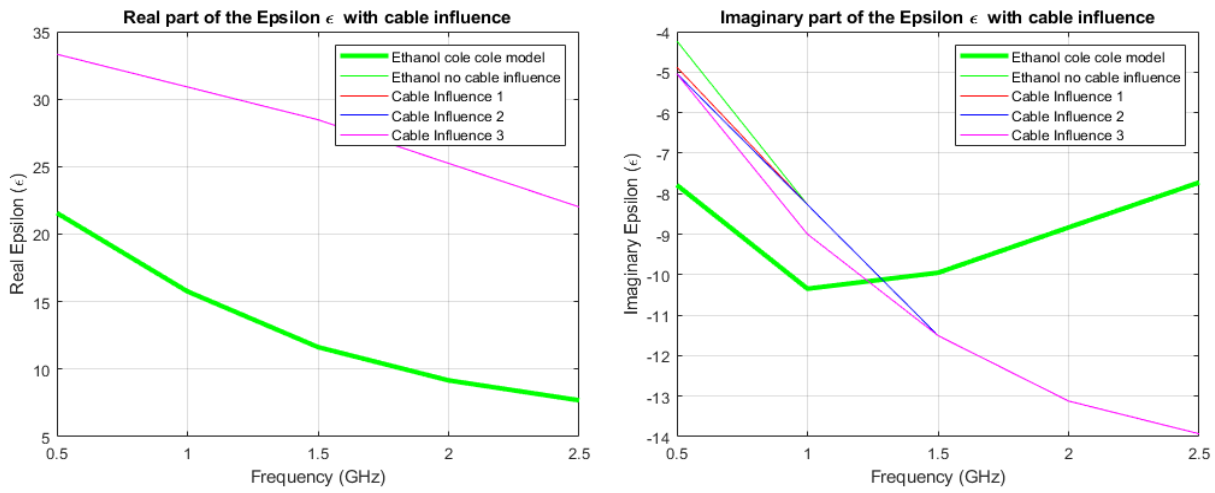


Figure 84: a) Real epsilon measurement of the cable distortion b) Imaginary epsilon for cable distortion measurement.

C.3.2 MUT interface

Another parameter that could influence the permittivity measurements is the immersion depth of the pin and patch for liquid measurements. For instance, just touching the water surface instead of being completely immersed in the liquid level with the pin and patch can give an error in the measurement results. Because of air between the patch and the Material Under Testing occurs in a measurement an error due to different permittivity can be detected specifically for liquid and air.

The following setup and variables are used for the depth measurements;

- Frequency range is from 0.5 GHz till 2.5 GHz with 5 steps.
- Calibration liquids used are water, methanol and air.
- IF bandwidth is 30 Hz.
- Output power is -10 dBm.
- Measurement is performed with deionized water.
- Integration interval is 1000

For the depth measurement there is chosen to perform the measurements with deionized water. Because of the higher viscosity of water than the other calibration liquids. This results that the water will stick on the pin and patch, which makes it possible to remove the pin and patch from the water surface resulting in a bubble that will still be attached on the pin and patch surface.

The water level measurements can be seen in Figure 85. Here there are three different water depth measurements. The first measurement is when the pin and patch are put deep in the water. The second measurement is when the pin and patch is lifted above the water level, which results in a bubble connecting between the pin and patch and the water surface. The third measurement is where only one side of the pin and patch is touching the water surface. When a normal measurement is performed, the pin and patch will be put in the water resulting in a water layer in the bottom and top side of the water. When this occurs the pin and patch will stay at this place and a measurement will take place.

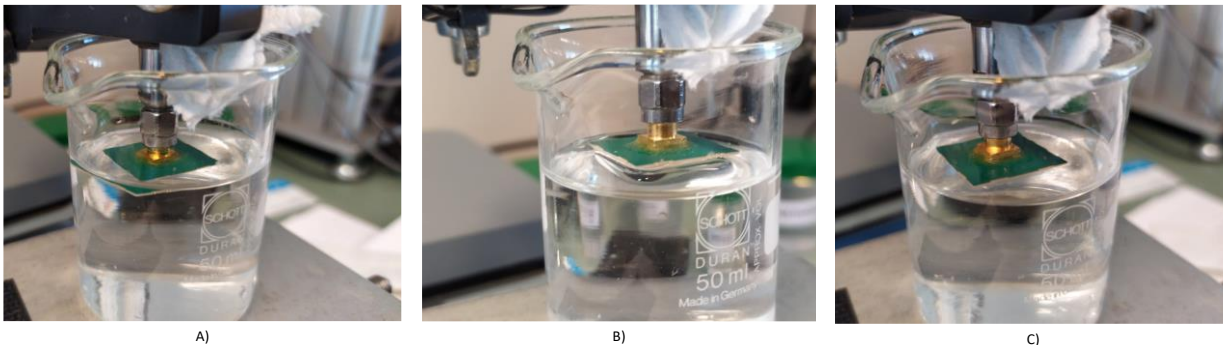


Figure 85: Water depth measurements; a) Deep inside the water b) Above the water surface creating a bubble c) Gold measurement, where the water is just touching the pin and patch.

With the different measurement depths, the following results were obtained for the S_{11} -parameter (see Figure 86). These results show different S_{11} values for each type of water depth measurements. However, none of the measurements is exactly the same as the desired Cole-Cole model. When only looking at the measurement results for the different depths can be seen that each measurement is different. Also, can be observed that the deep water measurements are the most accurate measurements compared to the Cole- Cole model. So, from the S_{11} -parameter, it can be concluded that the deep water level measurement is the most accurate measurement.

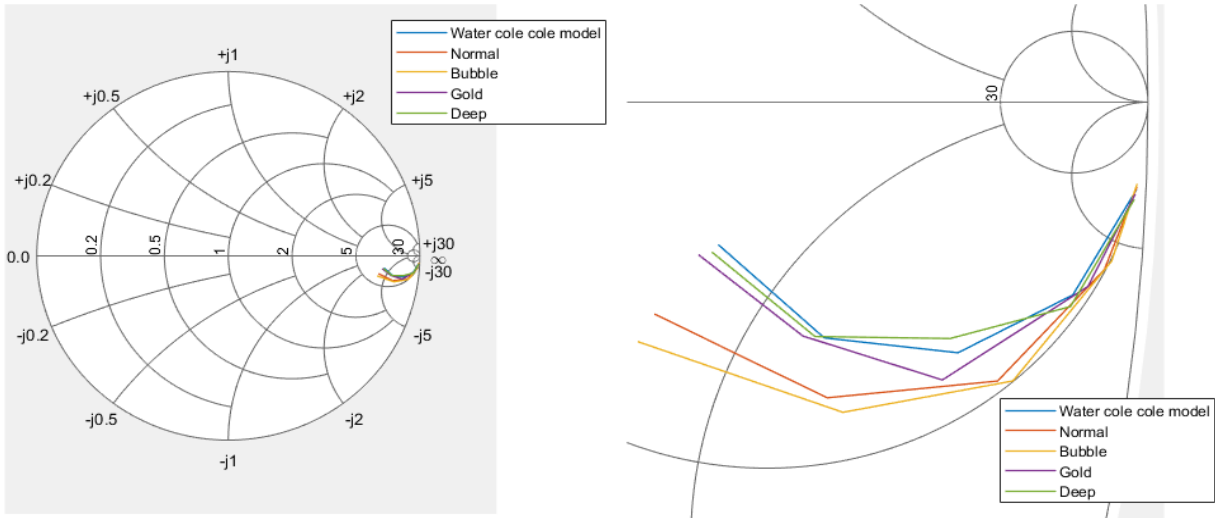


Figure 86: S11-parameter measurement with different liquid depths.

The real and imaginary epsilon obtained from the depth measurements can be seen in Figure 87. From the real part of the epsilon for the permittivity measurements, it can be seen that the water depth measurements from 1.5 GHz discard from the desired Cole-Cole model result. Nevertheless, each measurement goes wrong in the same way. The differences between these measurements is that they do not have a large difference. However, when looking at the imaginary part of the epsilon for the different depth measurements, it can be seen that there is a large difference between the depth measurements. So, from the imaginary measurements of the permittivity, can be concluded that the depth of the liquid measurements results in different permittivity values. However, due to the diminished accuracy for the imaginary epsilon permittivity, the real epsilon is considered as being the most accurate value when performing permittivity measurements.

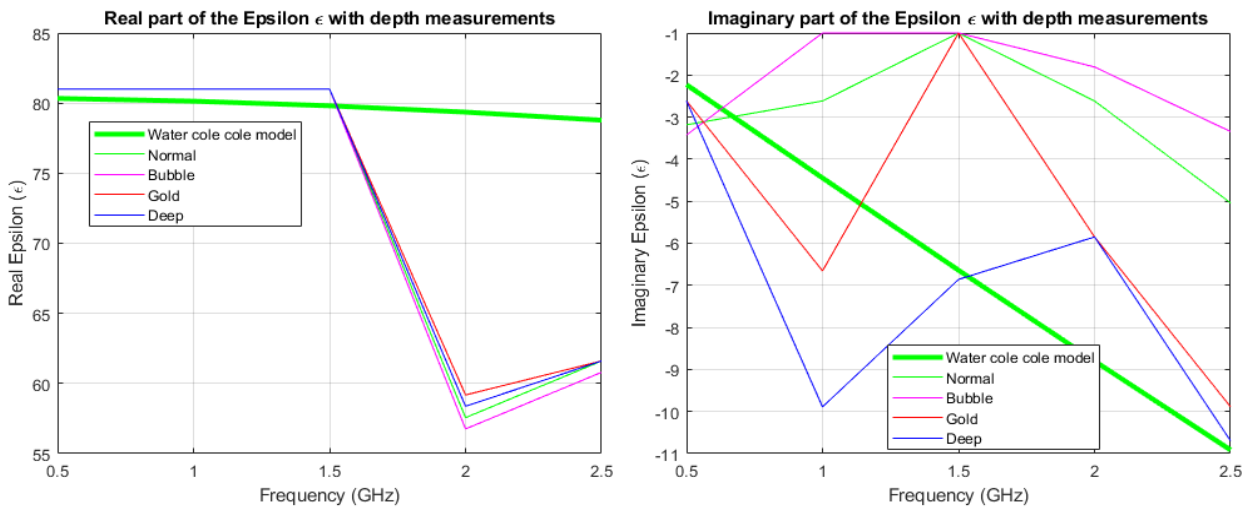


Figure 87: Permittivity measurements with real and imaginary epsilon for water depth measurements.

C.3.3 Calibration measurements

Another liquid measurement can be performed for which different ranges of epsilon calibration are used. Here two types of calibration measurements can be distinguished. In the first calibration measurement the 3 known liquids methanol, propanol and air are used for performing the measurements. The second calibration defines a calibration with water, methanol and air.

For both the calibration measurements the following variables hold;

- Frequency range is from 0.5 GHz till 5 GHz with 10 steps.
- IF bandwidth is 30 Hz.
- Output power is -10 dBm.
- Measurement is performed with deionized water.
- Integration interval is 1000 for generation LUT.
- Integration interval is 1000 for generation calibration liquids.

In theory, when applying different calibration liquids, it is possible to receive more accurate permittivity measurements for the liquids with lower real an imaginary epsilon. However, the measurements where a liquid is applied with a higher permittivity than the calibration liquids will give an inaccurate result back.

The resulting S11-parameter for calibration configuration 1 can be seen in Figure 88. From this configuration, it can be seen that the water measurement runs out of the Smith chart that results in a wrong permittivity measurement. This result is in line with the theory which was stated before.

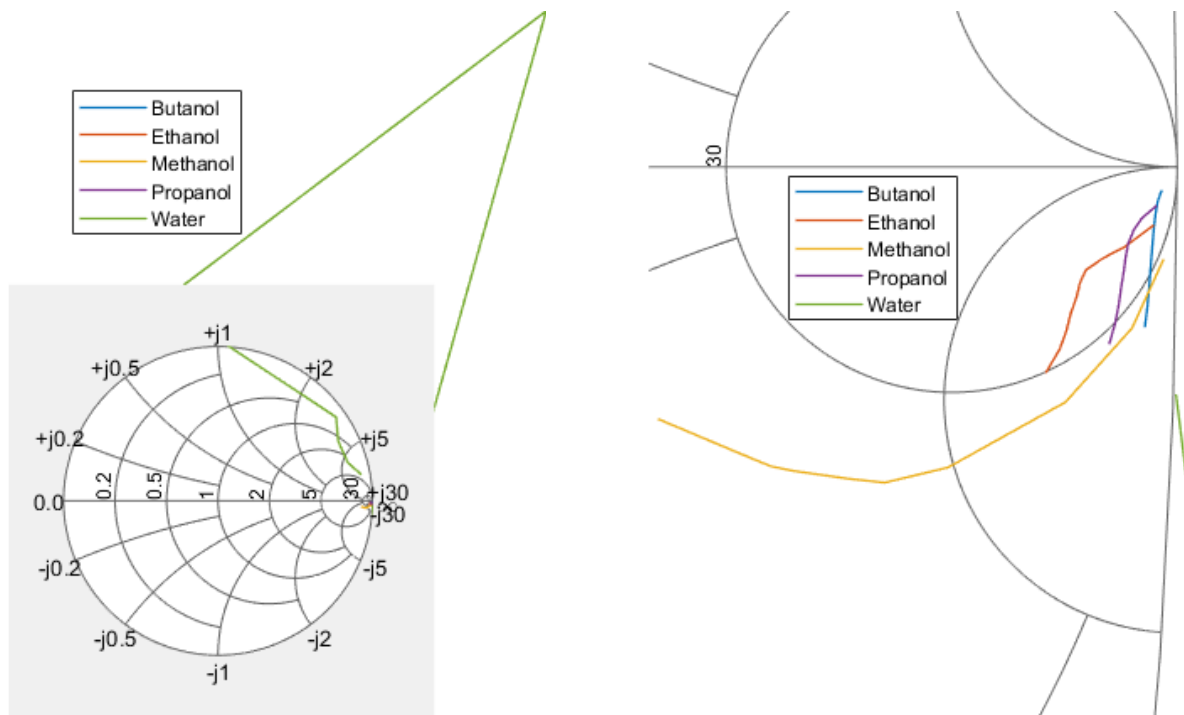


Figure 88: S11-parameter measurements for calibration configuration 1; a) general overview b) zoom version.

From the S11-parameter measurement, the permittivity can be obtained and this result can be seen in Figure 89. This result clearly shows that there are still some problems regarding the liquids.

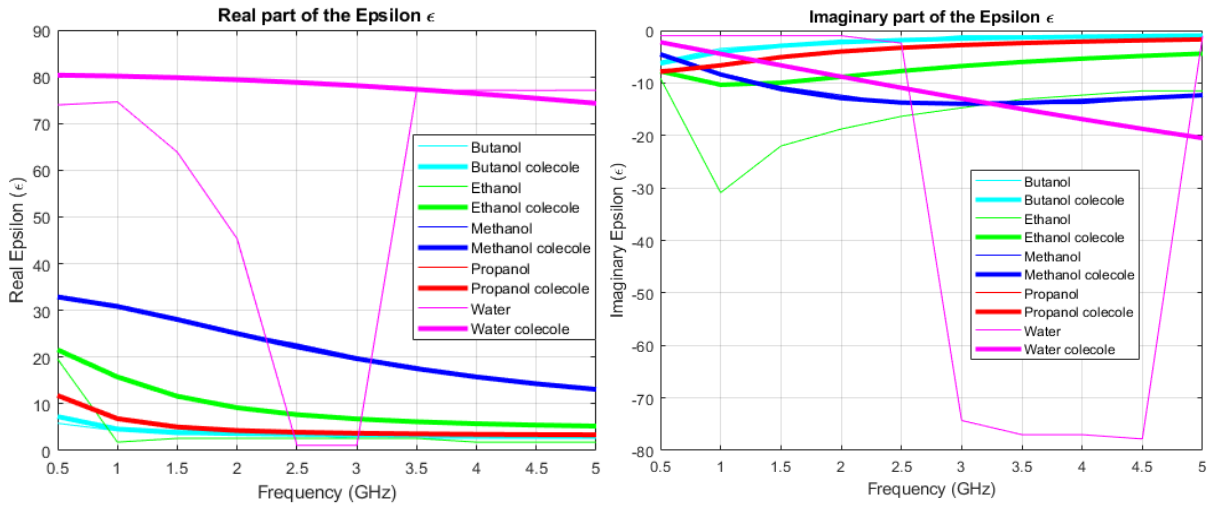


Figure 89: a) Real permittivity b) imaginary permittivity for calibration 1 configuration.

Calibration configuration 2:

The resulting S11-parameter results for the calibration configuration 2 can be seen in Figure 90. From these measurements can be seen that jumps in the liquids butanol, ethanol and propanol occur. These jumps can lead to inaccurate complex permittivities at these frequencies.

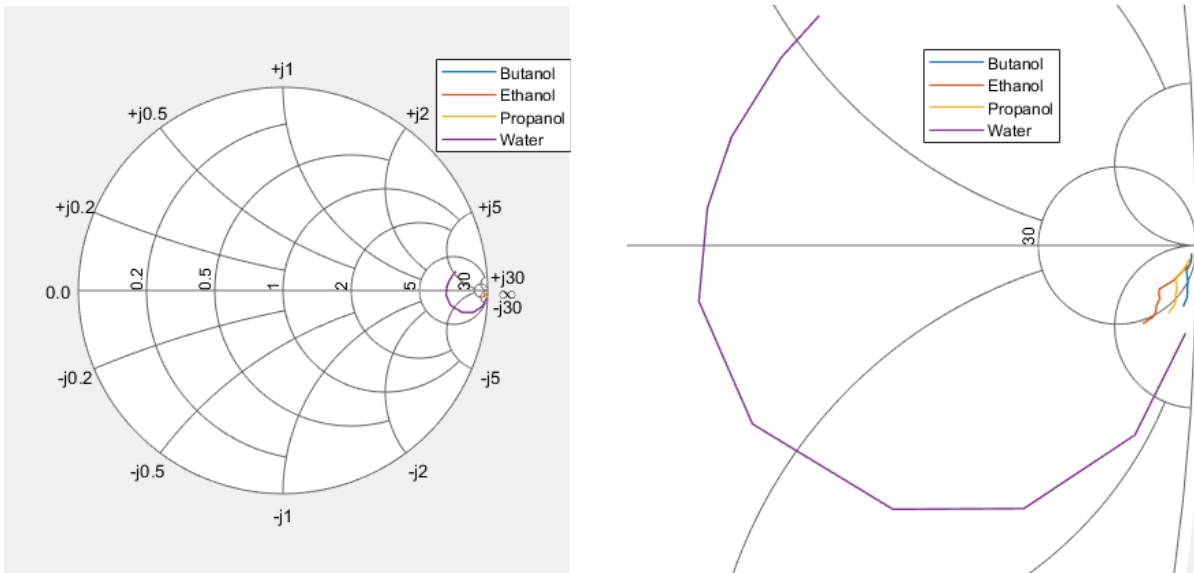


Figure 90: S11-parameter measurements for calibration configuration 2 a) general overview b) zoom version.

Converting the measured S11-parameter to complex permittivity, results in Figure 91. Even when a calibration with water is performed the measurement of water is not exactly on top of the Cole-Cole model. This conclusion can lead to two possibilities; namely, the liquids used are impure or the measurement configuration is not performed correctly.

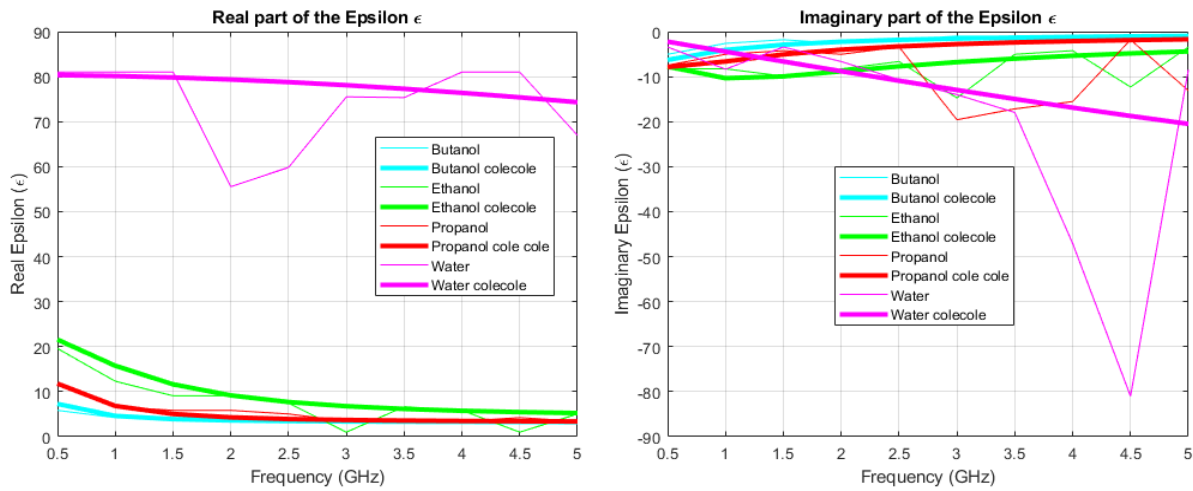


Figure 91: a) Real permittivity b) imaginary permittivity for calibration 2 configuration.

Comparing both measurements for both calibration configurations, results in inaccurate measurements. Here can be observed that the measurement of the calibrated liquid is not on top of the Cole Cole model, meaning that for both calibration configurations the results can be considered to be not accurate. Nevertheless, when using calibration liquids with a higher permittivity, the system is able to measure more accurate for liquids around that same permittivity of the calibration liquids.

C.3.4 S11-parameter for skin measurements

The resulting S11-parameter for the skin measurement for each test person is indicated in Figure 92. Looking at these results, one can conclude that the five series measurements for each person are closely related to each other, meaning that each measurement can be considered to be valid. Comparing the average value of each test person with respect to the other test person's measurements, also results in a slightly difference between the S11-parameter.

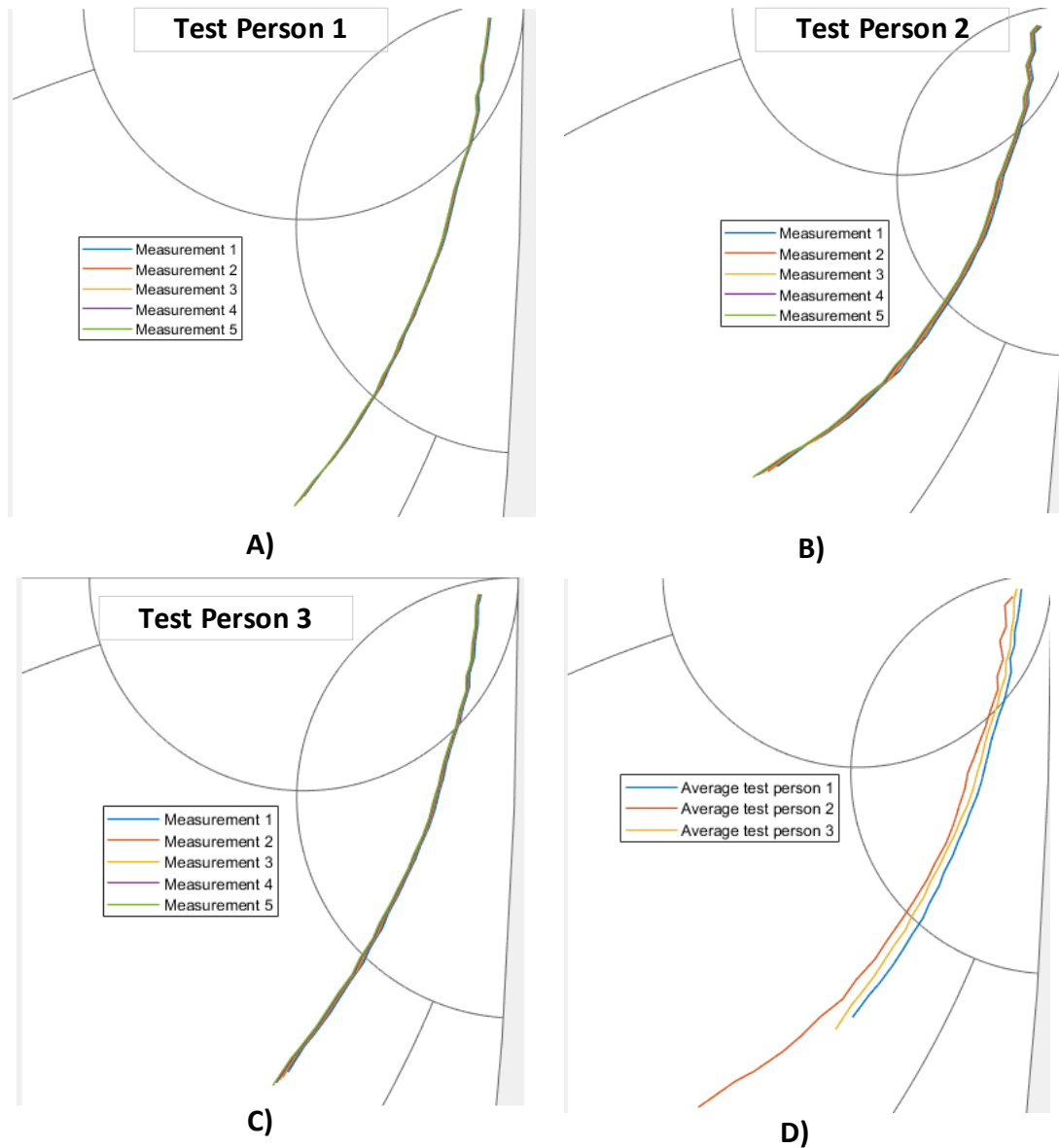


Figure 92: S11-parameter zero-state skin measurements: a) test person 1, b) test person 2, c) test person 3, d) average of each test person compared to each other.

Secondly, the measurements after 10 minutes of hydration in water can be examined. The measured S11-parameters can be seen in Figure 93. Here, the difference between the five serial individual measurements are slightly deviated from each other, but this difference is considered to be small and therefore can be neglected. Furthermore, is the difference between the test person's measurements clearly visible, which gives evidence that each skin cannot be considered as the same.

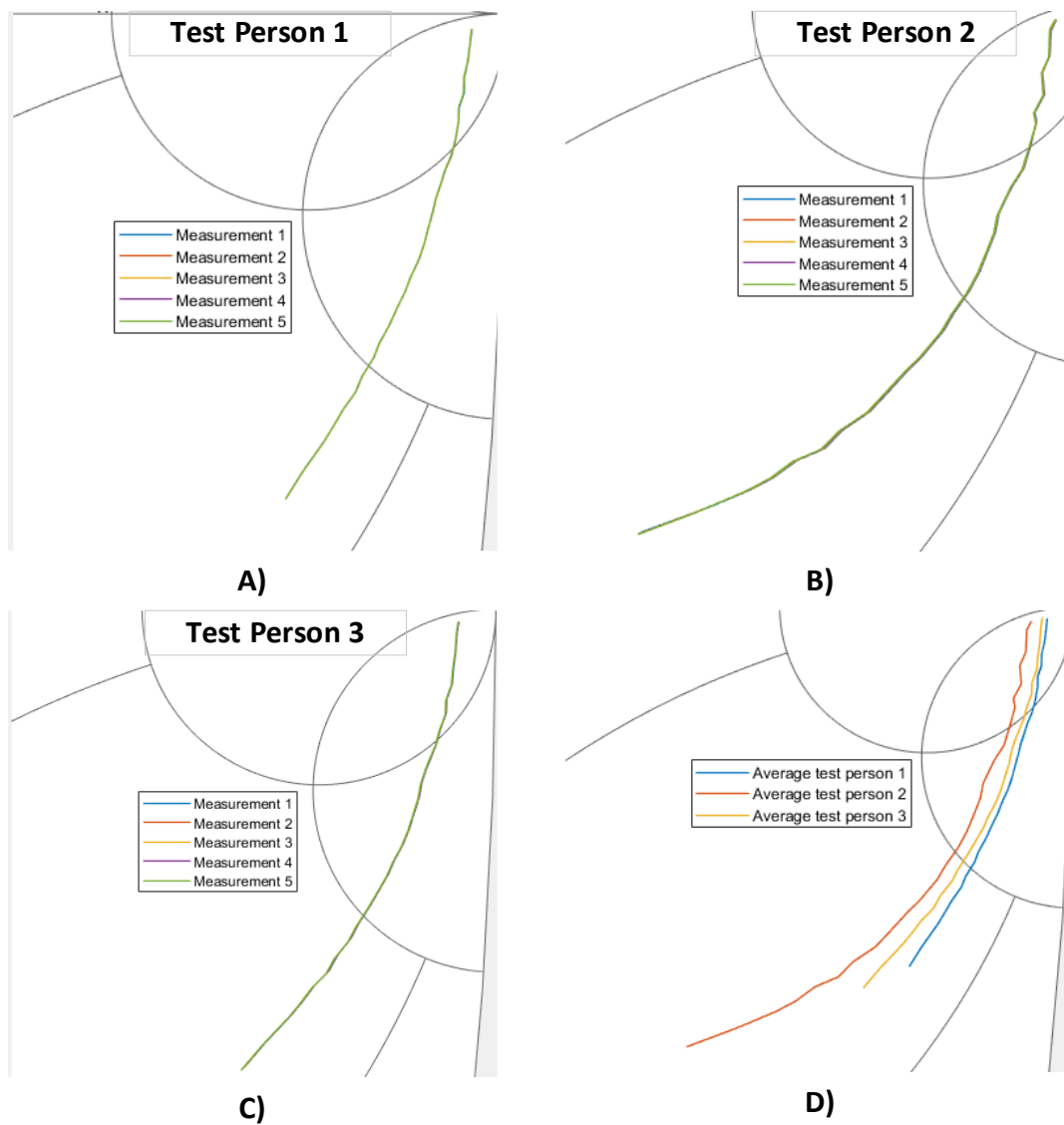


Figure 93: S11-parameter hydrated-state skin measurements; a) test person 1 b) test person 2 c) test person 3 d) average of each test person compared to each other.

From previous measurements in the zero-state and hydrated-state of the skin measurements a difference cannot be clearly detected. The S11-parameter for each test person is discussed and can be seen in Figure 94. From these results, can be concluded that a small difference is present between the hydrated- and zero-state for each test person. Also can be seen that the amplitude of the S11-parameter is larger than the zero-state.

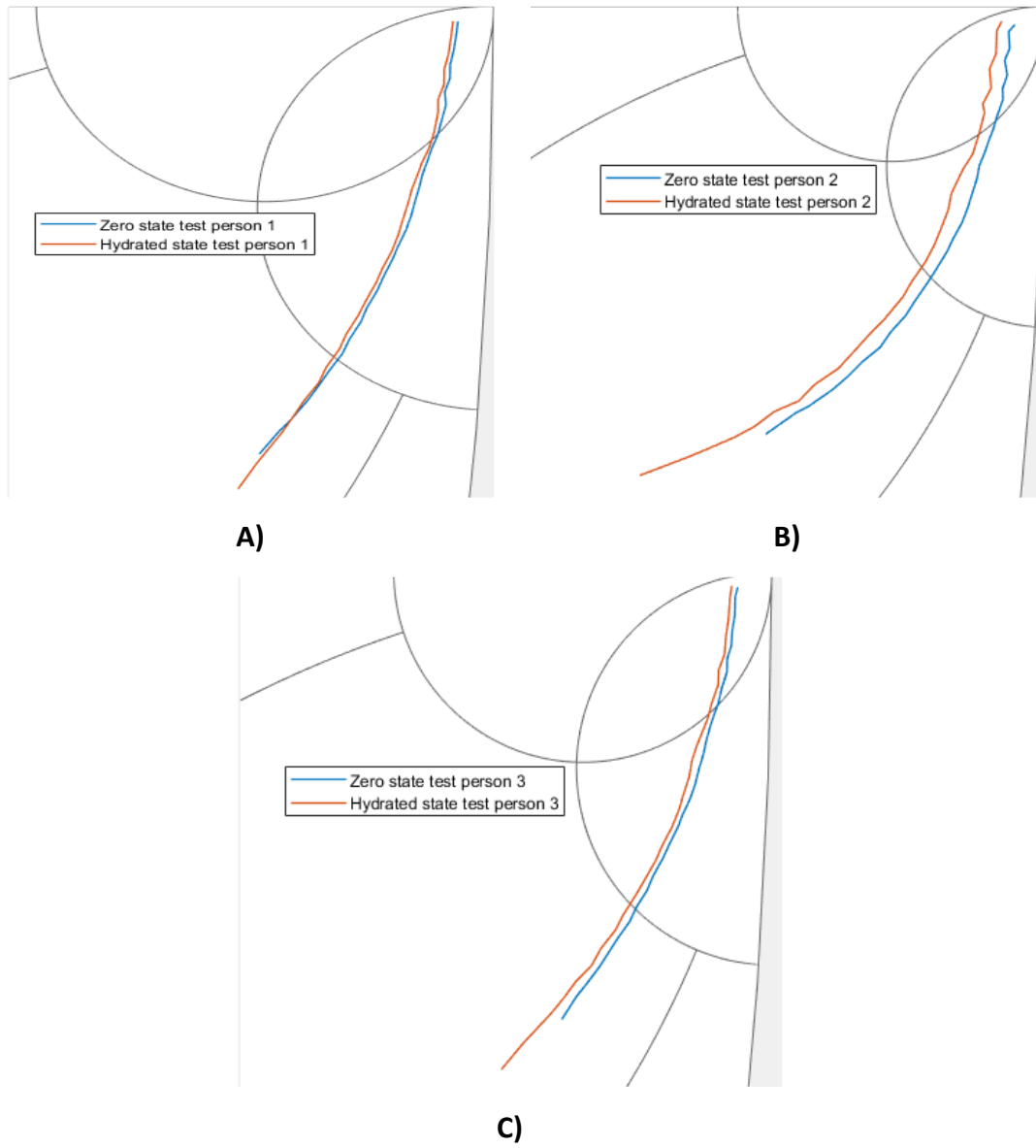


Figure 94: S11-parameter zero-state versus hydrated-state measurements; a) test person 1 b) test person 2 c) test person 3.